



City Research Online

City, University of London Institutional Repository

Citation: Aalinezhad, N. (2022). Mechanics of CSF in Human Ventricular System: Production and Circulation. (Unpublished Doctoral thesis, City, University of London)

This is the accepted version of the paper.

This version of the publication may differ from the final published version.

Permanent repository link: <https://openaccess.city.ac.uk/id/eprint/30635/>

Link to published version:

Copyright: City Research Online aims to make research outputs of City, University of London available to a wider audience. Copyright and Moral Rights remain with the author(s) and/or copyright holders. URLs from City Research Online may be freely distributed and linked to.

Reuse: Copies of full items can be used for personal research or study, educational, or not-for-profit purposes without prior permission or charge. Provided that the authors, title and full bibliographic details are credited, a hyperlink and/or URL is given for the original metadata page and the content is not changed in any way.

City Research Online:

<http://openaccess.city.ac.uk/>

publications@city.ac.uk

**Mechanics of CSF in Human Ventricular System:
Production and Circulation**



Narges Aalinezhad

Department of Mechanical Engineering and Aeronautics

City, University of London

Submitted in Partial Fulfilment for Degree of Doctor of Philosophy

December 2022

To Farzaneh & Amir Hossein

Abstract

Cerebrospinal fluid (CSF) is a water-like substance that circulates in a network of interconnected cavities located in the brain. The fluid ensures the brain's well-being by providing hydromechanical and biochemical support. Moreover, the fluid facilitates neurogenesis (i.e. the birth of neurones); a process essential for embryo development and self-repair in developed brains.

Changes in the composition or flow of CSF are linked to the development and progression of various neurological conditions such as hydrocephalus, multiple sclerosis, and Alzheimer's disease. These conditions have been recognised for over a century; yet there is no definite explanation for their onset nor there is a cure to restore brain health. Hence, medical interventions (e.g. surgery, medication) are used to control the abnormalities and prevent further damage, but they do not address the underlying cause. One reason for the lack of effective treatments is the limited understanding of the CSF system; its production, circulation, and absorption, in healthy and diseased states, and after treatments.

In this research, we aim to better understand the CSF system by conducting mathematical and computational modelling. At first, a comprehensive review of the existing literature is provided to bring to attention the controversies and misconceptions related to the system. Further, we discuss the necessity of exploring the system step by step to correct the existing conjectures.

We present a novel and comprehensive mathematical model of the organ responsible for CSF production (i.e. choroid plexus (CP)). This model integrates the CP's biological characteristics into physics and mathematical statements, which are solved using numerical techniques. The simulation predicts parameters such as pressure, concentration, and displacement of the CP, as well as the CSF production rate under different conditions such as ageing. This approach represents the first holistic method for understanding the dynamics of CSF production within the choroid plexus.

This research is extended to a preliminary investigation of CSF circulation in a 3D computational model of the brain cavities, constructed from magnetic resonance images (MRI). Simulation results characterise the CSF flow by providing information on pressure gradients, wall shear stresses, and fluid velocities.

Acknowledgement

I would like to thank my supervisor Dr. Mohammad Omidyeganeh for providing me with the opportunity to conduct this research and for believing in me throughout the journey. Progressing in this work would have not been possible without his vision, experience and support.

I would also like to thank my family for their constant support, encouragement, and unconditional love. Without their support, this accomplishment would not have been possible. Their unwavering faith in me and their willingness to stand by me during difficult times has been a source of inspiration.

Finally, I would like to extend my appreciation to my dear friends Sara Mennani, Florina Minzat, Kristine Hayhow, Olga Limantseva, Giorgio Cavallazzi, Soheil Ahmadi, Thibaud Plantegenet, Nastaran Namvar, Bahareh Eilbeigi, Mina Sowdagar and Salma Bahraman for their steady support, encouragement, and motivation that kept me focused and motivated during the most challenging times.

Contents

List of Tables	VI
List of Figures	IX
1 Introduction	1
1.1 Aims and outline of the thesis	3
2 Literature Review	5
2.1 Gross anatomy of CSF domain	5
2.2 Physiology of CSF	7
2.2.1 CSF production	8
2.2.2 CSF circulation	12
2.2.3 CSF absorption	16
2.3 Pathophysiology of CSF	20
2.3.1 Interruption in CSF production	20
2.3.2 Interruption in CSF circulation	21
2.3.3 Interruption in CSF absorption	21
2.4 Motivation and objectives	23
2.4.1 CSF production at choroid plexus	26
2.4.2 CSF circulation	28
3 Development of a Comprehensive Mathematical Model for the Choroid Plexus	32
3.1 Microanatomy of choroid plexus	32
3.2 Capillary vessel	36
3.2.1 Mathematical modelling of capillary	37
3.2.2 Mathematical modelling of endothelial cells	40
3.3 Connective tissue	45
3.3.1 Mathematical modelling of connective tissues	46
3.4 Epithelial cells	53
3.4.1 Mathematical modelling of epithelial cells	58

3.4.2	Mathematical modelling of membranes & tight junctions	59
4	A Novel Microscopic Model for Choroid Plexus and CSF Production	62
4.1	Introduction	62
4.2	Methodology	62
4.2.1	Computational domain	63
4.2.2	Formulation	64
4.2.3	Governing equations	73
4.2.4	Conditions and constants	77
4.3	Validation, Verification, and Results	87
4.3.1	Concentration of solutes	88
4.3.2	Solute flux	89
4.3.3	Pressure distribution in compartments	91
4.3.4	Water seepage	92
4.3.5	Origin of CSF pulsation at CP	94
4.4	Chapter summary & future work	96
5	Role of Choroid Plexus in Ageing Brain and Development of Neurological Disorders	98
5.1	Introduction	98
5.2	Methodology	100
5.2.1	Ageing of choroid plexus	100
5.3	Results and discussion	101
5.3.1	CSF production	102
5.3.2	Capillary morphology	111
5.3.3	Choroid plexus volume	116
5.4	Chapter summary & future work	120
6	CSF Circulation in the Ventricular System	123
6.1	Introduction	123
6.2	Methodology	125
6.2.1	MR imaging & geometry reconstruction	125

6.2.2	Mesh generation	125
6.2.3	CFD methodology	126
6.3	Results and discussion	128
6.3.1	CSF flow characteristics	128
6.3.2	Velocity field	130
6.3.3	Stress distribution	131
6.4	Chapter summary & future work	133
7	Contribution, Conclusion & Future Direction	135
	Appendices	138
	Appendix A: Is the steady flow assumption valid?	138
	Appendix B: Table of variables	141
	References	142

List of abbreviations

AQ	Aqueduct
APM	Apical membrane
AQP1	Aquaporin
BBB	Blood-Brain-Barrier
BCSFB	Blood-CSF-Barrier
BLM	Basal membrane
BT	Brain tissue
Cap	Capillary
CNS	Central nervous system
CP	Choroid plexus
CPE	Choroid plexus epithelium
CSAS	Cervical sub-arachnoidspace
CSF	Cerebrospinal Fluid
EC	Endothelial cells
FOM	Foramen of Monro
ISF	Interstitial fluid
ICP	Intracranial pressure
LVs	Lateral ventricles
SAS	Subarachnoid space
St	Stroma
St_{in}	Stroma from endothelial side
St_{out}	Stroma from basal membrane and tight junction side
SpSAS	Spinal subarachnoid space
SVZ	Sub-ventricular zone
TJ	Tight junction
3V	Third ventricle
4V	Fourth ventricle

List of Tables

1	Summarised investigations from CFD simulations. LV:Lateral ventricles, FOM: foramen of Monro, 3V: third ventricle, 4V:fourth ventricle, AQ: aqueduct, CSAS:cerebral subarachnoid space, SpSAS: spinal subarachnoid space, BT: brain tissue.	30
2	Passage of substances via transcellular routes is facilitated by protein molecules such as channels, co-transporters, and pumps. Compounds- Na:sodium, Cl: chlorine, K:potassium, HCO:bicarbonate, H:hydrogen, AQP: aquaporin	55
3	Main constituent in blood accounted in this study and their concentrations. The unit is $nmol/mm^3$	79
4	Resting radius and thickness of membranes (R_o, θ_o), ABV. EC:endothelial cells, BLM: Basolateral membrane, APM: apical membrane, Vent: ventricles.	80
5	Calculated reflection coefficient of each solutes across EC: endothelial cells and TJ:tight junctions.	82
6	Hydraulic conductivity of each membrane, ABV. EC:endothelial cells, BLM: Basolateral membrane, APM: apical membrane, Vent: ventricles.	83
7	Calculated diffusivity constants across interfaces, EC: endothelial cells, TJ: tight junction, Ch: channel.	85
8	transporter coefficients (M) and dissociated coefficients (K).	86
9	S: storage coefficient, α : Biot-Willis coefficient, μ : dynamic viscosity of water, k : permeability coefficient, and ρ : density of water.	87
10	Hydrostatic pressure and osmotic pressure across EC: Endothelial cells, BLM:basolateral membrane, APM: apical membrane, TJ: tight junction. The units are KPa.	93
11	Pathological changes in choroid plexus in ageing. (ABV. EC: Endothelial cells, St: Stroma, CPE: Choroid plexus epithelium, TJ: Tight junction, ATP & NKCC are two enzymes located on APM). Values are found from [93, 135, 43, 126, 60]	101

12	Detailed analysis assessing the impact of stiffened endothelial cells (EC), Stroma (St), and choroid plexus epithelium (CPE) on Q_{PI} : pulsatility index for total CSF production, OP_{APM} : osmotic pressure difference between CPE and vent, HP_{APM} : hydrostatic pressure difference between CPE and vent, OP_{TJ} : Osmotic pressure difference between St and vent, HP_{TJ} : hydrostatic pressure difference between St and vent.	105
13	Investigation of the effect of dehydrated interfaces such as endothelial cells (EC), basolateral membrane (BLM), apical membrane (APM), and tight junction (TJ) on Q_{PI} : pulsatility index for total CSF production, OP_{APM} : osmotic pressure difference between CPE and vent, HP_{APM} : hydrostatic pressure difference between CPE and vent, OP_{TJ} : Osmotic pressure difference between St and vent, HP_{TJ} : hydrostatic pressure difference between St and vent.	106
14	Impact of reduced epithelium size on components of CSF production. Q_{PI} : pulsatility index for total CSF production, OP_{APM} : osmotic pressure difference between CPE and vent, HP_{APM} : hydrostatic pressure difference between CPE and vent, OP_{TJ} : Osmotic pressure difference between St and vent, HP_{TJ} : hydrostatic pressure difference between St and vent. . . .	109
15	Detailed analysis of the significance of ATP and NKCC transporter activities on component of CSF production. Q_{PI} : pulsatility index for total CSF production, OP_{APM} : osmotic pressure difference between CPE and vent, HP_{APM} : hydrostatic pressure difference between CPE and vent, OP_{TJ} : Osmotic pressure difference between St and vent, HP_{TJ} : hydrostatic pressure difference between St and vent.	109
16	Analysis for impact of stiffness of endothelial cells (EC), Stroma (St), and choroid plexus epithelium (CPE) on capillary morphology. The analysis are conducted by studying the alterations in average capillary radius R_m , pulsation of capillary, R_P , average flow rate out of capillary compartment $Q_{m_{out}}$, and average flow rate across EC, $Q_{m_{EC}}$	112

17	Detailed analysis for dehydrated interfaces such as endothelial cells (EC), basolateral membrane (BLM), apical membrane (APM), and tight junction (TJ) on capillary morphology. The analysis are conducted by studying the alterations in average capillary radius R_m , pulsation of capillary, R_P , average flow rate out of capillary compartment $Q_{m_{out}}$, and average flow rate across EC, $Q_{m_{EC}}$	113
18	Impact of in epithelial cells reduction on capillary morphology. The analysis are conducted by studying the alterations in average capillary radius R_m , pulsation of capillary, R_P , average flow rate down the capillary compartment $Q_{m_{out}}$, and average flow rate across EC, $Q_{m_{EC}}$	115
19	Analysis for impact of stiffness of endothelial cells (EC), Stroma (St), and choroid plexus epithelium (CPE) on Choroid plexus volume. The investigations are on the alterations in average CP radius volumetric expansion $\frac{dV}{dt}_m$, its pulsation, $\frac{dV}{dt}_P$, mean radius capillary R_{cap} , mean radius Stroma R_{St} , and mean radius CPE R_{CPE}	117
20	Analysis for impact of dehydration of endothelial cells (EC), basolateral membrane (BLM), apical membrane (APM), and tight junctions (TJ) on Choroid plexus volume. The investigations are on the alterations in average CP radius volumetric expansion $\frac{dV}{dt}_m$, its pulsation, $\frac{dV}{dt}_P$, mean radius capillary R_{cap} , mean radius Stroma R_{St} , and mean radius CPE R_{CPE}	118
21	Analysis for impact of of epithelial cell atrophy on Choroid plexus volume. The investigations are on the alterations in average CP radius volumetric expansion $\frac{dV}{dt}_m$, its pulsation, $\frac{dV}{dt}_P$, mean radius capillary R_{cap} , mean radius Stroma R_{St} , and mean radius CPE R_{CPE}	119
22	Main constituent in blood accounted in this study and their concentrations. The unit is $nmol/mm^3$	121
23	Summarised specifications for model set-up.	126
24	Information about choroid plexus. The geometric specification of choroid plexus (i.e. length, thickness, surface area) are used to estimate the interventricular CSF production choroid plexus in each region of Lateral ventricles (LV), third ventricle (3V), and fourth ventricle (4V). [103, 16, 151]	128

List of Figures

1	Two main regions for neurogenesis in adult brain: the subventricular zone (SVZ) and the hippocampus. Picture adopted from [37].	2
2	Anterior and Lateral views of all cerebral ventricles. The two largest ventricles (coloured in blue) are lateral ventricles that connect to third and fourth ventricles. (picture adopted from [40]).	5
3	Left picture: ventricular surface, which is lined up by loosely connected ependymal cells, right picture: subarachnoid space is bound via pia mater, pictures taken from [51].	6
4	There are four choroid plexuses in the ventricular system, one in each. The figure on the bottom right shows the tight junctions (TJ) in the outer layers of choroid plexus. Picture adopted from [82].	7
5	A cast of the human blood brain barrier comprising of the smallest branches of vasculatures, taken from [51].	10
6	Proposed Glymphatic pathway: CSF enters the arterial paravascular space: a space bounded by pial sheath and glia limitans. This space disappears at the capillary level and CSF enters the brain parenchyma, mixes with the interstitial fluids and bathes the neurones. On the other hand, the CSF flows towards the venous system, where it is bounded between the vessel and glia limitans, finally drains into the blood system. [8]	13
7	Hydrocephalus is associated with fluid accumulation in the CSF system leading to abnormal enlargement of the ventricles,[84].	14
8	Arachnoid granulations are located at the outer layer of cerebral subarachnoid space. Picture taken from [24].	16
9	Scheme of possible routes for CSF drainage: 1) Olfactory bulb 2) Dura mater lymphatic vessels, which would drain into the cervical lymph nodes (CLNs), Picture adopted from [142].	18

10	Schematics of the sites of the barrier interfaces in the adult brain. (a) the blood–brain barrier (BBB): an interface between the cerebral blood vessels and brain parenchyma. (b) the blood–CSF barrier (BCSFB): a barrier between choroidal blood vessels and the CSF. (c) the CSF-venous barrier (CSFVB) is the meningeal barrier separating Pia surface and CSF. (d) the tissue-CSF barrier (TCSFB) is the ependyma cells lining the ventricles [26].	25
11	Morphology of choroid plexus reveals a complex shaped structure residing next to each in parallel form (A-B). A close view from the top shows the epithelial cells covering the entire CP (C). A cross sectional cut through the CP shows a highly vascularised structure (D). Two strands of CP, each contains one capillary embedded in connective tissues and a layer of cuboidal epithelial cells. Pictures are adopted from different sources [122, 28, 146]	33
12	Micro-anatomy of a single strand of the choroid plexus.	34
13	Scheme of different types of capillaries throughout the body. Continuous capillaries have intact endothelial cells and basement membranes. Fenestrated capillaries have continuous basement membrane, however there are perforations in their endothelial cells that allows for transfer of water and molecules (picture taken from [1]).	34
14	Scheme of two epithelial cells that are linked together by tight junction near the luminal surface, taken from [67].	35
15	Schematic picture depicting fenestrated capillary cross section. Choroid plexus capillaries are composed of three layers: glycocalyx layer, endothelial cells with fenestrations, basement membrane. The endothelial cells may join to one another tightly tight junctions, or do not join, leaving a gap (i.e. intercellular clefts). The diaphragm covers the inner side of the pores, but not the clefts.	36
16	Proposed models for three different paracellular transport: (top-left) mechano-diffusion model, (top-right) electro-osmosis model, (bottom) and claudin model. Picture adapted from [28].	54

17	Membrane transport proteins. Top: Channel protein, Bottom: Carrier protein	54
18	Proposed model by Damkier for the transcellular isotonic transport across CPE, [28].	57
19	Highly expressed AQP1 water channels on the apical membrane [28].	58
20	Proposed computational domain for one strand of choroid plexus (CP). The microscopic model consists of all 7 media that make up the CP: capillary, fenestrated endothelial cells, loose connective tissues, basal membrane, epithelium, apical membrane and tight junction.	63
21	The sketch depicts one unit of CPE with all the protein transporters on membrane.	69
22	Inlet and outlet conditions for the model. Top left: inlet profile for pressure distribution at capillary. Top right: outlet profile for pressure distribution at ventricle. Bottom: flow inlet profile at capillary inlet.	78
23	Concentration of sodium (Na), potassium (K), bicarbonate (HCO_3), calcium (Ca), and magnesium (Mg) in blood (Cap), Stroma (St), Choroid plexus epithelium (CPE), and ventricle (vent). The concentration values shown in blue are the inlet condition, the black ones are obtained from the model, and the red ones are found from literature [28]. Unit: milimollar (mM).	89
24	The pressure waveforms in different compartments in choroid plexus, capillary (Cap), Stroma (St), choroid plexus epithelium (CPE), and Ventricle (vent).	91
25	Predicted pressure in Stroma (St) and choroid plexus epithelium (CPE). The figure on the left shows the evolution of pressure from a normal case to an abnormal case of thickened endothelial cells. Right figures show the steady state solutions of pressures for one cardiac cycle in normal vs abnormal case.	92
26	(a) Total water flux for 3 seconds & (b) CSF pulses for 1 second across endothelial cells (EC), Basolateral membrane (BLM), apical membrane (APM), and tight junction (TJ)	94

27	Compare the two proposed sources of pulsation from choroid plexus. (a) CSF production pulsation & (b) volumetric expansion pulsation. The latter is four orders of magnitude larger than the former, hence more likely to be pulsating source.	95
28	Investigating the effect of media stiffness on CSF production. Left: total CSF production for 3 seconds, middle: CSF pulses for 1 second, right: the schematic diagram of the relative percentage difference of mean CSF production between normal and each abnormal condition.	104
29	Impact of interfaces dehydration on CSF production. Left: total CSF production for 3 seconds, middle: CSF pulses for 1 second, right: the schematic diagram of the relative percentage difference of mean CSF production between normal and each abnormal condition.	107
30	Impact of CPE atrophy on CSF production. Left: total CSF production for 3 seconds, middle: CSF pulses for 1 second, right: the schematic diagram of the relative percentage difference of mean CSF production between normal and each abnormal condition.	108
31	Effect of ATP and NKCC transporters on CSF production. Left: total CSF production for 3 seconds, middle: CSF pulses for 1 second, right: the schematic diagram of the relative percentage difference of mean CSF production between normal and each abnormal condition.	110
32	Impact of CPE stiffness on capillary morphology (left) and its pulsation (right).	112
33	Impact of endothelial cell dehydration on capillary morphology (left) and its pulsation (right).	113
34	Impact of CPE atrophy on capillary morphology (left) and its pulsation (right).	114
35	Comparison between the CSF efflux across endothelial cells (left) and CSF efflux down the capillary (right) for normal (black lines) and in CPE atrophy case (purple line).	115
36	Impact of CPE stiffness on total choroid plexus volumetric change (left) and its pulsation (right).	117

37	Impact of endothelial cell dehydration on choroid plexus volumetric change (left) and its pulsation (right).	118
38	Impact of epithelium atrophy on choroid plexus volumetric change (left) and its pulsation (right).	119
39	Sagittal view of the brain: the four lobes and ventricular system. The anterior horn, body, posterior, and inferior horns of the lateral ventricle are located in the frontal, parietal, occipital, and temporal lobes. Associated functions of lobes: Frontal:thinking, memory, & movement. Parietal: language and touch. Occipital: sight. Temporal: hearing, learning and feelings.	123
40	Views of real cerebral ventricles obtained from MRI 5-year old boy. From left two right: Coronal, Sagittal, and Horizontal planes.	126
41	Coronal (left) and Sagittal (right) views of the reconstructed geometry of lateral ventricles. black mesh represent the surface area of the LVs, the regions marked in red are the choroid plexuses (i.e. inlet flow sites), and the blue mesh is represents the outlet.	127
42	Streamlines illustrating the path that each particle travels from the production source (choroid plexus) to the outlet.	129
43	Velocity contours, top left: Sagittal plane, top right: Horizontal plane from bottom, bottom right: Horizontal plane from top, bottom left: coronal plane from the back. The figure is colour coded: red represents highest velocity and blue the lowest velocity.	131
44	Pressure contours, top left: Sagittal plane, top right: Horizontal plane from bottom, bottom right: Horizontal plane from top, bottom left: coronal plane from the back. The figure is colour coded: red represents highest pressure and blue the lowest pressure.	132
45	Shear stress contours, top left: Sagittal plane, top right: Horizontal plane from bottom, bottom right: Horizontal plane from top, bottom left: coronal plane from the back. The figure is colour coded: red represents highest Shear stress and blue the lowest Shear stress.	133

46	Time dependant pressure signal in the capillary obtained from M1 (circle symbols), M2 (dashed line) and M3 (solid line).	139
47	Comparing the solutions of flow rate in capillary obtained from M1 (circle symbols), M2 (dashed line) and M3 (solid line).	140

1 Introduction

Human brain is one of the most complex structures in the universe. This organ of approximately 1.5 kg weight, coordinates our actions, senses, emotions, and cognitions; in short, it defines who we are. Although it has been studied for over a century, its behaviour in health, disease, or even after treatments remains a mystery. According to World Health Organisation (WHO), 6.8 million people die every year from neurological conditions, yet in most cases, neither the onset nor the primary cause of these conditions is known [113]. In general, the brain is composed of three main systems: parenchyma (i.e. brain tissue and its fluid), vasculature (i.e. blood and lymphatic vessels), and ventricular domain. The latter refers to four interconnected cavities inside the brain where a fluid called cerebrospinal fluid (CSF) circulates. CSF is a water-like substance that promotes the brain's well-being by providing hydromechanical and biochemical support. The hydromechanical protection of the brain via CSF is through two mechanisms: first, it acts as a shock absorber and guards the brain against the inside and outside forces such as tumour growth or accidental impacts [147]. The second (i.e. biochemical) role of CSF is to maintain brain homeostasis by regulating the composition and volume of the interstitial fluid (i.e. fluid surrounding the brain cells), which is imperative for maintaining normal neuronal functioning [147].

The physical interrelation between brain parenchyma (i.e. brain tissue) and CSF domain (Figure 2) enables one system to impact the other; on one hand, CSF interacts with the brain parenchyma and facilitates the exchange of necessary solutes and nutrients with the brain tissue. On the other hand, it acts as an excretory pathway for metabolite wastes, unwanted proteins, excess neurotransmitters, bacteria, and viruses [52, 58].

Cerebrospinal fluid also plays a significant role in the development and organisation of the brain through neuronal guidance. Until 30 years ago, it was generally accepted, by the neurosciences communities, that developed brains do not generate new neurones (neurogenesis). Today, it is clear that neurogenesis (i.e. the birth of neurones) occurs in two areas in the adult brains: the subventricular zone (SVZ) and hippocampus (Figure 1) [152]. These newborn neurones migrate in the SVZ to reach the olfactory bulb, where they mature into local neurones. These neurones then have the potential to enable brain

self-repair after injuries caused by stroke or neurodegenerative disorders [4, 37]. A recent study shows that these new born neurones in SVZ follow the flow of CSF in the adult brain to reach the olfactory bulb; any disturbance in the CSF flow strongly affects the migration in the SVZ [124].

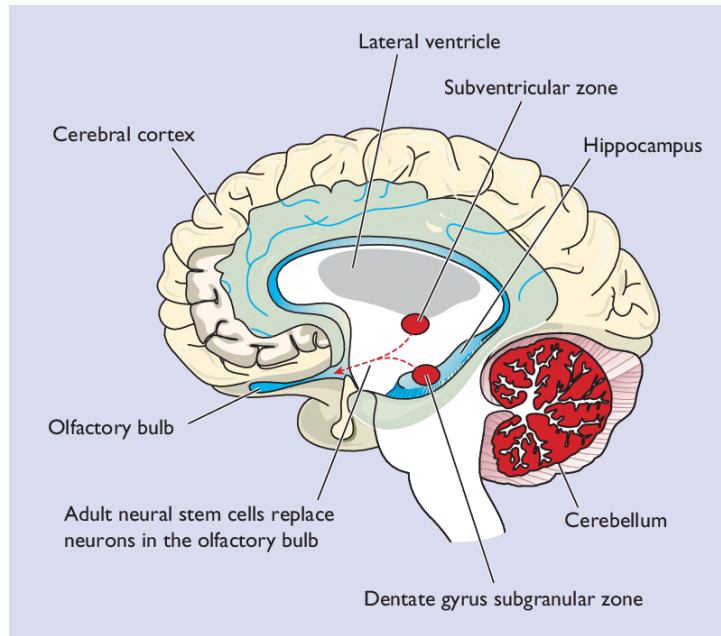


Figure 1: Two main regions for neurogenesis in adult brain: the subventricular zone (SVZ) and the hippocampus. Picture adopted from [37].

In addition to the aforementioned roles of CSF, this multi-functional fluid is used in medical fields for diagnostic purposes [65]. Cerebrospinal fluid is composed of approximately 99.13% water and 0.87% of solutes such as sodium, potassium, calcium, magnesium, chloride, albumin, amino acids, etc. This composition is finely regulated, and its variation is widely used for diagnostic purposes of a wide range of brain abnormalities (e.g. Infections such as meningitis, autoimmune disorders such as multiple sclerosis, brain tumours, and bleedings in the brain). For instance, xanthochromia (i.e. yellowish appearance of CSF), which is a product of red blood cell degeneration, indicates haemorrhage in the system. Another use of examining CSF sample is to count the number of cells in order to spot certain abnormalities. Normal cell count of CSF is approximately 5 per millilitre; an increase in cell concentrations (e.g. immunoglobulins) may be an indication of infection or the onset of autoimmune disease [147].

Disruption in normal CSF physiology (i.e. flow or/and composition) is closely attributed to development of various neurological disorders such as hydrocephalus, Alzheimer's disease, and Chiari malformation [48, 149, 61]. Therefore, targeting and manipulation of cerebrospinal fluid system can be beneficial in discovery and monitor of variety of neurological conditions (e.g. spread of brain cancer) and transport of drugs (i.e. drug delivery) into the brain [127].

1.1 Aims and outline of the thesis

Despite the important role of CSF, a significant aspect of this system has remained unknown. Therefore, the ultimate aim of this work is to take a step towards better understanding the system. We fulfil this aim by conducting mathematical and computational studies. The outline of this thesis is organised in six chapters as described below: **chapter 2** is dedicated to describing the gross anatomy of CSF domain (i.e. brain ventricles), followed by two subsections that review the literature and studies conducted to understand the physiology and pathophysiology of CSF systems. One aim of such extensive review is to provide the reader with an insight about conjectures, misconceptions and disagreements that exist in every aspect of the CSF system, from its production to circulation and absorption. Subsequently, we build a foundation for explaining the the research gap and conclude the chapter by emphasising on the motivation behind our investigation and set objectives.

In **chapter 3**, we initiate investigating the production of CSF. Hence, the chapter starts with a background on the micro-anatomy of one system that produces CSF. i.e. Choroid plexus (CP). Since the system is composed of three distinctive organs, we explain the related physiology of each organ and their physics separately to mathematically model them, as isolated organs. The reason behind formulating them isolatedly is that each of these organs is found in different parts of body, but either have never been mathematically modelled or only certain aspects of them have been modelled. Consequently, it will set a firm foundation for the following chapter.

Chapter 4 introduces the first ever developed holistic mathematical model mimicking

the Choroid plexus and CSF production. First, we utilise the driven equations for each isolated organ in the previous chapter, finalise them in a holistic setup to mimic CP, introduce the governing equations and apply the numerical methods to solve the system. The obtained results are validated against the data provided in literature. The main purpose of this chapter is to understand the system in health and provide a baseline for investigating abnormal scenarios.

In **chapter 5**, we evaluate and analyse the system in other scenarios such as healthy ageing and its relation to development of various neurological conditions. We aim to provide new insights about the impact of the different conditions on the mechanics of CP and CSF production.

In **chapter 6**, we start investigating the circulation of CSF in a realistic geometry which is acquired by conducting MR imaging. The 3D simulation is done by taking advantage of commercialised software. Flow dynamics are analysed and results are discussed.

Chapter 7 outlines the main findings related to the set objectives, summarises the work done in each chapter and highlights the contributions of the study. It concludes with the future directions that can be taken.

2 Literature Review

2.1 Gross anatomy of CSF domain

The CSF domain is a set of multi-compartmental interconnected cavities located in brain and provides a route for CSF circulation. The overall anatomy of this system can be classified into ventricular (i.e. internal to the brain tissue) and the subarachnoid spaces (SAS) (i.e. external to the brain tissue). Figure 2 depicts the ventricular CSF system: the two largest cerebral ventricles are the lateral ventricles (LVs), one in each cerebral hemisphere. These ventricles join the third ventricle (3V) through narrow pathways called the foramina of Monro (FOM). The third ventricle subsequently connects to the fourth ventricle (4V) via the cerebral aqueduct (AQ). Fourth ventricle, then, extends into two separate pathways: one connects the fourth ventricle to the cerebral subarachnoid space (via foramen of Magendie) and the other one to the spinal subarachnoid space (via the foramina of Luschka).

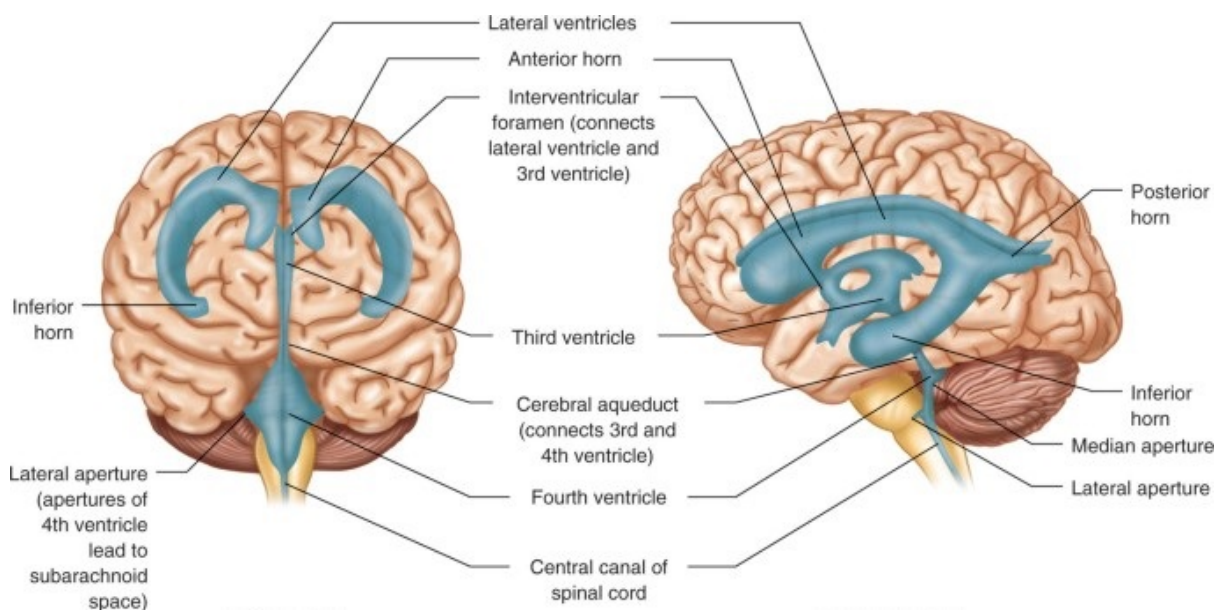


Figure 2: Anterior and Lateral views of all cerebral ventricles. The two largest ventricles (coloured in blue) are lateral ventricles that connect to third and fourth ventricles. (picture adopted from [40]).

The ventricular systems are lined up by a continuous layer of ciliated epithelial cells called ependymal cells. These cells form a tissue-CSF barrier and they lack tight junctions,

hence, facilitating fluid exchange between the CSF domain and brain parenchyma. In addition, the subarachnoid spaces are separated from the outer surfaces via pia mater (Figure 3). Since the focus of this study is on the ventricular system, we will not further discuss the anatomy of the subarachnoid pathways.

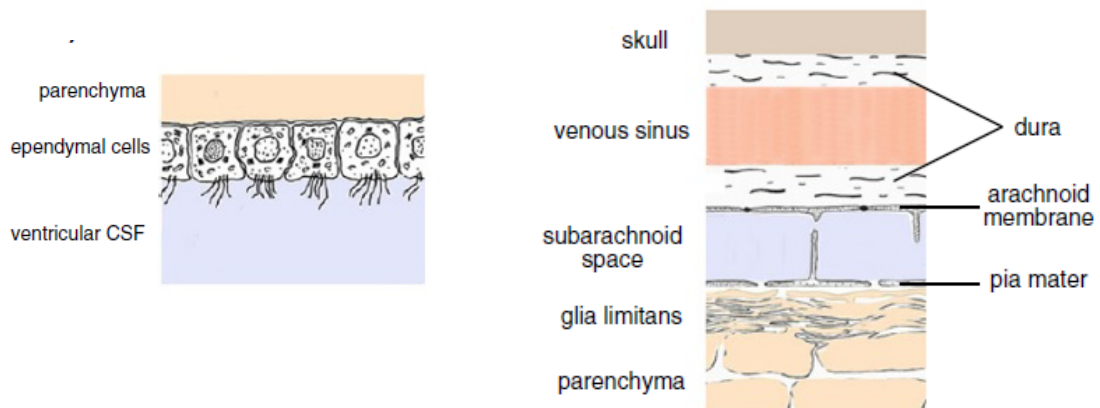


Figure 3: Left picture: ventricular surface, which is lined up by loosely connected ependymal cells, right picture: subarachnoid space is bound via pia mater, pictures taken from [51].

Each ventricle possesses a cauliflower shaped organ called the choroid plexus (CP), which is composed of three main layers. The innermost layer is fenestrated capillaries that are embedded within connective tissue, Stroma. The outer layer of Stroma itself is covered by a specialised form of cells, called epithelial cells (Figure 4).

Choroid plexus (CP) is accepted as one site for CSF production (further discussed in section 2.2). The CSF, that is produced by CP, is believed to be produced in the two relatively large lateral ventricles and flow through the FOM to reach the third ventricle. Then, it circulates through the cerebral aqueduct inside the fourth ventricle, from where a portion flow inside the spinal SAS and the rest travels upward through the cerebral SAS. Most investigators claim that CSF is absorbed into the blood stream via arachnoid granulations (Figure 8). Note that, the explained route for CSF flow is a traditional view and currently there are many controversies about the mechanisms involved in different aspects of CSF system, all of which is discussed in the following sections.

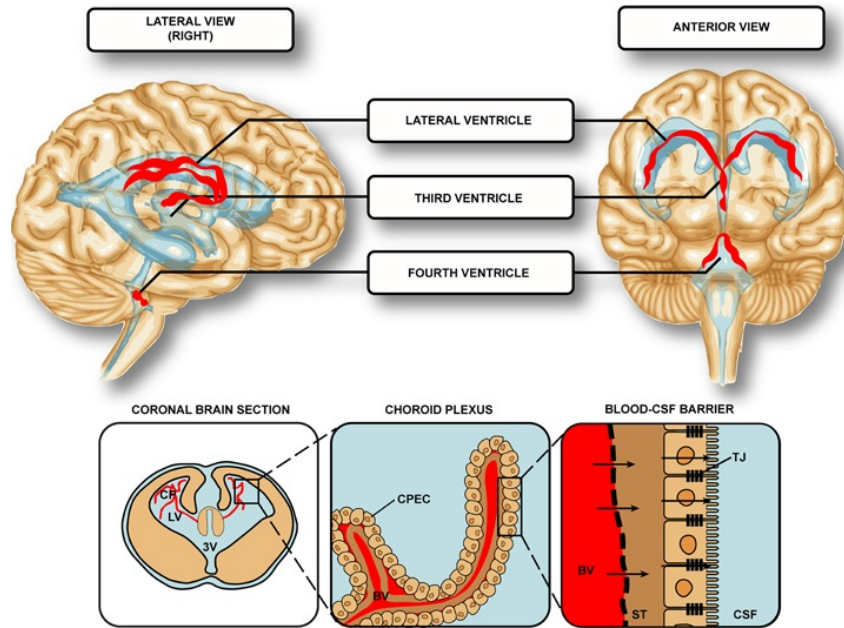


Figure 4: There are four choroid plexuses in the ventricular system, one in each. The figure on the bottom right shows the tight junctions (TJ) in the outer layers of choroid plexus. Picture adopted from [82].

2.2 Physiology of CSF

Cerebrospinal fluid occupies about 100-150 ml of the brain, 35 ml of which circulates in the ventricular system and the remaining flows in the subarachnoid spaces [122]. At discovery, this fluid was believed to be a simple filtration of blood plasma through choroid plexus. Soon after, Rougemont et al. reported that although the composition of CSF is similar to blood plasma, they differ in some ionic concentration: compared to plasma, CSF has a lower concentration of protein, cells, glucose, calcium, potassium, and bicarbonate, while having higher concentration of chloride, sodium, and magnesium [30, 84]. This observation, turned the attentions to the choroid plexus as the main site for CSF production as an organ that actively produces CSF (active production: involves the use of energy to produce CSF, even against the concentration gradient [51]). Since, the CP is located in the ventricular system, the concepts for CSF circulations inside the ventricular pathways and their absorptions sites via arachnid granulations were formed. Later these views were challenged, which are discussed below.

The following part of the section is divided into three main sub-sections dedicated to describing the physiology of CSF production, circulation and absorption. In each sub-

section, we discuss the conjectures and existing opposing hypothesis, bringing into the reader's attention, the current knowledge gap in the area. At the end of each subsection, there is a block diagram that summarises the discussed materials.

2.2.1 CSF production

CSF production was assumed to be solely an active process, produced at a constant rate (i.e. approximately 0.4 ml/min [110]) and independent of variations in physical quantities (e.g. blood pressure) [110, 84]). This observation was later questioned and modified; CSF production is a combination of filtration and active transport and the production rate is dependent on blood hydrodynamic pressure. i.e. in instances where blood pressure increases, blood flow rate into the intracranial areas decreases, so as the CSF production [122]. Recently, this view is also challenged by researchers whom question the possible effect of osmotic pressure gradient, created by concentration difference between the blood and CSF [17, 28, 51]. According to this new hypothesis, the CSF production is a combination of all three mechanisms (i.e. hydrodynamic pressure, osmotic forces, and active transport).

So far we discussed the mechanisms by which CSF is produced. Now we turn our attention to the question in regards to the main site for this production. Some investigators believe the majority of CSF is produced at choroid plexus, whereas others believe the main production occurs extra-choroidal.

Is choroid plexus the main source for CSF production?

The primary functions of the CP in ventricles is production of CSF. In literature, this production is mainly referred to as a two stage process, a view that we will challenge in Chapter 3. In the first stage, blood plasma passing through choroidal capillaries (located inside the ventricles) will filter through its fenestrated walls and flow into the neighbouring tissue, Stroma. Then, the ultra-filtrate crosses the epithelial cells at the surface of the choroid plexus, and enter the ventricle. It is suggested that 80% of CSF is produced via choroid plexuses and the remaining is produced indirectly by the extra-ventricular sources (argued against in the next subsection). This term, extra-ventricular sources, refers to the indirect production of CSF by microvescature capillaries located inside the

brain tissue. In this production, blood passing through capillaries will filter through its fenestrated walls into the interstitial fluid (ISF) of brain tissue, where they travel to reach the ventricular wall (ependymal cells). Note that this argument can be made on the basis that water is the main constitute of both CSF and ISF.

The conception of the CP as the main site of CSF production is originally based upon an experiment conducted on a single dog by Dandy [29]. In this experiment, the CP in one of the LVs was removed and both pathways between the LVs and third ventricle (i.e. FOM) were blocked; he discovered that the manipulated ventricle collapsed, whereas the other ventricle dilated due to accumulation of CSF. He, therefore, reported that the CP is the main source for CSF generation. However, this conclusion was later criticised since the experiment could not be reproduced by others [14]. For instance, Hassin et al. [50] performed the same experiment as Dandy, and he did not observe any signs for LV reduction after the monolateral plaxectomy; they concluded a different source for CSF production must exist (i.e. indirect production via microvessel capillaries located in brain parenchyma). In addition, some other researchers argued that if choroid plexus is the main source of CSF production, then choroid plaxectomy should reduce the overall CSF secretion; hence some pressure relief for patients with enlarged ventricles (i.e. hydrocephalic patients). However, the results revealed that more than 50% of the patients who received the choroid plaxectomy treatment still required shunt placements due to reoccurrence of hydrocephalus [77].

Additionally, there are other sets of evidences that emphasise on the significance of the CP in CSF production. For instance, it is believed the rate of blood flow to each gram of choroid plexus tissue was found to be 4 ml/min (approximately 10 times greater than the rate of blood flow to the brain parenchyma [137]). This was interpreted to enable choroid plexus to produce CSF at a rate that is very close to the estimated value for CSF absorption [137]; hence, CP produces the majority of CSF. To oppose this view, some investigators argue that the surface area of parenchyma capillaries (Figure 5) are 1000 times more than the surface area of the choroidal capillaries (20 m^2 and 0.02 m^2 , respectively) [28]; therefore, indirect production must be the main source for CSF production and not CP. A recent study, however, states that the surface area of choroidal capillary is significantly more than the previously reported value (i.e. approximately $2\text{-}5\text{ m}^2$), and

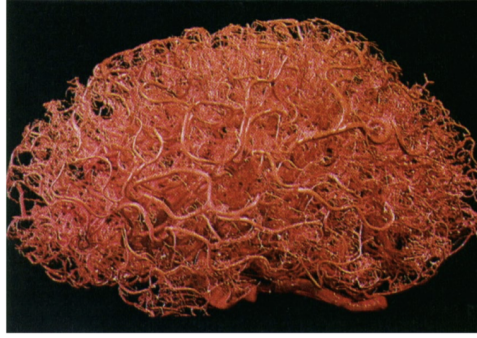


Figure 5: A cast of the human blood brain barrier comprising of the smallest branches of vasculatures, taken from [51].

the capability of CP for CSF production should not be underestimated [137].

CSF is also produced indirectly by extra-choroidal sources

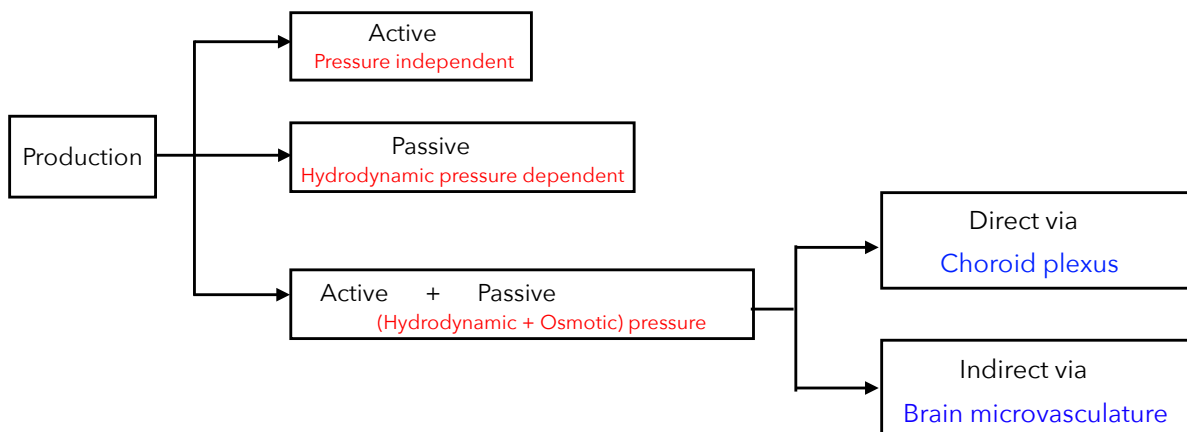
In 1973, Hammock and Milhorat questioned the CP as the main source for CSF production. They argued that choroid plexus removal must affect the CSF composition if CP is the origin for CSF production. They conducted an experiment and reported that the compositions do not significantly change and concluded that the major portion of CSF must be produced elsewhere [97].

These controversies turned the attention of researchers towards the brain microvessels (i.e. capillaries) as the main source for CSF production. Generally, the walls of capillaries (i.e. endothelial cells) in the brain form a dense interconnected network that are tightly connected and do not allow for free movement of large substances across them. This morphological structure of these microvessels enables them to form a barrier between the blood and the brain parenchyma (blood-brain-barrier (BBB)).

These barriers allow for transport of water and some solutes into the brain parenchyma, producing interstitial fluid (ISF). Since water constitutes the major portion of the ISF as well as the CSF (i.e. 99%), and the solute compositions in both (i.e. ISF and CSF) are similar, BBB are hypothesised as the main CSF generator. According to this hypothesis, the arterial capillaries undergo a high hydrostatic pressure during systole; as a result, water and some small solutes (that can pass through the tight junctions) filter across the microvessel walls. However, larger solutes (i.e. proteins) retain in the capillary generating osmotic counter pressure, which opposes water filtration. Hence, some filtered solution

would be reabsorbed back into the capillaries and balance the pressures in the system. The fresh ISF, then can pass across loose ependymal cells lining the ventricular system and mix with the solutes made by choroid plexus and make the CSF. Some investigators argue the possible contribution of CSF production from indirect source is more than 60% [122]. This view is also supported due to the large surface area of the microvessels (Figure 5). However, Brinker et al. argues that BBB are incapable of producing CSF at high rates: the rate of CSF production by the capillaries are substantially lower than production by CP (i.e. 1/100 when normalized for barrier surface area) [14]. Subsequently, this argument is also questioned by researchers based on the new findings related to morphology of BBB. Traditionally it was believed that the production is mainly through the intercellular clefts (i.e. gaps) of endothelial cells. However, the modern understanding of BBB unveiled that the surface of BBB is covered by astrocytes end feet, which have water transporting pores (i.e. aquaporins AQs) that facilitate large water movements across the vessels [14].

Block diagram summary of CSF production



2.2.2 CSF circulation

Similar to CSF production, there are many controversies and misconceptions related to circulation of CSF. It was originally accepted that the CSF flow mainly initiates at lateral ventricles and flow through the left and right FOM to the third ventricle. Next it flows through the aqueduct of Silvius into the fourth ventricle; From where it either exit through the foramen of Lushka into the cerebral subarachnoid space or egressing through foramen of Magendie into the spinal subarachnoid space, and travel towards the absorption sites (discussed in the following subsection). Therefore, many researchers refer to CSF circulation as a unidirectional bulk flow (i.e. like a river) from lateral ventricles to the absorption sites [17, 72]. According to this theory, the pressure gradient between the site of CSF production and the site of CSF absorption enables the CSF circulation [72]. Years later, advances in imaging technology revealed that the CSF flow is not as linear as it was previously described; it, rather, circulates in a pulsatile manner with each heart beat [51]. This observation raised the question related to the origin of the CSF pulsation: does volumetric changes in CP cause the CSF flow pulsation? Is CSF formation the driving force? Do expansion and contraction of parenchymal blood vessels transmit the tissue pulsation into the CSF system? How about cilia beatings? These questions were addressed by researchers, which will be reviewed in the following sections. Note that in recent years, an additional system has been proposed for the circulation of CSF (i.e. Glymphatic system). However, since the focus of this study is on the ventricular CSF, we will barely introduce the pathway. According to this theory, CSF enters the brain parenchyma via a narrow space located between the arterial blood vessels, penetrating the cerebral subarachnoid space, and brain parenchyma. This space is called the paravascular space that disappears at the start of capillaries. Here, the bulk flow of CSF bathes the neurone and washes out the waste products towards the venous system (Figure 6). There exist many controversies and uncertainties about the mechanisms behind the flow circulation in this pathway, which we will not be able to discuss, as is out of the scope of the current study.

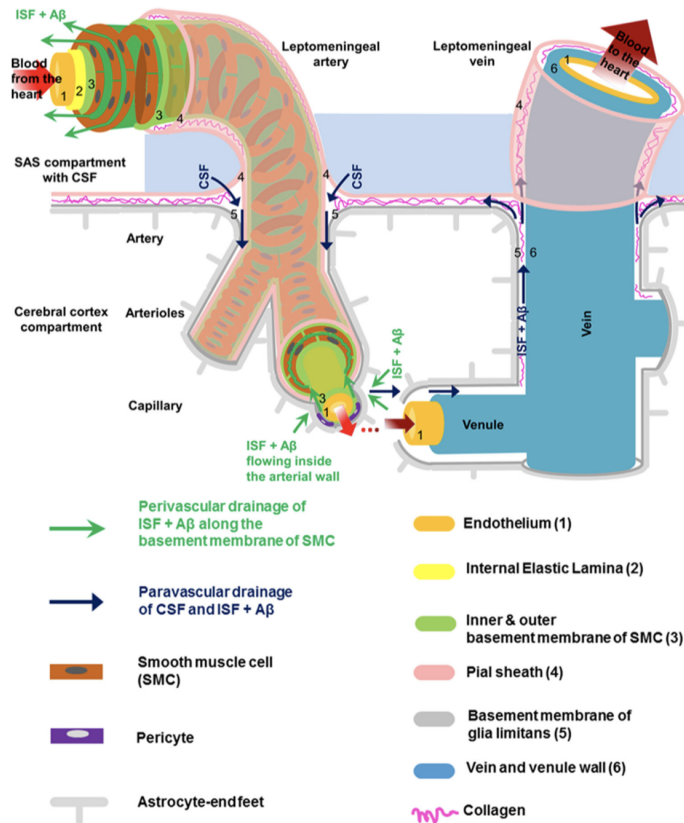


Figure 6: Proposed Glymphatic pathway: CSF enters the arterial paravascular space: a space bounded by pial sheath and glia limitans. This space disappears at the capillary level and CSF enters the brain parenchyma, mixes with the interstitial fluids and bathes the neurones. On the other hand, the CSF flows towards the venous system, where it is bounded between the vessel and glia limitans, finally drains into the blood system. [8]

Controversy 1: CP as the origin of pulsation

Edgar et al. conducted a series of experiments on three dogs in which the pathway for CSF flow was obstructed and hydrocephalus (i.e. enlarged state of ventricles Figure (7)) was developed. They examined the CSF pulsation secondary to arterial pulse and measured the ventricular CSF pulse in the them before and after removing the CP in the lateral ventricles. Then they opened the ventricular pathways in two dogs with their CP intact. They reported the pressure pulses in the ventricles without CP disappeared, whereas the waveform in ventricles with healthy CPs remained unchanged. In another sets of experiments, they performed a unilateral choroid plexctomy in healthy dogs; they recorded the CSF pressure pulse existed in both ventricles, however the pulse was lower in the one with no choroid plexus. In parallel to this experiment, they conducted a

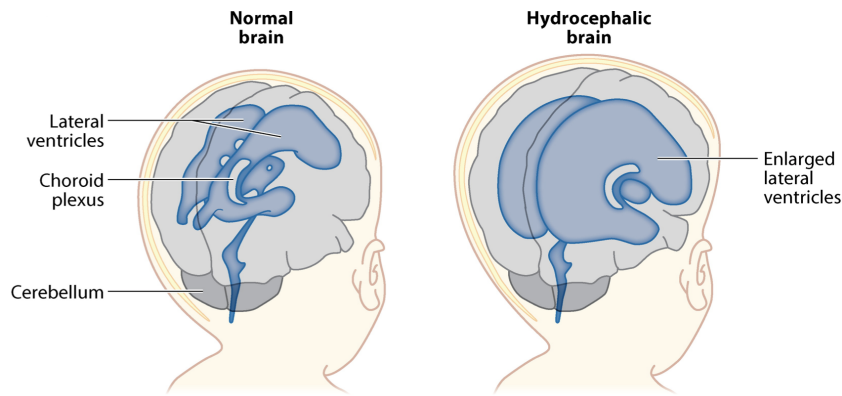


Figure 7: Hydrocephalus is associated with fluid accumulation in the CSF system leading to abnormal enlargement of the ventricles,[84].

unilateral choroid plexectomy procedure on another group of dogs and blocked one of the FOM. They observed no pressure pulse in the ventricle with no CP and plugged FOM, whereas the healthy ventricle presented a normal pulse. They concluded that the choroid plexus is the chief sites of arterial pulsation transfer to the CSF.

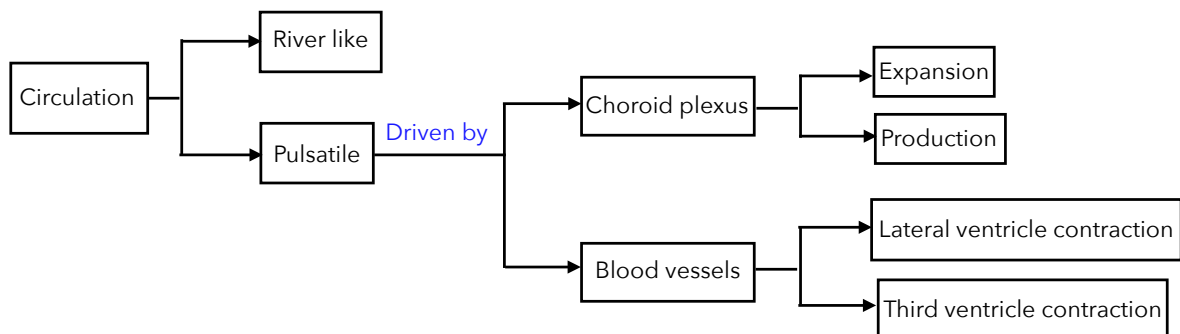
In recent years, the improvement of micro-video probes enabled the researchers to study the morphological changes of the choroid plexus along with the heartbeat. This technique illustrated that the choroid plexus stretches and expands inside the ventricular system and covers a large area [137]. Picard, however, recently reported that he has never observed any significant volumetric changes of choroid plexus through his endoscopic and ultrasonographic examinations [96]. Takizawa et al. conducted a quantitative analysis to study the motion of CSF in vicinity of a widely populated choroid plexus, trigone area (i.e. an area in LVs where choroid plexus is most populated). They reported that there was no significant motion in the site of interest; they reasoned the lack of CSF motion in the area is an evidence to refute the CP as a pulsation site [145].

Despite all arguments above, the role of choroid plexus as a CSF pump is accepted by many researchers and have been utilised their computational studies [95]. For instance, Linninger et.al. developed a computational model with the aim of better understanding the CSF flow dynamics and predicting the CSF pressure and velocity fields in the cranium. In his paper, he refers to expansion of the choroid plexus as the CSF pump; he adds that the CSF production takes place at a constant rate, but the volumetric expansion of CP acts as the driving force for the pulsatile CSF circulation [85].

Controversy 2: Arterial pulsation in brain parenchyma acts as the CSF pump

There is a great body of research suggesting that change in intracranial blood volume during cardiac cycle is responsible for the pulsatile CSF motion in the ventricular system. According to this theory, arterial blood flow into brain parenchyma during systole expand the elastic blood vessels in the brain parenchyma. On one hand, according to Monro Kellie doctrine, the total volume of blood vessels, brain tissue, and CSF is constant and any volume change in one or two system must be compensated by the other system (s). Therefore, at systole, the volumetric expansion of blood vessels must be at the expense of brain tissue and/or volumetric system contraction of CSF domain. In this theory, the brain tissue is assumed incompressible, hence its volume remain unchanged. Therefore, as the consequence of vascular expansion, the ventricles contract and the resulting force causes a portion of CSF is displaced inside the ventricular system [39]. This theory is widely accepted by many researchers [12, 39] and incorporated in many computational studies [83, 143]. Du Boulay agreed on the concept that the CSF pulsation originates from the arterial expansion located in the parenchyma. He, however, doubted that this expansion would be transmitted to all the ventricular system. He reported that the pulsation in the lateral ventricles have small amplitude and possibly do not drive the force. He extended his examination to the pulsations in third ventricle and claimed that pulsation of large arteries near thalamus causes the third ventricle to squeeze [33]. This view was later examined and refuted by Feinberg et al. who reported the role of lateral ventricles in the CSF circulation is unquestionable [39].

Block diagram summary of CSF circulation



2.2.3 CSF absorption

Before explaining the absorption routes, please note that this aspect of CSF is not extended in our study. However, we include it in the section for providing a complete overview of the CSF flow.

Cerebrospinal fluid is believed to egress the cerebral subarachnoid space via arachnoid granulation (Figure 8, [20]), which itself protrudes into superior sagittal sinus (SSS); hence the blood system.

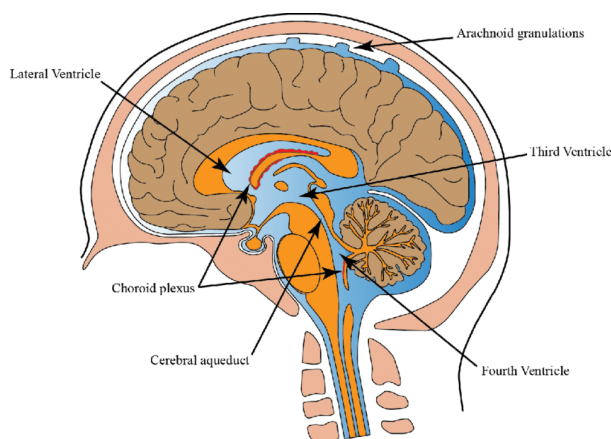


Figure 8: Arachnoid granulations are located at the outer layer of cerebral subarachnoid space. Picture taken from [24].

Under normal physiological condition, this absorption is passive and dependent on the balance between the hydrostatic pressure in the CSF system and the blood in the SSS. Although, this organ has been established as the major route for CSF absorption, there are some opposing opinions. An early experiment was conducted by Key and Ro noted that a coloured- injected gelatine in CSF space would leave the arachnoid granulation into the SSS. This experiment was questioned since the dye injection happened at high pressure (60 mmHg which is out of normal range; 9-13 mmHg). It was argued that such high pressure might have ruptured the granulations to enter the SSS. Weed modified the experiment and injected dye at physiologically normal range; he reported there is no trace of the die found in the arachnoid granulations [91].

Another disagreement on this hypothesis is that this structure (i.e. arachnoid granulation) does not exist in infants and young children and its formed after 18 months. This argument was also challenged by microscopic studies, which showed the existence of the

arachnoid villi; the microscopic size of an organ which later in life forms into arachnoid granulations [98, 70].

What are the alternative proposed routes for CSF absorptions?

Other sites have been proposed as the main CSF turnover site: Choroid plexus, BBB, and lymphatic systems. Choroid plexus, which is suggested as a CSF production site, is also proposed as an absorption site. This hypothesis is mainly based on two observations: 1) CSF is absorbed via choroid plexus if the osmolality of the fluid is increased; 2) in hydrocephalic patients. Both views were argued against on the basis that the choroid plexus may absorb a small portion of CSF under abnormal conditions, however the structure cannot be responsible for the all CSF absorption. Matsumae et al. notes that after this argument experiments regarding CP as the main absorption sites were not conducted since 1921 [97].

Similar to the theories for the CSF production via microvessels, these barriers have been proposed as the CSF absorption sites. According to this hypothesis, the ventricular CSF can cross the ependymal cell, interact with the brain parenchyma, and subsequently be absorbed inside the microvessels. Bulat et.al. infused H-water (similar colloidal feature as water) into the lateral ventricles on observed that the water does not flow into the SAS, but it sharply is absorbed through the periventricular capillaries. They argued that the venous concentration of 3H water rapidly increased, whereas the CSF and arterial concentration remind unchanged.

Cervical lymph nodes (CLN) located in the neck (Figure 9) have been strongly suggested location as CSF absorption site. In 1993, Mortensen and Sullivan injected a radiocontrast medium into the CSF system of a dog and they observed the substance entered the cervical lymphatics and concluded the CLNs were the CSF drainage sites [105]. However, the route that the CSF takes to be absorbed into the CLN is dubious. There are two potential pathways proposed: 1) the olfactory/ nasal lymphatic vessel, 2) the dura mater lymphatic vessels (Figure 9). In the former route, CSF in the brain parenchyma flows towards the cerebral subarachnoid space running in parallel to the olfactory bulb passing through the cribriform plate to reach the CLN. This observation was concluded by many experiments in which different substances (e.g. radiocontrast agent and ink, leucocytes)

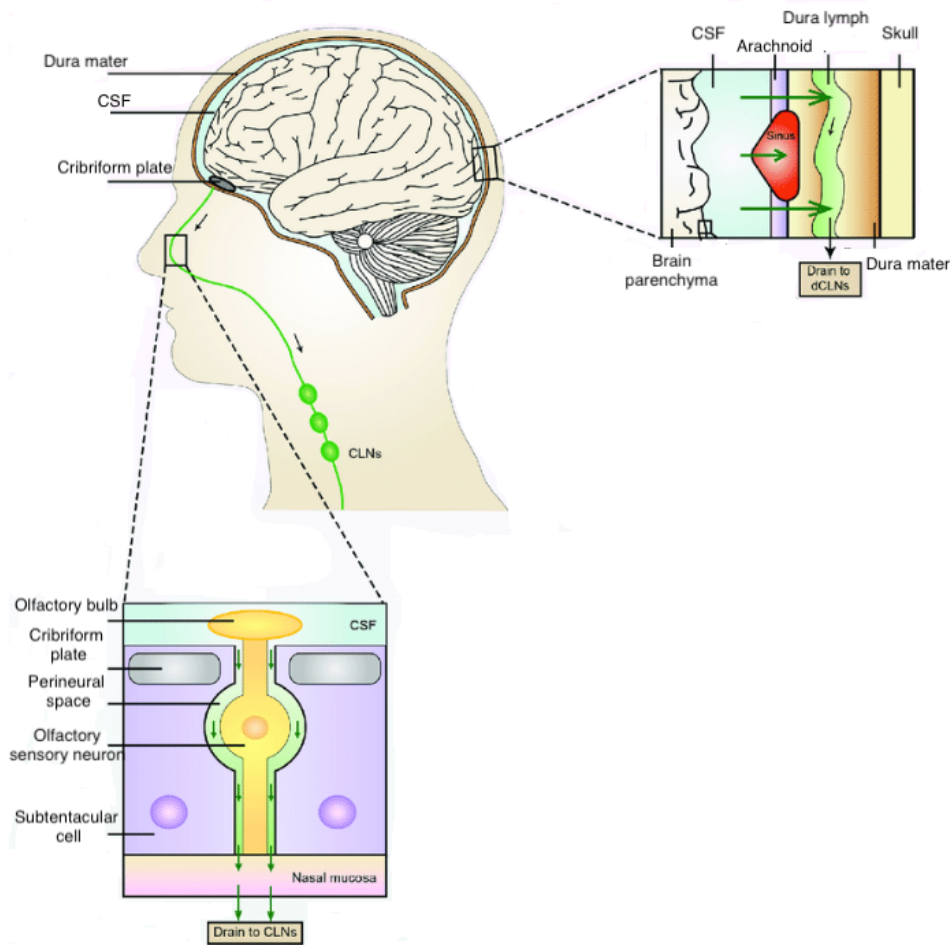
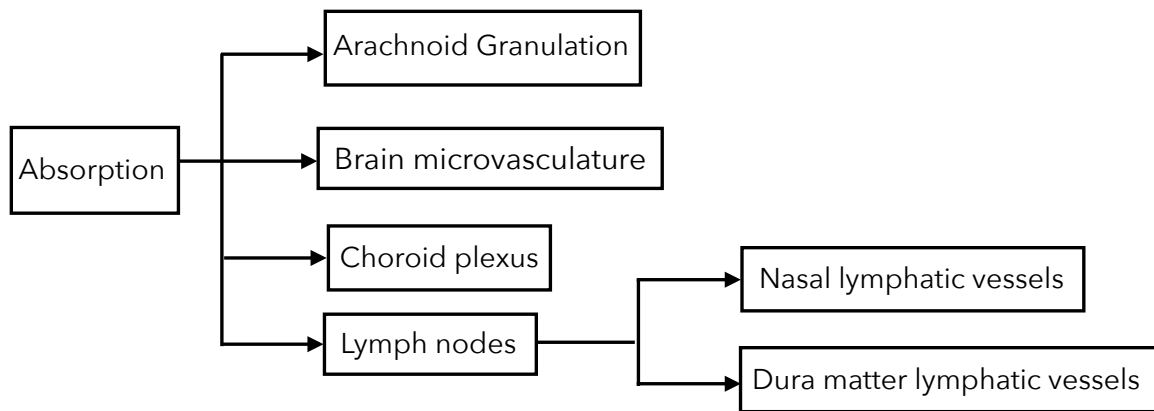


Figure 9: Scheme of possible routes for CSF drainage: 1) Olfactory bulb 2) Dura mater lymphatic vessels, which would drain into the cervical lymph nodes (CLNs), Picture adopted from [142].

were injected into the brain parenchyma and the pathway was marked as the only route for CSF drainage into CLN [73, 108]. In 2015, the discovery of the lymphatic vessel in the vicinity of the venous sinus opened an opportunity for researchers to propose another pathway for the CSF drainage into the CLN. These vessels are located near the Dural sinuses and meningeal arteries and provide a route for direct CSF drainage from the cerebral subarachnoid space into the dura mater lymphatic vessels and CLN (Figure 9). Researchers infused dye into the ventricles and observed the appearance of the substance into the Dural lymphatic vessels and concluded these vessels are populated at the base of skull [88].

Block diagram summary of CSF absorption



2.3 Pathophysiology of CSF

Cerebrospinal fluid role in preserving the central nervous system is unique. It provides a system by which the necessary nutrients and ions enter the brain, the waste products excrete the brain, and bathes the neurones in a chemically stable environment [136]. Therefore, it is not surprising that the alterations in the CSF hydrodynamic and/or composition may lead to onset of various neurological disorders (e.g. hydrocephalus (HC), Alzheimer's disease (AD), and multiple sclerosis (MS)) [61]. In the following, we will discuss the abnormalities which may cause disturbance in any of the aforementioned CSF system (i.e. production, circulation, and absorption). Note that the discussion is to provide an insight about the possibilities that may occur due any abnormalities, however these three mechanisms are interconnected and interruption in one mechanism would subsequently affect the two others. For instance, CSF overproduction incident may affect the normal circulation and possibly the absorption.

2.3.1 Interruption in CSF production

Disruptions in the production of CSF can be a result for or subsequently a cause of several medical conditions such as ageing, infections, tumours, and hydrocephalus. A study done by Wostyn reported that caffeine intake can alert the activity of transporters in the choroid plexus (the transporters are described in Chapter 3), hence mediate the CSF production. It was noted that acute intake caused CSF underproduction, whereas chorionic intake resulted in CSF overproduction in the ventricles [159]. Another factor affecting the CSF production is the presence tumours in the CP. It has been postulated that tumours may obstruct the flow of solutes and water into the ventricular systems and result in CSF underproduction or overproduction; in either case, an imbalance between the production and absorption of CSF is observed (i.e. hydrocephalus). In addition, hypertension (i.e. high blood pressure), a medical condition that is highly reported in adults, has been attributed to breakdown of BBB by increasing its permeability to solutes and leakage of water, leading to CSF overproduction across the ependymal cells [99]. Literature widely refers to the outer layer of choroid plexus, choroid plexus epithelium (CPE), as a barrier between blood and cerebrospinal fluid (i.e. Blood-CSF barrier or

BCSFB) (discussed in detail Chapter 3). This structure stands a gatekeeper for harmful solutes and unwanted proteins, while serving the CSF with nutrients and immune cells. In healthy brains, the BCSFB allows for peripheral immune cells entry into to circulate into various locations (e.g. ventricular system), however these immune cells do not penetrate into the brain parenchyma. Breakdown of BCSFB may allow for some destructive cells (i.e. T cells) to enter the brain parenchyma and engage with the degeneration of brain neurones, which cause multiple sclerosis (MS) [129].

2.3.2 Interruption in CSF circulation

The three-mechanism involved in CSF flow dynamics (i.e. production, circulation, and absorption) are linked; a condition affecting one will impact the two others as well. Nevertheless, it can be claimed that the interruption in CSF production or absorption will have a major impact on the circulation. The abnormalities in CSF circulation is often associated with intracranial pressure (ICP) rise, which in turn results cell death and inflammatory neurones responses . Also, it is responsible for ependymal cell shedding and that results in ventricular expansion [70].

Various pathological conditions such as aqueduct stenosis, interventricular haemorrhage, and infection can cause obstruction in the CSF pathways (i.e. FOM, AQ, etc). CSF flow blockage may alter CSF pulsation, CSF composition and its mixing. This pathological condition is believed to be the most frequent aetiology for hydrocephalus (i.e. 95%) [13]. Furthermore, the CSF circulation clears debris from the ependymal surface of ventricular walls and prevent deposition [131]. The deposition of solutes has not been reported in any studies, to the best of our knowledge, and we suggest it is due to the fact that it is not easy to be detected by imaging techniques. Nevertheless, it may impact dynamics of the flow by changing the wall shear stresses, adding extra surface roughness in such complex geometry, and creating bumps on the surface wall; all of which will affect the local CSF dynamics.

2.3.3 Interruption in CSF absorption

Reduction of CSF turnover rate is postulated to attribute to accumulation of solutes in the brain and lead to neurodegenerative disorders. This pathological condition can

be due to infection, meningitis, subarachnoid haemorrhage, and aggregation of debris at arachnoid granulations.

Decreased CSF absorption will lead to communicating hydrocephalus; a state of enlarged brain ventricles, in which cerebrospinal fluid can circulate in all ventricles, but malformed at arachnoid granulation. In addition, giant arachnoid granulation is a name given to a pathological disorder in which, the arachnoid granulations grow larger than 1 cm. It is postulated that this condition is a response to increasing CSF volume turnover, pressure, and altered CSF pulsations [150].

Deposition of various macromolecules and waste products in the brain parenchyma are postulated to be result of impaired clearance. Recent investigations claim that alterations in CSF turnover is the main cause for aggregation of amyloid beta, the solute responsible for setting of the Alzheimer's disease (AD). Failure of clearance routes such as BBB and lymphatic nodes may be responsible for accumulation of cerebral amyloid angiopathy (CAA), a pathological feature associated with cognitive impairment in AD [87] .

2.4 Motivation and objectives

In recent years, the significance of cerebrospinal fluid has become more evident and motivated investigators in different fields (e.g. neuroscience, cell biology, physiology, engineering) to study this fluid in more detail. The motivation behind such investigations is to understand the CSF system, its flow dynamics and biochemistry, since traces of CSF dysfunction is found in various neurological conditions, such as hydrocephalus, Alzheimer's and Parkinson disease [61, 60, 113, 74]. These neurological conditions have been known for centuries, yet their aetiology have not been fully understood, and in most cases, there is no cure. One reason is that the onset of the conditions is usually subtle and imperceptible. They develop slowly over years and symptoms appear when the brain has undergone irreversible damages. According to Alzheimer's society, subtle signs of Alzheimer's disease in thinking and memory appears upto 18 years prior to formal diagnosis [118].

Current approaches to tackle these disorders and diseases include medical interventions (e.g. medications, surgical treatments, etc), which enables patients to control their health problem and lessen their symptoms. However these treatments can have complications. In some cases, since neurological conditions have overlapping symptoms (e.g. headaches, loss of muscle strength, memory loss, etc), it is common to be misdiagnosed [41] and inappropriately treated. Recent studies found that between 12%-23% of patients diagnosed with Alzheimer's disease (AD) did not show sufficient AD pathology at the autopsy [41]. Other forms of complications arise from the effectiveness of the treatments. For example, there is a condition called hydrocephalus, which is associated with abnormal accumulation of CSF in the ventricular system. The most commonly used treatment for hydrocephalus is CSF shunts: a tube inserted into the ventricular system, which diverts excess CSF into a circulatory system (e.g. abdominal area). Although shunting provides relatively fast pain relief, most hydrocephalic patients undergo multiple surgeries in their lifetime [155]. A relatively recent study reviewed the shunt revision rate and published approximately 46% of patients relying on shunt underwent shunt revision, 65% of which within the first six months postoperatively [90].

Another reason for the lack of cure or effective treatment is that the CSF system is very unknown, even in health: there are conjectures and disagreements in almost every aspect

of this system (refer to subsection 2.2), and the system has been overlooked. i.e. Solar et. al. argues that choroid plexus is among the least studied structure in the brain [135]. Therefore, to improve understanding of abnormal conditions, possibly finding cure or improve treatments, we must fill the current fundamental knowledge gaps.

In recent years, there has been a growing body of research emphasising on the potential of the CSF system for other therapeutic purposes such as drug transport. In general, accessing and targeting the brain to overcome related diseases, is one of the most challenging problems encountered in medical fields. One reason is the four barriers that exist in the brain, which separate the three systems (i.e. blood, tissue, and CSF). In health, these barriers protect the brain against intrusion of unwanted substances (i.e. viruses, bacteria, cancer cells, etc) into another, synchronously do not allow for the transport of drugs into different parts of the brain. These barriers are: blood-tissue, blood-CSF, tissue-CSF, and CSF-venous barriers (Figure 10).

Blood-tissue barrier, which is widely referred to as blood-brain barrier (BBB), is the name given to the walls of blood microvasculature located in brain parenchyma that restrict the movements between the blood system and the brain tissue. The blood-CSF barrier is the outmost layer of the choroid plexus which is lined up by epithelial cells. The tissue-CSF barrier is essentially ependymal cells lining the ventricular surface, separating CSF and brain tissue. Finally, the CSF-venous barriers are located in subarachnoid spaces (near the brain skull) separating Pia mater and CSF.

Regardless of the above argument, the necessity for drug transport into the brain has led researchers to target these interfaces [62, 141, 115]. Among the four, BBB is the most studied one [141, 26]. The biggest advantage of transporting drugs via this route is its location that promotes access to brain tissue. Hence, targeting cancerous cells, tumours, and viruses located inside the brain parenchyma is reasonable via this approach. One disadvantage of transporting drug via this route is that the gap junction at BBB are very tight (i.e. approximately 150 *nm*). This characteristic facilitates the penetrations of only small molecules and stops 95% of appropriate molecules [31].

There are two other popular routes that can provide similar support to the brain; both of which include CSF system. The first approach targets the CSF system via choroid plexus: the transport take place from systemic blood circulation to the choroidal cap-

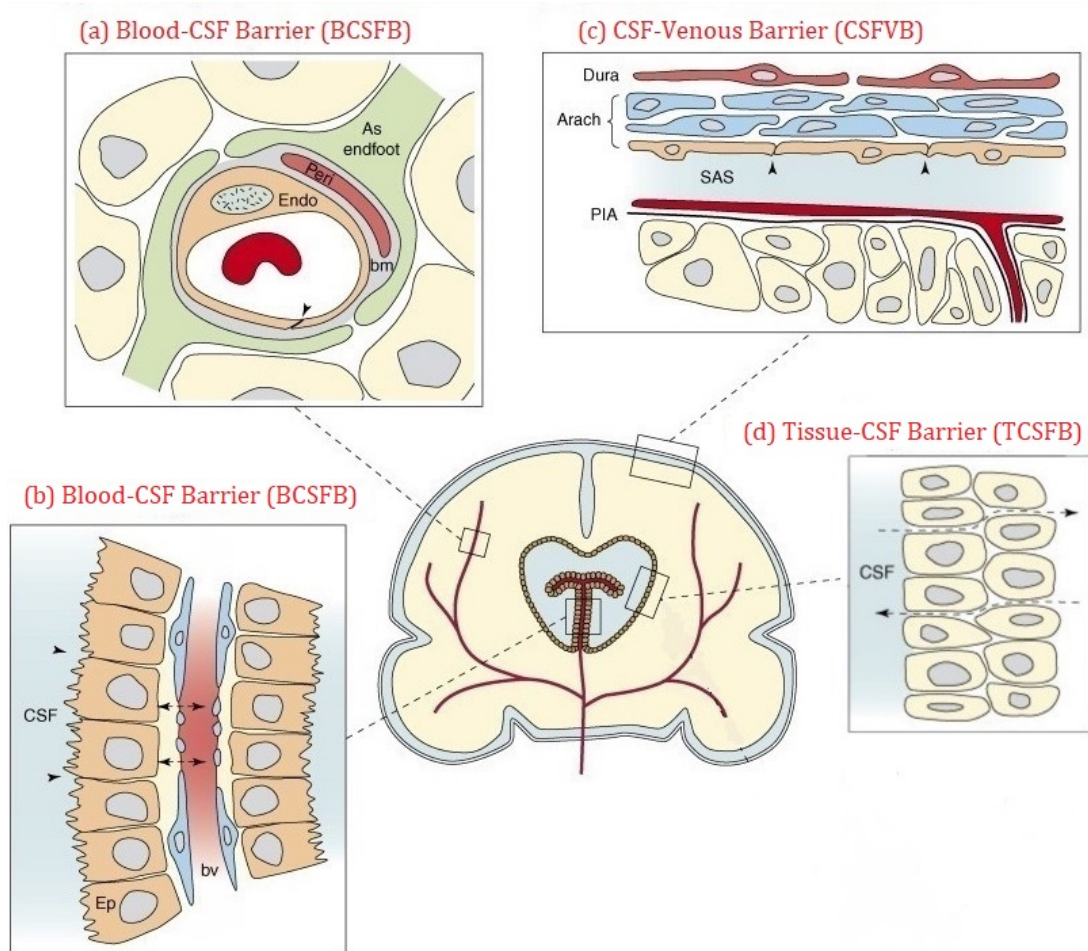


Figure 10: Schematics of the sites of the barrier interfaces in the adult brain. (a) the blood–brain barrier (BBB): an interface between the cerebral blood vessels and brain parenchyma. (b) the blood–CSF barrier (BCSFB): a barrier between choroidal blood vessels and the CSF. (c) the CSF–venous barrier (CSFVB) is the meningeal barrier separating Pia surface and CSF. (d) the tissue–CSF barrier (TCSFB) is the ependyma cells lining the ventricles [26].

illaries. In contrary to the capillaries in brain tissue, these vessels lack tight junctions and facilitate transport of molecules at larger sizes. The next stage in this transport is crossing the epithelial cells, which is one of the brain barriers. The gap junctions at this barrier is approximately $15 \mu m$ (100 times larger than BBB) [52]. Once the drug passed the CP and enters the CSF, it can target areas in contact with CSF. i.e. targeting ependymal cells (lining lateral, third, and fourth ventricles), or the brain tissue beneath them [21, 62, 141].

The second approach includes targeting the epithelial cells of choroid plexus to modify its genetic behaviour, manipulat transport of certain molecules, and alter the rate of CSF

secretion [21, 62, 141]. These approach have been suggested for treatments of conditions such as hydrocephalus, Alzheimer’s disease, and choroid plexus papillomas [21, 62, 141]. Given the importance of the CSF system in maintaining health, addressing disease, and facilitating therapeutic interventions, this study aims to shed new light on its fundamental properties. By gaining a more complete understanding of the system in its healthy state, we can begin to identify and characterise aberrations that underlie various pathologies.

Given the vast size and complexity of the CSF system, we have chosen to focus our investigation on two key aspects: the production system within the ventricles, specifically the choroid plexus, and the circulation of CSF. These two interrelated processes are discussed in greater detail below.

2.4.1 CSF production at choroid plexus

When the physiology of this tissue was less understood, the choroid plexus seemed small, passive, and unimportant. Today, it is clear that this tissue is a major site for transport of certain proteins, vitamins, ions, and amino acids to the brain. It also plays a significant role in producing the growth factors (growth factors: naturally occurring substance capable of prompting cellular growth) and contribute to removal of waste products.

In addition, manipulation of the tissue function may hold a great promise for clinical applications. One example is regulation of neurone functioning; neurones are specialised cells located in brain that communicate to one another in order to transmit information across human body. Fast pace communication among neurones (i.e. neuronal firing) is the key for normal human functioning. There are multiple factors that can affect the neuronal firing and slow down the process such as ageing, lack of sleep, eating habits, and onset of various disorders and diseases. However, these neuronal firing can be regulated through manipulation of certain chemical concentration in the CSF domain. For example, it is known that when the concentration of potassium ion in CSF is high, neurones are more easily excited and fire more readily. Calcium and Magnesium are also two other ions transported across the CP, which are believed to affect the neurone firings. Furthermore, it is proposed that some drugs for epilepsy are more effective by increasing the transport of potassium out of CSF through the CP [136]. Therefore, the more is

learned about the flow of solutes and ions across the CP, the better treatments may be proposed.

In addition, recent studies uncovered that supply of certain substances into the brain (e.g. vitamin C) takes place only via CP [63]. Another example is the transport of AIDS-azidothymidine; one of the most effective agents prescribed for AIDS. It is clearly established that the AIDS virus can invade the brain and hide inside the brain [141]. The virus finds shelter from many antiviral drugs, which cannot pass BBB nor BCSFB. As a result, therapies to tackle the virus mainly fail, unless the agents (i.e. drugs) could access the affected areas. However, this agent (i.e. azidothymidine) is capable of crossing the CP and suppress the virus [136].

Additional to the above argument, there are open questions in regards to CP mechanics and its contribution to CSF production. These questions include the significance and contribution of the tissue to CSF production? How much does a normal CP deform in each cycle of heart beat? How much is the production sensitive to the parameters of the CP (e.g. blood pressure, age, imbalance of solutes)? What properties of the solutes play the most important role in the transportation mechanism across the CP? How does the transportation of solutes/water is affected upon introduction of new solutes (e.g. drugs) into the blood?

To address the aforementioned matters and find solid answers to the associated questions, we take advantages of mathematical modelling and conduct the first part of this study (Chapters 3,4, and 5) with the aim of better understanding the choroid plexus. Consequently, the objectives of this study are:

- Developing the first microscopic model of cerebrospinal fluid (CSF) production in a one strand of the choroid plexus (CP). The model incorporates factors such as fluid and solid mechanics, as well as passive and active transport of solutes.
- Studying and analysing the system in a healthy state; characterising the pressure distributions in each compartment, fluid seepage, and examining the origin of CSF pulsation at the production site.
- Assessing the behaviour of the system in conditions such as normal ageing; analysing the impact of parameters such as elasticity, dehydration, cell atrophy, and trans-

porter activity on the choroid Plexus. Additionally, investigating the potential contribution of these factors to the development of neurological disorders.

2.4.2 CSF circulation

The second part of the project relates to the circulation of CSF in ventricular domain. Cerebrospinal fluid circulates in the ventricular domain in a pulsatile manner. The source of this pulsatile motion is the subject of many medical discussion: is it due to 1) the CSF production at CP, 2) CP volumetric expansion and contraction, 3) CSF production at ependymal cells, 4) deformation of the ependymal cell layer, or 5) beating of the motile cilia located on the CSF facing surface of the ependymal cells. In the previous sections, we introduced all the above mechanisms except the ciliary beating.

Motile cilia are micro-scale hair-like extensions on many cell types across the body such as lungs, fallopian tubes, and ventricular systems. Their synchronised movement generate a directional flow, which are involved in establishment of right-left symmetry in human body, the removal of debris from respiratory system, and transport of solutes in kidney [109]. These microstructures play a crucial role in the CSF system, from development to its function. In recent years, the neurogenesis (i.e. birth of new neuroependymal cells (lining lateral, third, nes) in adult human brain become uncovered [152] . Swamoto et al. suggests that motile cilia form a concentration gradient that are essential for the migration of the new born neurones [124], which promote organ recovery and self-repair in brain. A recent published study proposed a direct link between alcohol consumption and cilia dysfunction [2]. Defects in these structures are correlated with disruption in ventricular development, impairment in CSF mixing , and enlargement of the ventricular systems [109].

In general, understanding and confirming the dynamics of CSF flow is crucial and can provide many benefits in explaining the underlie cause of various pathological conditions that lead to non-reversible neurological disorders (e.g. hydrocephalus) [129], in providing alternative and/or more effective treatments (e.g. shunt improvement)[85], and paves the way towards proposing procedure to possibly cure and rehabilitation of various brain related disorders by taking advantages of solute and drug transport (e.g. via drug delivery) [141]. Recall that, solutes and drugs can enter the CSF system either through

choroid plexus or ependymal cells (i.e. ventricular walls) and can be transported by CSF to various parts of the brain, if the dynamics of the transports are known. In addition, the flow generated by the ciliary beatings are postulated to transport solutes, remove waste products, and modify the depth of unstirred layers at ventricular walls [124, 107]. Computational studies (i.e. CFD) are also beneficial in modelling the CSF flow; they provide a tool for investigating the flow pattern in health, diseased, and treated states without the need for *vivo* studies (e.g. human trials). However, so far, the set-up of computational studies has been based on the inconsistent clinical and experimental conjectures, which led to contradictory results. For example, some investigators accounted for CP expansion as the flow driving force, whereas others take ventricular (or only 3V) expansion (refer to Table 1). Another factor affecting the results of computational studies is the misinterpretation and over simplification of applied conditions (i.e. boundary and/or initial). For instance, in most studies, choroid plexus is responsible for CSF production (refer to Table 1), however among all of the studies, except one to the best of our knowledge [53], there is no assigned area to choroid plexus in the computational domain; the CSF production takes place everywhere in the system by accounting for a source term in continuity equation [95, 143]. Another crude simplification is in modelling the CSF production: the bulk CSF flow production is represented by combining average CSF production (i.e. 0.5 ml/min) and a sinusoidal function [22, 95] or alternatively by normalising the bulk flow with arterial blood flow signal [143, 83].

Another significance of utilising the computational studies is its ability to acquire information that is impossible to provide by clinical and experimental studies (e.g. due to low resolution). One example is quantifying the wall effects in such complicated system. Numerical investigations could fulfil this need by adopting appropriate assumptions, boundary conditions, and non-simplified geometries. However, among all the conducted computational studies, to the best of our knowledge, there is only one study in the ventricular system that characterised the wall shear stress in the system [131] (more details of this study are provided in the Table 1). In this study, Siyahhan et al. reports the time averaged wall shear stress value for two small regions in the ventricular system. However, this coefficient is a function of space and time and it should receive more attention in such complex geometry and system. This physical quantity may provide important

Reference	Computational Domain	Boundary Conditions	Significant Flow Features
Kurtcuglu 2007 [75]	3D, 3V, AQ	Inlet: Entrance of 3V walls: Rigid outlet: Exit of AQ	Laminar flow with three features in 3V: Jet flow, two recirculation zones. $V_{maxAQ} = 167 \text{ mm/s}$
Howden 2008 [53]	3D, LV, FOM, 3V, AQ, 4V	Inlet: CP walls: Rigid outlet: 4V	Creeping Flow in LV. Laminar flow in the rest. $V_{maxAQ} = 11.38 \text{ mm/s}$
Linninger 2009 [83]	2D, LV, FOM,3V, AQ, 4V, BT, CSAS,SpSAS	Inlet: CP in LV walls: Partially deformable outlet: CSAS	Reversed flow in all system in early systole and diastole. $V_{maxAQ} = 5 \text{ mm/s}$
Sweetman 2011 [143]	3D, LV, FOM, 3V, AQ, 4V, BT, CSAS	Inlet: CP walls: Partially deformable with predefined function outlet: CSAS	Reversed flow in all system at early systole and diastole. $V_{maxAQ} = 25 \text{ mm/s}$
Maoumi 2013 [95]	2D, LV, FOM,3V, AQ, 4V, BT	Inlet: CP walls: Rigid outlet: Exit of 4V Inlet: CP walls: Deformable outlet: Exit of 4V	Similar velocity profiles in both simulations. Reversed flow in diastole when deformable walls. Rigid wall: $V_{maxAQ} = 11 \text{ mm/s}$ Deformable wall: $V_{maxAQ} = 8 \text{ mm/s}$.
Siyahhan 2014 [131]	3D, LV, FOM, 3V, AQ, 4V,	Inlet: CP walls: Rigid outlet: Exit of 4V	Existence of orthogonal and parallel streamlines to the walls of LV at different times. Recirculation zones at some instants in 3V. $V_{maxAQ} = 167 \text{ mm/s}$

Table 1: Summarised investigations from CFD simulations. LV:Lateral ventricles, FOM: foramen of Monro, 3V: third ventricle, 4V:fourth ventricle, AQ: aqueduct, CSAS:cerebral subarachnoid space, SpSAS: spinal subarachnoid space, BT: brain tissue.

information about solute mixing and solute transport near the walls. Alteration in CSF flow dynamics may further affect the shear stress: increased shear stress may be associated with cell shedding from ventricular walls that have been reported in existence of hydrocephalus, and decreased shear stress may lead to deposition of solutes and debris in the system [161].

In the last decade, there has been a growing body of numerical, clinical, and experimental studies to investigate the movement of cilia and its effect on the surrounding fluids in various parts of body. However, not many investigations (i.e. only one [131]) have been done to study the dynamic effects of ciliary beating on the CSF flow on macro and micro scales flows. In the conducted study, two small subdomains of lateral ventricle were taken as the computational domain, on which cilia were modelled. They reported that motile cilia dominate the dynamics of CSF flow near the wall [131]. However, in this study the

conditions were physiologically inappropriate: CSF production occurred everywhere in the system, non-pulsatile (i.e. river like) flow with rigid ventricular walls.

Considering all above arguments and discussions, we raise questions: Is it appropriate to discuss about CSF flow pulsatility as an event that occur everywhere in such a complicated domain? or the system must be examined locally? Also, according to a study done by Lee et al. the size of lateral ventricular volume varies by 10-20% during each cardiac cycle [81]. Does the ependymal cell layer displacement cause CSF flow circulation or the forces caused by CSF circulation is responsible for ventricular wall movement? Some researchers believe that the CSF pulsation in 3rd ventricle is more significant than in Lateral ventricles [39]. Is this observation related to smaller volume of the 3V compared to the LVs? What does such displacement of the ventricular wall imply on the flow in LVs? Does cilia beating affect the flow at vicinity of the wall or its affect are felt by the macroscale flow as well? What is the mechanism for solute transport in the CSF domain? In addition, some studies suggest that there are areas in the ventricular system with no motion and the CSF is nearly stagnant [65]. How do the solutes travel in those areas? How significant is contribution of the cilia in mixing of the CSF flow? How significant is contribution of the cilia in transport of solutes at various locations in the CSF domain (i.e. at low-momentum area (inferior horns) vs high-momentum area (aqueduct))?

Given the above arguments, we extend our investigation to possibly fulfil some of the aforementioned knowledge gaps. However, provided the time limit, we conduct a study with the objective of,

- Characterising the CSF flow dynamics in a real geometry (i.e. cerebral ventricles); analysing the flow pattern, pressure gradients, wall shear stresses and fluid velocity using computational fluid dynamics.

3 Development of a Comprehensive Mathematical Model for the Choroid Plexus

In the preceding chapter, we highlighted the need for a more comprehensive exploration of the choroid plexus (CP). Consequently, this chapter lays the groundwork for developing the first all-encompassing mathematical model that elucidates the mechanics of the CP, including its role in the production of cerebrospinal fluid (CSF). This organ is composed of three primary layers of blood vessels, connective tissues, and epithelial cells, all of which exist in various parts of the human body (e.g. kidney, eye, pancreas). Hence, in this chapter, we derive a general set of equations for each of these organs individually, which can be employed to model similar organs elsewhere in the body. Nonetheless, as our aim is to model the choroid plexus, the explanations will ultimately tilt towards fulfilling the objective of the current study. It is worth noting that organs such as blood vessels and epithelial cells have previously been mathematically modelled for different purposes. However, they have never been modelled for the choroid plexus, nor have they been modelled as a single system.

The structure of this chapter is outlined as follows: initially, the micro-anatomy of the choroid plexus is discussed, outlining the key compartments in the system. Subsequently, each compartment is explored in dedicated sub-sections, which describe their morphology and physiology, including their interface. This is followed by a mathematical derivation for each medium. Upon completion of this chapter, a general form of equation for each medium will have been established. In the next chapter, these equations will be finalised and combined to represent the choroid plexus as a complete system.

3.1 Microanatomy of choroid plexus

The choroid plexus (CP) is a vascular network arising as extensions of the ependymal cells lining the cerebral ventricles. At first glance, in a macro-scale view, the tissue appears as a complex shaped organ with a dense papillary structure (Figure 11-A). However, in micro-scale, a magnified top view of CP surface reveals sheet like structures residing next to each other in a longitudinal folds, i.e. parallel form (Figure 11-B). A scanning

electron micrograph of the outer surface of CP indicates homogenous and bumpy structures, called epithelial cells. These cells are covered by cilia (primary and motile) and microvilli (Figure 11-C). On the other hand, a cross sectional cut of the organ shows vascularised strands of CPs (Figure 11-D). A micrograph of the strands includes a clear view on two units of choroid plexus, with their capillaries, embedded in connective tissue, and epithelial cells (Figure 11-E).

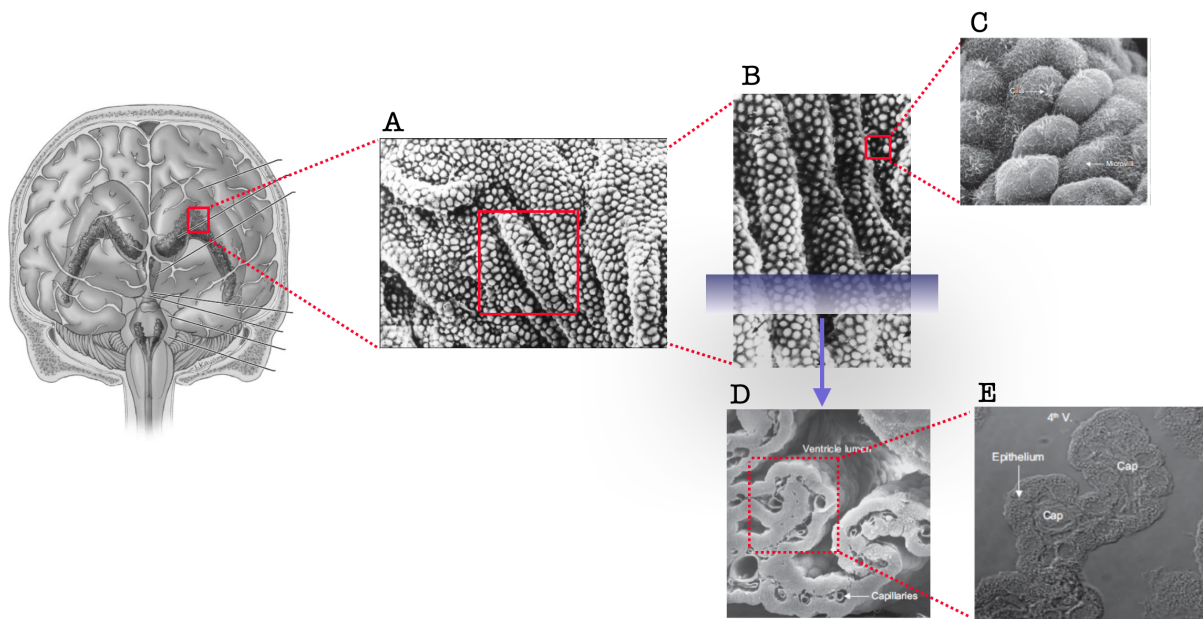


Figure 11: Morphology of choroid plexus reveals a complex shaped structure residing next to each in parallel form (A-B). A close view from the top shows the epithelial cells covering the entire CP (C). A cross sectional cut through the CP shows a highly vascularised structure (D). Two strands of CP, each contains one capillary embedded in connective tissues and a layer of cuboidal epithelial cells. Pictures are adopted from different sources [122, 28, 146]

To provide a more clear view, Figure 12 shows a sketch for a functional unit of choroid plexus (CP) that consists of capillaries (Cap) embedded within a layer of connective tissue (i.e. Stroma), and a single layer of epithelial cell.

In general, there exist two types of capillaries in brain: continuous and fenestrated. These capillaries are distinguished from one another by the characteristic structure difference in their cells lining up the capillary vessels, called endothelial cells (refer to Figure 13 for different types of capillary vessels). In particular, most capillaries in brain are the continuous type; their endothelial cells are non-fenestrated and small solutes can only cross

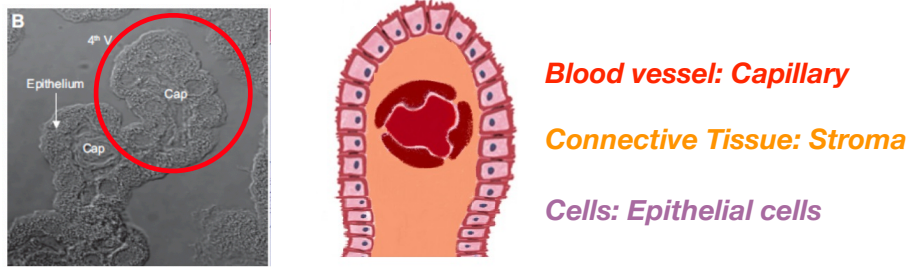


Figure 12: Micro-anatomy of a single strand of the choroid plexus.

them through tight junctions or intercellular clefts, i.e. the movement is highly restricted. These capillaries compose the blood-brain barrier, i.e. BBB. However, choroid plexus is the only place in the brain that has fenestrated capillaries: the endothelial cells in CP contain pores that are highly permeable to fluids and solutes into the surrounding tissue (Stroma). This tissue itself is separated from the brain ventricles by a continuous layer of epithelial cells.

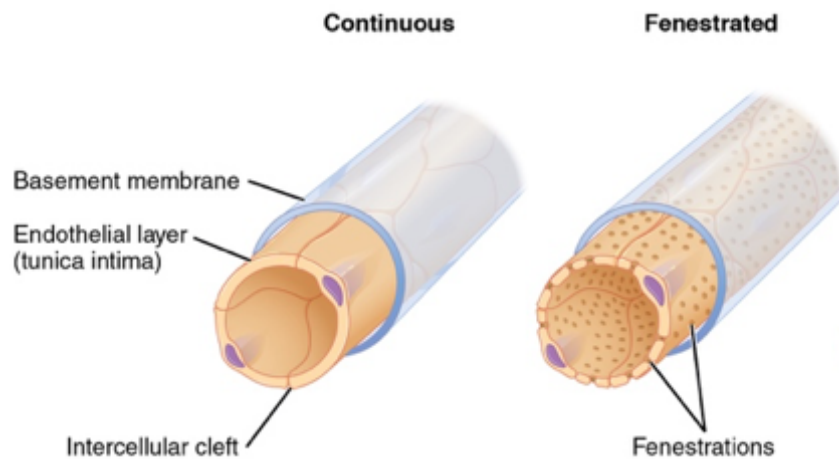


Figure 13: Scheme of different types of capillaries throughout the body. Continuous capillaries have intact endothelial cells and basement membranes. Fenestrated capillaries have continuous basement membrane, however there are perforations in their endothelial cells that allows for transfer of water and molecules (picture taken from [1]).

Epithelial cells, by definition, are type of cells that connect the surface of many organs such as kidney proximal tubule, sweat gland duct, gall bladder and Choroid plexus. A typical feature of epithelial cells (Figure 14) reveals that they all have a brush border interface with lumen, called apical membrane (APM), and an interface with blood plasma called basolateral (basal-lateral) membrane. The basolateral membrane (BLM) itself is

composed of two sides: the side opposing the apical membrane, called basal membrane, and a lateral membrane facing another epithelial cell. These epithelial cells are sealed together by tight junctions near the apical surface making a narrow space between the two cells, called lateral intercellular space (LIS).

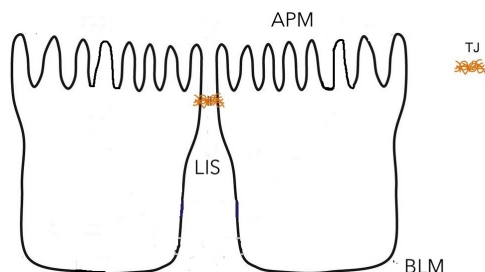


Figure 14: Scheme of two epithelial cells that are linked together by tight junction near the luminal surface, taken from [67].

As discussed in chapter 1, choroid plexus is proposed as one of the main sites for CSF production. A general belief is that the capillary walls and the Stroma do not impose any restriction to the transport of water or solute across the CP [14, 64, 28]. However, we challenge this perception due to the morphology of the compartments and model all the compartments. Therefore in our model, the CSF production takes place at three stages: first, blood passing through the choroid plexus capillaries partially cross the walls (endothelial cells) and make blood ultrafiltrate (plasma) and reach the Stroma. Then, plasma travels through the connective tissues in Stroma to reach the epithelial cells. Finally the fluid that reached the epithelial cells is transported by different mechanisms, and enter the ventricular space.

Note that the fluid (i.e. blood, CSF) is composed of water and solutes. To this end, there are seven main media composing a unit choroid plexus, i.e. Cap, EC, St, BLM, APM, and TJ. In the following sections, each medium with their mechanisms accountable for water and solute transports are explained in detail, below.

3.2 Capillary vessel

Capillaries are the tiniest branches of blood vessels that facilitate the exchange of solutes and water between the circulatory system and the surrounding space (i.e. interstitium). The capillary walls in the CP are composed of three layers (15): glycocalyx layer, endothelial cells and the basement membrane. The glycocalyx is a matrix that covers the inner side of the vessels and covered by the endothelial cells (EC); a collection of cells, in which each cell is connected to another either tightly (i.e. tight junctions) or do not seal properly and leave a gap between them (i.e. intercellular clefts). Note that the glycocalyx layer covers the pores (i.e. diaphragmed fenestrea), but not the intercellular clefts. In addition, these cells are covered from the outer side via basement membrane that do not act as a barrier to small solutes and water transport [68]. .

In this study, we model the capillary wall as a one medium and do not model the layers

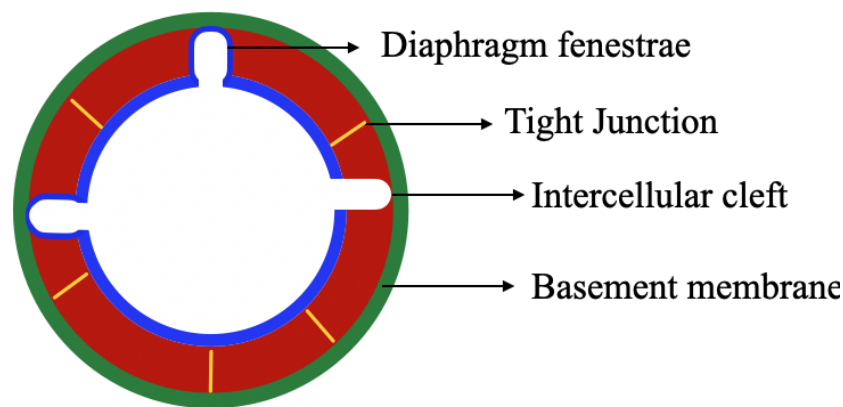


Figure 15: Schematic picture depicting fenestrated capillary cross section. Choroid plexus capillaries are composed of three layers: glycocalyx layer, endothelial cells with fenestrations, basement membrane. The endothelial cells may join to one another tightly tight junctions, or do not join, leaving a gap (i.e. intercellular clefts). The diaphragm covers the inner side of the pores, but not the clefts.

separately. However, we indirectly account for the limitation that each layer may impose to the transportation of solute when defining the parameters. This will be further elaborated in Chapter 3.

3.2.1 Mathematical modelling of capillary

In this section, the mathematical model for the transport of water and solutes flowing down the capillary and across endothelial cells are introduced. Since endothelial cells compose elastic walls, the model also accounts for the elastic nature of the capillary wall.

Mass conservation of water and solutes

The first set of equations that govern the flow inside capillary is the mass conservation law for the fluid (i.e. water) and each individual solute (e.g. sodium, potassium, and etc). In general, this balance ensures that the total mass for each material in a control volume is conserved. Since one unit of capillary resembles a cylinder, the equations will be formulated in the cylindrical coordinate system. Here, we introduce the mass conservation in an integral form that explains the rate of the volume change of capillary is balanced by the fluid entering and exiting the compartment. This conservation for water in capillary (Cap) can be stated as,

$$\frac{dV}{dt} = Q_{in} - Q_{out}, \quad (1)$$

V , Q_{in} , and Q_{out} are the volume, the influx and the outflux, respectively. Assuming that the volume change occurs by a variation in the cross-sectional area "A" of the cylinder (i.e. constant length "l"), the above equation can be expressed as,

$$l \frac{dA}{dt} = Q_{in} - Q_{out}. \quad (2)$$

Subsequently, the mass conservation for each solute that exist in the blood (e.g. potassium) in a compartment can be written as,

$$\frac{d}{dt}(VC_i) = Q_{in}C_{i,in} - Q_{out}C_{i,out}. \quad (3)$$

Where C_i is the conservation of the i^{th} solute. This balance states that in a control volume, the total mass of solutes is conserved over time and it can be rearranged as,

$$l \frac{d}{dt}(AC_i) = Q_{in}C_{i,in} - Q_{out}C_{i,out}. \quad (4)$$

Momentum conservation

An additional equation that governs the fluid flow inside the capillary is the momentum conservation balance, which states that the forces acting on a control volume must be balanced with the momentum change inside the control volume (i.e. capillary). This balance in capillary for incompressible and Newtonian fluids can be written as,

$$\rho \left(\frac{\partial \vec{u}}{\partial t} + (\vec{u} \cdot \nabla) \vec{u} \right) = \nabla \cdot \bar{\sigma} + \rho \vec{f}. \quad (5)$$

where ρ is the density, $\bar{\sigma}$ is the stress tensor, \vec{u} and \vec{f} are the velocity and body force vectors, respectively. Since the flow inside a capillary (i.e. cylinder) resembles an axisymmetric flow, we can assume there is no tangential velocity (i.e. $u_\phi = 0$) and the remaining quantities are independent of $\phi = 0$. Therefore, Equation 5 in the absence of any external and body force can be rewritten for the two remaining velocity components as,

$$\frac{\partial u_r}{\partial t} + u_r \frac{\partial u_r}{\partial r} + u_z \frac{\partial u_r}{\partial z} = -\frac{1}{\rho} \frac{\partial P}{\partial r} + \frac{\mu}{\rho} \left[-\frac{u_r}{r^2} + \frac{1}{r} \frac{\partial}{\partial r} \left(r \frac{\partial u_r}{\partial r} \right) + \frac{\partial^2 u_r}{\partial z^2} \right], \quad (6)$$

$$\frac{\partial u_z}{\partial t} + u_r \frac{\partial u_z}{\partial r} + u_z \frac{\partial u_z}{\partial z} = -\frac{1}{\rho} \frac{\partial P}{\partial z} + \frac{\mu}{\rho} \left[\frac{1}{r} \frac{\partial}{\partial r} \left(r \frac{\partial u_z}{\partial r} \right) + \frac{\partial^2 u_z}{\partial z^2} \right]. \quad (7)$$

Assuming steady flow (i.e. $\frac{\partial}{\partial t} = 0$, flow does not change in time), no velocity in the radial direction (i.e. $u_r = 0$), and the fully developed flow in the stream-wise direction (i.e. $\frac{\partial u_z}{\partial z} = 0$), Equations 6 and 7 are reduced to,

$$\frac{\partial p}{\partial r} = 0, \quad (8)$$

$$-\frac{1}{\rho} \frac{\partial P}{\partial z} + \frac{\mu}{\rho} \left[\frac{1}{r} \frac{\partial}{\partial r} \left(r \frac{\partial u_z}{\partial r} \right) \right] = 0. \quad (9)$$

Since the flow in capillary is pulsatile, one might question the steady flow assumption. This assumption has been examined and results are shown in Appendix A. In addition, the two equations above demonstrate that the pressure is only a function of axial coordinate z , and Equation 9 can be presented in ordinary differential equation form and rearranged as,

$$\frac{1}{r} \frac{d}{dr} \left(r \frac{du_z}{dr} \right) = \frac{1}{\mu} \frac{dp}{dz}. \quad (10)$$

Since we are interested in the volume average of the equation, we take volume integral with respect to r and represent the solution as,

$$\frac{du_z}{dr} = \frac{r}{2\mu} \frac{dp}{dz} + \frac{A}{r}, \quad (11)$$

and

$$u_z = -\frac{1}{4\mu} r^2 \frac{dp}{dz} + A \ln(r) + B. \quad (12)$$

Where A and B are the constants and need to be evaluated. Since the velocity u_z must be finite at $r = 0$, then A must be zero. In addition, one common assumption used is the no slip velocity at the boundary (i.e. $u_z = 0$ @ $r = R$) which determines B ,

$$A = 0,$$

$$B = -\frac{1}{4\mu} R^2 \frac{dp}{dz}.$$

Substituting the constants back into the 12,

$$u_z = \frac{1}{4\mu} \frac{dp}{dz} (R^2 - r^2). \quad (13)$$

which is a representation of parabolic velocity profile for velocity. This final assumption (i.e. no slip velocity at the wall) has been examined and the results are discussed in Appendix A (i.e. Figures 46 and 47).

Since we are interested in the volumetric average velocity Q , we further integrate the

Equation 13 over the cross section of the cylinder as,

$$Q = \int_R^0 \frac{1}{4\pi} \frac{dp}{dz} (R^2 - r^2) 2\pi r dr,$$

$$\implies Q = \frac{\pi}{2\mu} \int_R^0 (rR^2 - r^3) dr = \frac{\pi}{2\mu} \frac{dp}{dz} \left(\frac{r^4}{4} - \frac{r^2 R^2}{2} \right) \Big|_0^R$$

Which yields an expression for momentum conservation law in a simplified form (i.e. Hagen Poiseuille) as,

$$\frac{dp}{dz} = \frac{8\pi\mu}{A^2} Q \quad (14)$$

Or

$$\Delta p = \frac{8\pi\mu l}{A^2} Q \quad (15)$$

Note that $\Delta P = P_{in} - P_{out}$ is the pressure drop from the inlet to the outlet of the cylinder, and $\frac{8\pi\mu l}{A^2}$ is an approximate resistance (μ is the dynamic viscosity of the fluid).

3.2.2 Mathematical modelling of endothelial cells

So far, equations governing the flow inside the capillary as integral forms of conservation laws (i.e. mass and momentum) have been discussed. In the following, we will discuss the mechanisms and the equations that govern the flow of water and solutes across the fenestrated capillary walls (i.e. endothelial cells (EC)).

Solute transport

Exchange of solutes across fenestrated endothelial cells are mainly facilitated via pores, intercellular clefts, and tight junctions via two mechanisms: diffusion and advection [68, 79]. The latter involves fast bi-directional movement of substances over atomic length scales (i.e. very short distances) in random manner that appears as a very slow mechanism over large length scales of the biological systems under this study. This process in macroscopic scales is initiated with a concentration gradient between the capillary and the interstitial space (i.e. across the endothelial cell). The rate of a specific solute diffusion depends on its molecular weight (the heavier the solute, the slower the diffusion rate) and the permeability of the endothelial membrane to that solute. The net rate of diffusion (J_D)

across an endothelial cell is given by Fick's law (Equation 16), which depends on diffusion constant (D), the surface area of membrane (B), the concentration difference across the membrane (e.g. plasma vs interstitial fluid), and the membrane thickness (Δx).

$$J_D = DB\Delta C_i \quad (16)$$

Advection of the solutes through the paracellular route, is a passive transport of solutes along with the host fluid (solvent) and is the dominant process if the momentum of the fluid is significant (i.e. Peclet number, the ratio between advective and diffusive transport rates, larger than unity is an indication that the transport is mainly due advection and the diffusion may be neglected). In this case, the exchange of solutes is determined mainly by the dynamics of the fluid flow. If the flow is from capillary into the interstitial space the solute transport is called filtration, while for the flow in the opposite direction the term absorption is used. In addition, the advection of solutes (J_A) through endothelial cells membrane, in the case where there is no concentration gradient, is determined by solute concentration (C_i) and net volume flow of water (Q) carrying the solutes, as

$$J_A = C_i(1 - \sigma_i)Q. \quad (17)$$

σ_i is the solute reflection coefficient, which is defined as the ratio between osmotic pressure difference produced by the solute across a membrane and the osmotic pressure difference that would exist if the solute were totally impermeable. Therefore σ_i can take any value between zero and one, where $\sigma_i = 1$ corresponds to all the solutes being reflected and $\sigma_i = 0$ corresponds to situations where solute could freely pass through the membrane [52].

Since, transport of solutes via diffusion and advection mechanisms across membranes occur in parallel, the total solute flux (J) across endothelial cells is,

$$J = J_D + J_A,$$

or

$$J = DB\Delta C_i + C_i(1 - \sigma_i)Q. \quad (18)$$

Water transport

Transport of water across fenestrated endothelial cells is a passive process utilised mainly via paracellular transport. This fluid flow (Q) is derived by the hydrodynamic (ΔP) as well as the osmotic pressure gradients ($\Delta\pi$) across the endothelial cell layer. The hydrodynamic pressure gradient, on one hand, imposes a body force on the water particles to explicitly move in the opposite direction of the pressure gradient, while the osmotic pressure implicitly induce water particles to move in the direction of the concentration gradient to reach iso-osmolarity. This water transport, which also is known as Starling law is expressed by,

$$Q = Lp[\Delta P - \sigma_i \Delta\pi] \quad (19)$$

Lp is the hydraulic conductivity of the membrane, σ_i is the reflection coefficient and π is defined as $\pi = RTC_i$ (R : Gas constant, T : temperature). Therefore, the Starling law can be rearranged as

$$Q = Lp[\Delta P - RT\sigma_i(\Delta C_i)]. \quad (20)$$

Elasticity

So far, we discussed the mechanisms by which solutes and water travel through and across the medium. Now we turn our attention to another characteristic of the membrane: elasticity. Biological membranes (i.e. endothelial cells) have very thin walls and facilitates the membrane deformability when subjected to external forces and return to their original state in the absence of any applied force (i.e. equilibrium state) [11]. The motion of such biological membrane is governed by the momentum balance as,

$$\rho\left(\frac{\partial \vec{u}}{\partial t} + (\vec{u} \cdot \nabla)\vec{u}\right) = \nabla \cdot \bar{\bar{T}} + \rho \vec{f} + \vec{\pi}, \quad (21)$$

where $\rho, \vec{u}, \bar{\bar{T}}, \vec{f}$, and $\vec{\pi}$ denote the density, velocity vector, tension tensor, body force, and the external load on the membrane. Since the inertia forces are negligible (i.e. low Reynold number) and assuming no body force on the membrane; the membrane motion is rearranged as,

$$\nabla \cdot \bar{\bar{T}} + \vec{\pi} = 0. \quad (22)$$

Furthermore, the endothelial cells can be represented as a thin walled cylinder with displacements purely in radial direction (i.e. $(T_{rr}, 0, 0)$ and $(\pi_{rr}, 0, 0)$). Subsequently, the first term on the left-hand side can be represented as,

$$\nabla \cdot \bar{\bar{T}} = \left[\frac{\partial T_{rr}}{\partial r} + \frac{1}{r} \frac{\partial T_{\phi r}}{\partial \phi} + \frac{\partial T_{zr}}{\partial z} + \frac{1}{r} (T_{rr} - T_{\phi\phi}, 0, 0) \right]. \quad (23)$$

In addition, the stretches happen in the angular coordinate, i.e. ϕ direction. Hence, the equation reduces to,

$$\nabla \cdot \bar{\bar{T}} = -\frac{1}{r} T_{\phi\phi} \quad (24)$$

These terms can be further approximated by Hooks law, which provides a linear relationship between the membrane stresses and the elastic deformation as [116],

$$T_{\phi\phi} = \frac{G}{1-\nu} \left(\lambda_{\phi}^2 - 1 + \nu \left[\lambda_z^2 - 1 \right] \right), \quad (25)$$

where G is the shear modulus constant, ν is the poisson ratio, and λ , are the expansion ratios. Given the assumption of no stretch in z-direction, the term $\lambda_z = 0$. In addition $\lambda_{\phi} = \frac{\phi}{\phi_o}$. The subscript o defines the variables at the initial state of the membrane. ϕ can be estimated in terms of radius r (i.e. conservation of area and perimeter) as,

$$\phi_o = 2\pi r_o, \phi = 2\pi r,$$

$$\frac{r_o}{r} = \frac{\phi_o}{\phi}.$$

Considering the aforementioned descriptions, the equation 25 can be rewritten as,

$$\nabla \cdot \bar{\bar{T}} = -\left(\frac{1}{r}\right) \left(\frac{G}{1-\nu}\right) \left(\frac{r^2}{r_o^2} - 1 - \nu\right) \quad (26)$$

Furthermore, the external load on the membrane (i.e. $\vec{\pi}$ in Equation 22) arises from the normal stresses exerted to the membrane as,

$$\vec{\pi} = (\bar{\bar{\sigma}}_{ex} - \bar{\bar{\sigma}}_{in}) \cdot \vec{n}. \quad (27)$$

Where $\bar{\sigma}$ is the stress tensor, \vec{n} is the outward unit normal vector, and the subscripts *ex* and *in* refer to the external and internal sides of the membrane. Therefore, this equation for the capillary as the internal environment

$$\begin{aligned}\bar{\sigma}_{Cap} \cdot \vec{n} &= (\sigma_{Cap} \cdot n_r, 0, 0) \\ &= \left(\frac{P_{Cap}}{\theta}, 0, 0 \right),\end{aligned}\tag{28}$$

where θ and P are the thickness and the pressure inserted to the membrane, respectively. Therefore, the equation governing the elasticity of capillary as an isolated compartment with no external load applied to can be written as,

$$\left(-\left(\frac{1}{r}\right)\left(\frac{G}{1-\nu}\right)\left(\frac{r^2}{r_o^2} - 1 - \nu\right) - \frac{P}{\theta} \right)_{EC} = 0.\tag{29}$$

3.3 Connective tissue

These tissues, in general, connect organs together and are composed of fibres, ground substance and cells. They are categorised into two types of dense and loose connective tissues, which are distinguished from one another by the ratio of ground substance to fibrous tissue. i.e. loose connective tissue has much more ground substance and a relative lack of fibrous tissue, while the reverse is true for dense connective tissue. The biomechanical behaviour of dense connective tissues (e.g. tendons & ligaments, cartilage, bone, etc) have been extensively studied, however very little is known about the characteristic and behaviour of loose connective tissues. These forms a continuous body wide network including subcutaneous and interstitial connective tissues surrounding all muscles, organs, and blood vessels [57].

Although transport across this tissue, to the best of our knowledge, has not been mathematically modelled, its mechanical features as a poroelastic medium resembles the brain parenchyma. This tissue is composed of two phases, a solid matrix and an interconnected fluid, which is saturated in pores. In order to develop an appropriate transport model of the fluid through the connective tissues (e.g. Stroma), studies on the flow through the brain parenchyma are needed to be reviewed.

Literature is divided in two different approaches when dealing with fluid flow in the brain parenchyma. A simple approach is to adopt a mechanical balance for the solid matrix displacement, which is not coupled with the fluid flow. In these approaches the interaction between the solid and the fluid is modelled by an immersed boundary method. An example of such studies is the CSF flow simulation in the ventricles when the authors considered a deformable interface in the location of the choroid plexus. The displacement is imposed by a simple mechanical function [42, 143].

The alternative and more accurate calculations belong to coupled systems of equations in Eulerian mesh arrangement that account for mass and momentum conservation laws in both solid and fluid phases in addition to an elastic law for the solid displacement (usually Hook's law [47, 106]).

In this stud, the latter approach is examined and the derivation of the governing equations for the fluid flow in the connective tissue is provided. The formulation is similar to

the mixed-phase approach [10, 100], considering the fact that the stroma in the choroid plexus can be considered a thin poroelastic layer surrounding the capillaries (i.e. the thickness of the layer is considerably smaller than the circumference of the layer).

3.3.1 Mathematical modelling of connective tissues

Mass conservation of water within poroelastic tissue

The conservation law of a fluid mass in a poroelastic medium demands that

$$\frac{\partial(\varphi\rho_f)}{\partial t} + \nabla \cdot (\varphi\rho_f\vec{u}_f) = 0, \quad (30)$$

where φ is the porosity, ρ_f is the fluid density, and \vec{u}_f is the velocity of the fluid phase. By the chain rule the first term expands as

$$\varphi\frac{\partial\rho_f}{\partial t} + \rho_f\frac{\partial\varphi}{\partial t} + \nabla \cdot (\varphi\rho_f\vec{u}_f) = 0. \quad (31)$$

As a general rule to approach mass conservation laws for fluid and solid phases in a poroelastic medium [10, 100], here they are considered compressible. The rate of change of density, $\frac{\partial\rho_f}{\partial t}$, of a constant mass material can be approximated as

$$\begin{aligned} \frac{\partial\rho_f}{\partial t} &= \frac{\Delta\rho_f}{\Delta t} = \frac{\rho_{f_2} - \rho_{f_1}}{\Delta t} \\ &= \frac{m_f}{\Delta t} \left(\frac{1}{V_{f_2}} - \frac{1}{V_{f_1}} \right), \end{aligned} \quad (32)$$

where subscripts 1 and 2 represent the values at t_1 and t_2 . This equation becomes

$$\frac{\partial\rho_f}{\partial t} = \frac{m_f}{\Delta t} \left(\frac{-\Delta V_f}{V_{f_2}V_{f_1}} \right) \quad (33)$$

Using $\rho_{f_2} = \frac{m_f}{V_{f_2}}$, the above equation becomes,

$$\frac{\partial\rho_f}{\partial t} = \frac{\rho_{f_2}}{\Delta t} \left(-\frac{\Delta V_f}{V_{f_1}} \right) \quad (34)$$

The volume fractional volume change $\frac{\Delta V_f}{V_{f_1}}$ can be estimated as $\frac{\Delta V_f}{V_{f_1}} = -\beta\Delta p$, where β and

P are the fluid compressibility coefficient and pressure, respectively. Substituting for the volume change in Equation 34, the rate of change of density can be written as

$$\frac{\partial \rho_f}{\partial t} \simeq \rho_f \beta \frac{\partial P}{\partial t} \quad (35)$$

The fluid mass conservation law (Equation 35) is therefore represented as,

$$\varphi \rho_f \beta \frac{\partial P}{\partial t} + \rho_f \frac{\partial \varphi}{\partial t} + \nabla \cdot (\varphi \rho_f \vec{u}_f) = 0. \quad (36)$$

Since the stroma is a thin layer, it is appropriate to assume that the properties of the layer are homogeneous in the angular and the axial directions, hence variables are only a function of radius. If the fluid density can be considered a weak function of space compared to time in such thin layer, it can be taken behind the space operators (e.g. divergence) as in the mass conservation equation

$$\varphi \rho_f \beta \frac{\partial P}{\partial t} + \rho_f \frac{\partial \varphi}{\partial t} + \rho_f \nabla \cdot (\varphi \vec{u}_f) = 0 \quad (37)$$

Adding and subtracting $\nabla \cdot (\varphi \vec{u}_s)$ from the above equation and dividing it by the density, the conservation law for the fluid phase becomes

$$\varphi \beta \frac{\partial P}{\partial t} + \frac{\partial \varphi}{\partial t} + \nabla \cdot (\varphi (\vec{u}_f - \vec{u}_s)) + \nabla \cdot (\varphi \vec{u}_s) = 0, \quad (38)$$

where (\vec{u}_s) is the solid rate of displacement. Note that the fourth term in the equation above is related to the displacement of the solid phase in the poroelastic medium, which is present in the conservation of mass for the solid phase

$$\frac{\partial((1 - \varphi)\rho_s)}{\partial t} + \nabla \cdot ((1 - \varphi)\rho_s \vec{u}_s) = 0. \quad (39)$$

In Equation 39, ρ_s is the density of the solid phase. The chain rule simplifies the first term as

$$-\rho_s \frac{\partial \varphi}{\partial t} + (1 - \varphi) \frac{\partial \rho_s}{\partial t} + \nabla \cdot \rho_s \vec{u}_s = \nabla \cdot (\varphi \rho_s \vec{u}_s). \quad (40)$$

Here again, the solid density can be assumed as a weak function of space compared to time and can be taken behind the space operators. Dividing all terms by the density provides

$$-\frac{\partial\varphi}{\partial t} + \frac{(1-\varphi)}{\rho_s} \frac{\partial\rho_s}{\partial t} + \nabla \cdot \vec{u}_s = \nabla \cdot (\varphi \vec{u}_s). \quad (41)$$

The rate of change of solid density $\frac{\partial\rho_s}{\partial t}$ can be estimated by making similar arguments as made for $\frac{\partial\rho_f}{\partial t}$ (i.e. Equations 32 to 35) as,

$$\frac{\partial\rho_s}{\partial t} = \frac{\Delta\rho_s}{\Delta t} = \frac{\rho_{s_2} - \rho_{s_1}}{\Delta t} = \frac{m_s}{\Delta t} \left(\frac{1}{V_{s_2}} - \frac{1}{V_{s_1}} \right), \quad (42)$$

where the subscripts correspond to times t_1 and t_2 . Further,

$$\frac{\partial\rho_s}{\partial t} = \frac{m_s}{\Delta t} \left(-\frac{\Delta V_s}{V_{s_2} V_{s_1}} \right) \quad (43)$$

Since, $\rho_{s_2} = \frac{m_s}{V_{s_2}}$,

$$\frac{\partial\rho_s}{\partial t} = \frac{\rho_{s_2}}{\Delta t} \left(-\frac{\Delta V_s}{V_{s_1}} \right). \quad (44)$$

The fractional volume change of solid $\frac{\Delta V_s}{V_{s_1}}$ can be estimated as

$$\frac{\Delta V_s}{V_{s_1}} = -\frac{((\alpha - 1)\Delta\epsilon + C_s\Delta P(\alpha - \varphi))}{1 - \varphi}, \quad (45)$$

Where C_s is the solid compressibility factor, α is the Biot-Willis coefficient (a value between 0 and 1) and ϵ is the volumetric strain (trace of the strain tensor). Substituting Equation 45 into 44, provides the rate of change of solid density as,

$$\frac{\partial\rho_s}{\partial t} \simeq \frac{\rho_s}{1 - \varphi} \left((\alpha - 1) \frac{\partial\epsilon}{\partial t} + C_s(\alpha - \varphi) \frac{\partial P}{\partial t} \right) \quad (46)$$

where $\frac{\Delta\epsilon}{\Delta t} = \nabla \cdot \vec{u}_s$, therefore,

$$\frac{\partial\rho_s}{\partial t} = \frac{\rho_s}{1 - \varphi} \left((\alpha - 1) \nabla \cdot \vec{u}_s + C_s(\alpha - \varphi) \frac{\partial P}{\partial t} \right). \quad (47)$$

Now, Equation 41 can be rearranged as

$$-\frac{\partial \varphi}{\partial t} + (\alpha - 1)\nabla \cdot \vec{u}_s + C_s(\alpha - \varphi)\frac{\partial P}{\partial t} + \nabla \cdot \vec{u}_s = \nabla \cdot (\varphi \vec{u}_s) \quad (48)$$

Substituting the left hand-side of Equation 48 for $\nabla \cdot (\varphi \vec{u}_s)$ in Equation 38 (i.e. last term) provides,

$$(\varphi\beta + C_s(\alpha - \varphi))\frac{\partial P}{\partial t} + \nabla \cdot (\varphi(\vec{u}_f - \vec{u}_s)) + (\alpha - 1)\nabla \cdot \vec{u}_s + \nabla \cdot \vec{u}_s = 0. \quad (49)$$

where the term $\varphi\beta + C_s(\alpha - \varphi)$ is called the storage coefficient S . Therefore, the equation reads as,

$$S\frac{\partial P}{\partial t} + \nabla \cdot (\varphi(\vec{u}_f - \vec{u}_s)) + \alpha\nabla \cdot \vec{u}_s = 0. \quad (50)$$

Since the velocity of the solid phase is equal to the derivative of the solid displacement vector \vec{d} in time, (i.e. $\vec{u}_s = \frac{\partial \vec{d}}{\partial t}$), the above equation becomes

$$S\frac{\partial P}{\partial t} + \nabla \cdot \left(\varphi \left(\vec{u}_f - \frac{\partial \vec{d}}{\partial t} \right) \right) + \alpha \nabla \cdot \frac{\partial \vec{d}}{\partial t} = 0. \quad (51)$$

This equation governs the mass conservation of both the fluid and the solid phases in a poroelastic material. The second term in Equation 51 (i.e. $\varphi \left(\vec{u}_f - \frac{\partial \vec{d}}{\partial t} \right)$) can be determined by the momentum conservation of the fluid phase,

$$\rho_f \left(\frac{\partial \vec{u}_f}{\partial t} + \vec{u}_f \nabla \cdot \vec{u}_f \right) = \nabla \cdot \bar{\bar{\sigma}}_f + \rho_f \vec{f} + \vec{\pi}_f, \quad (52)$$

where $\bar{\bar{\sigma}}_f$ is the stress tensor, $\rho_f \vec{f}$ is the body force in a unit volume (e.g. gravity), and $\vec{\pi}_f$ is the momentum supply. This balance is composed of the inertia forces on the left-hand side and the body as well as stress forces on the right-hand side. The ratio between these two terms in a poroelastic medium is usually very small [10], particularly in the stroma which is also a thin layer. Assuming no body forces acting on the medium, the momentum equation is reduced to

$$\nabla \cdot \bar{\bar{\sigma}}_f + \vec{\pi}_f = 0. \quad (53)$$

Assuming linear stress-strain relationship, Newtonian viscous fluid, and neglecting the viscous stress constants [10], we write

$$\bar{\sigma}_f = -\varphi PI, \quad (54)$$

Where P is the fluid pressure and I is the identity tensor. The momentum transfer is modelled by a linear relation as

$$\pi_f = \frac{-\varphi^2 \mu}{k} (\vec{u}_f - \vec{u}_s) - P \nabla(1 - \varphi), \quad (55)$$

Which is essentially Darcy law [10] and k is the permeability. Substituting Equation 54 and 55 into Equation 53 provides,

$$\nabla \cdot (-\varphi PI) - \frac{\varphi^2 \mu}{k} (\vec{u}_f - \vec{u}_s) - P \nabla(1 - \varphi) = 0, \quad (56)$$

Since $\nabla \cdot (-\varphi PI) = -\nabla(\varphi P)$, the above equation can be rearranged as,

$$\nabla(\varphi P) + \frac{\varphi^2 \mu}{k} (\vec{u}_f - \vec{u}_s) + P(\nabla(1 - \varphi)) + \nabla\varphi = 0. \quad (57)$$

Taking advantages of the chain rule, the first term can be expanded (i.e. $\nabla(\varphi P) = \varphi \nabla P + P \nabla \varphi$) and Equation 57 can be further stated as,

$$\varphi \nabla P + P \nabla \varphi + \frac{\varphi^2 \mu}{k} (\vec{u}_f - \vec{u}_s) + P \nabla(1 - \varphi) = 0, \quad (58)$$

or

$$\varphi \nabla P + \frac{\varphi^2 \mu}{k} (\vec{u}_f - \vec{u}_s) + P(\nabla(1 - \varphi) + \nabla\varphi) = 0. \quad (59)$$

since $\nabla(1) = 0$, the relationship can be further simplified as,

$$\varphi \nabla P + \frac{\varphi^2 \mu}{k} (\vec{u}_f - \vec{u}_s) = 0. \quad (60)$$

Therefore,

$$-\frac{k}{\mu} \nabla P = \varphi (\vec{u}_f - \vec{u}_s) \quad (61)$$

and Equation 51 can be expressed as,

$$S \frac{\partial P}{\partial t} + \nabla \cdot \left(-\frac{k}{\mu} \nabla P \right) + \alpha \nabla \cdot \left(\frac{\partial \vec{d}}{\partial t} \right) = 0. \quad (62)$$

Assuming permeability k to be independent of location, the equation can be simplified as,

$$S \frac{\partial P}{\partial t} - \frac{k}{\mu} \nabla^2 P + \alpha \nabla \cdot \left(\frac{\partial \vec{d}}{\partial t} \right) = 0. \quad (63)$$

This is the equation that governs the dynamics of the flow in the Stroma in the current study. This tissue, Stroma, can be represented by an annulus, with the inner radius r_i and the outer radius r_o corresponding to the Stroma at at the endothelial and basal membrane sides, respectively. Therefore, we write the aforementioned governing equation in the cylindrical coordinate system with the assumption that all dependent variables such as the pore fluid pressure and the solid displacement are only functions of the radial coordinate (i.e. axially symmetric and homogeneous along the axis). Equation 63 in the streamwise direction becomes

$$S \frac{dp}{dt} - \frac{k}{\mu} \left(\frac{1}{r} \frac{\partial}{\partial r} \left(r \frac{\partial p}{\partial r} \right) \right) + \alpha \left(\frac{1}{r} \frac{\partial}{\partial r} \left(r \frac{\partial d_r}{\partial t} \right) \right) = 0. \quad (64)$$

For simplicity from now on the subscript r is removed from the variables (e.g. $d = d_r$). Taking a volumetric average of the Equation 64 from the inner radius r_i (representing the capillary interface; endothelial cells) to the outer radius r_o (representing the ventricular interface; epithelial cells), each term becomes

- $\frac{1}{\pi r_o^2 - \pi r_i^2} \int_{r_i}^{r_o} S \frac{dp}{dt} 2\pi r dr = S \frac{d\langle p \rangle}{dt}$.
- $\frac{1}{\pi r_o^2 - \pi r_i^2} \int_{r_i}^{r_o} \frac{k}{\mu} \left(\frac{1}{r} \frac{\partial}{\partial r} \left(r \frac{\partial p}{\partial r} \right) \right) 2\pi r dr = \frac{2}{r_o^2 - r_i^2} \left(\frac{k}{\mu} \left[r_o \left(\frac{\partial p}{\partial r} \right)_{r_o} - r_i \left(\frac{\partial p}{\partial r} \right)_{r_i} \right] \right)$.
- $\frac{1}{\pi r_o^2 - \pi r_i^2} \int_{r_i}^{r_o} \alpha \left(\frac{1}{r} \frac{\partial}{\partial r} \left(r \frac{\partial d}{\partial t} \right) \right) 2\pi r dr = \frac{2\alpha}{r_o^2 - r_i^2} \left[r_o \left(\frac{\partial d}{\partial t} \right)_{r_o} - r_i \left(\frac{\partial d}{\partial t} \right)_{r_i} \right]$.

Therefore, the volumetric average of the Equation 64 becomes,

$$S \frac{d\langle p \rangle}{dt} - \frac{k}{\mu} \frac{2}{r_o^2 - r_i^2} \left[r_o \left(\frac{\partial p}{\partial r} \right)_{r_o} - r_i \left(\frac{\partial p}{\partial r} \right)_{r_i} \right] + \frac{2\alpha}{r_o^2 - r_i^2} \left[r_o \left(\frac{\partial d}{\partial t} \right)_{r_o} - r_i \left(\frac{\partial d}{\partial t} \right)_{r_i} \right] = 0. \quad (65)$$

In the equation above $\langle P \rangle$ denotes the volumetric average pore fluid pressure in the

stroma. This equation govern the volumetric average of the dynamics of the fluid-solid interaction in the poroelastic stroma in the current simplified model. Later, in a dedicated section to the holistic model of CSF production, the boundary conditions of these equations will be specified and linked to the neighbour compartments.

Momentum conservation

Another relation that will be useful in this study is the relationship between stress-strain in such poroelastic medium. According to the constitutive law [89, 100] the stress tensor in an isotropic and poroelastic medium is related to the strain tensor by,

$$\bar{\sigma} = 2G\bar{\epsilon} + \frac{3\nu}{1+\nu}\sigma I - PI \quad (66)$$

where G, ν, \vec{d}, I , and $\bar{\epsilon}$ are the shear modulus, Poisson's ratios, solid displacement vectors, identity matrix, and strain tensor, respectively. Where σ is the mean stress., (i.e. $\sigma = \frac{\sigma_{kk}}{3}$). The above equation in the radial direction of cylindrical coordinate system will be rearranged as,

$$\sigma_{rr} = 2G\epsilon_{rr} + \frac{3\nu}{1+\nu}\left(\frac{\sigma_{rr}}{3}\right) - P_r$$

or

$$\sigma_{rr} = (2G\epsilon_{rr} - P_r)(1 + \nu) \quad (67)$$

Note that $\sigma_{rr} = \frac{\partial d_r}{\partial r}$ and $G = \frac{E}{2(1+\nu)}$. Therefore,

$$\sigma_{rr} = E \frac{\partial d_r}{\partial r} - (1 + \nu)P_r \quad (68)$$

This relationship is utilised when the relationship between the stress and strain in Stroma is of interest.

3.4 Epithelial cells

Epithelial cells are aggregation of cells that cover different organs in the body e.g. pancreatic ductal epithelium, proximal tubule epithelium, retinal pigment epithelium, and choroid plexus epithelium [19, 35]. These cells are highly dynamic; a characteristic that they inherit from their viscoelastic properties. This property of the material exhibit a combination of elastic and viscous characteristic when undergo deformation. Purely elastic materials strain instantaneously when subjected to stress, whereas viscous material undergo a time-dependent strain.

The solute transport across these cells differ from the ones explained in previous section. Typically, there are two routes that molecules can take to cross epithelial cells: paracellular and transcellular routes. The former is the transport of substances by passing through the intercellular space between two adjacent cells, called tight junctions (TJ). A characteristic of this transport is that it is passive and depends solely on the local concentration gradients between two mediums [36]. In literature, there are three common models proposed for paracellular transport: mechano-diffusion model, electro-diffusion model, and the Claudin model (Figure 16). In the first model (top-left panel), water and solute transport are facilitated by active opening and closing behaviour of a series of compartments formed in the junction, to allow diffusion of water and small solutes but not large macromolecules. This implies that the flow becomes hypotonic (i.e. lower osmotic pressure) downstream of the junction. In the electro-diffusion model (top-right panel), the net negative electrical charge of the junctions attracts sodium (Na) ions into the gap between the cells which accompanied by a bulk water transport. The Claudin model (bottom panel) proposes that Claudin proteins in the junction co-transport ions and water across the cells. So far, 24 members of this protein family has been discovered [130] with various roles in transporting different molecules. For instance, Claudin-16 mediates transport of magnesium (Mg), while Claudin-2 facilitate water transport [28].

Transcellular mechanism, on the other hand, refers to transportation of solutes and water across the cells, which are facilitated via special proteins (i.e. channels and carriers) residing on biological membranes (apical and basal membranes). Primary difference between the channels and carriers is that they are simultaneously open to both sides, while

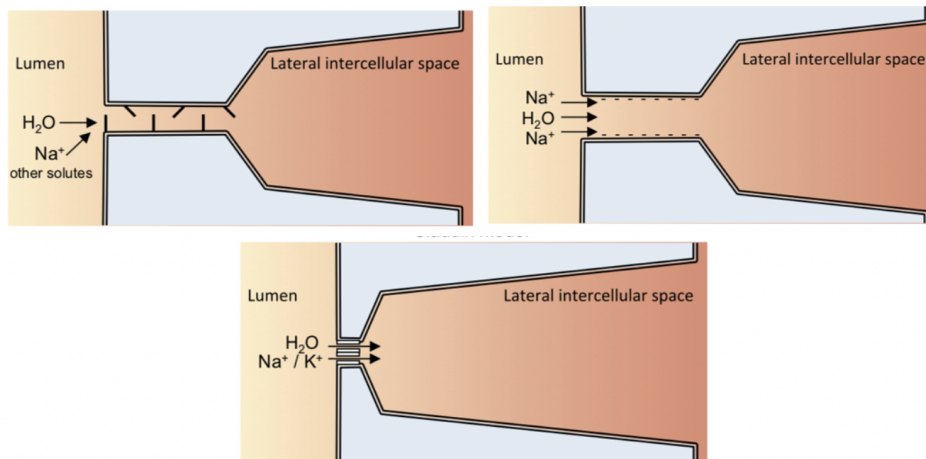


Figure 16: Proposed models for three different paracellular transport: (top-left) mechano-diffusion model, (top-right) electro-osmosis model, (bottom) and claudin model. Picture adapted from [28].

in carriers either the inner gate is open or the outer one (Figure 17).

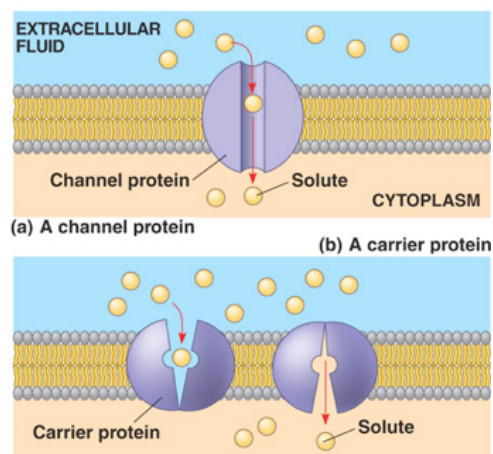


Figure 17: Membrane transport proteins. Top: Channel protein, Bottom: Carrier protein

In addition, channel proteins only allow movement of substances down their electrochemical gradients (i.e. passive transport), while the transport of substances via carrier proteins can be down or against their electrochemical gradients (i.e. passive or active transport, respectively). Movement of substances against their concentration and/or chemical gradient (active transport) require energy and can be divided into two types: primary active transport (PAT) and secondary active transport (SAT). Primary active transport acts a pump and uses a source of chemical energy that is driven from metabolism of cells to move substances against their gradients, whereas secondary active transport utilises

Route	Transporter Symbol	Molecule into the cell	Molecule out of the cell
Channel	Na	Na	Na
	Cl	Cl	Cl
	K	K	K
	AQP	water	water
Transporter	NBCe2		HCO,Na
	NKCC1	Cl,K,Na	
	KCC3		K,Cl
	KCC4		K,Cl
	AE2	Cl	HCO
	NBCn2	HCO,Na	Cl
	NHE	Na	H
Pump	Na-K-ATPase	K	Na

Table 2: Passage of substances via transcellular routes is facilitated by protein molecules such as channels, co-transporters, and pumps. Compounds- Na:sodium, Cl: chlorine, K:potassium, HCO:bicarbonate, H:hydrogen, AQP: aquaporin

the energy, stored from the electrochemical gradients that is resulted from primary active transport to, move substances. This form of active transport uses transporters that couples the movement of some ions down their electrochemical, while some others move against their gradient [32]. Furthermore, the transport of these molecules may be all in the same direction (i.e. all into a cell or out of a cell: symporters or cotransporters) or in opposite directions (i.e. some into a cell and some out of a cell: antiporters or counter transporters). A list of some transcelular transporter symbols and their corresponding ions are tabulated in Table 2.

So far, relevant mechanisms for transport of substances (i.e. solute and water) across typical physical barriers have been discussed. Note that, different epithelial cells have different types of transporters. However, since we aim to model choroid plexus epithelium, we included a subsection that specifically addresses the transport across these cells.

CPE secretion model

A typical CPE and its transporters are depicted in Figure 18. In general, among all the solutes existing in blood, sodium, chloride, bicarbonate and potassium (i.e. Na, Cl,

HCO₃, and K) are proposed to cross the epithelial cells. The model shows the transporters responsible for the movements of these solutes are AE2 and NCBE/NBCn2, and KCC3 on BLM and on the apical membrane NBCe2, KCC4, NKCC1, and Na-K-ATPase transporters as well as Cl and K channels).

Na, that has the highest concentration among the aforementioned solutes in blood (137 *mmol/L*), is believed to be the dominant driver of the CSF secretion. Eventual transport of Na across the CPE has a complication that despite the well-established transport across apical membrane, its transport mechanism across the BLM is not clearly understood. It is evident that the apical Na-K-ATPase pump exports most Na from cell into lumen, while it moves K from the lumen into the cell. Additionally, Na is also being transported into the lumen via NBCe2 co-transporter alongside HCO₃ (one Na with three HCO₃). There is an additional transport of Na across APM via NKCC1 co-transporter. In literature, there are controversies around the direction of this transporters. In general, studies suggest that NKCC on epithelial cells can transport in both directions [160]. However most studies suggest in a normal functioning CPE, the direction of solute transports is into the cells, i.e. the opposite of depicted in the figure below [28]. On the other hand, researchers have not confirmed the transport of Na via BLM. It has been suggested that the import of Na into cell is via Na-H and NBCn1 co-transporters. Note that the ambiguity is on the transporter of Na through the BLM and not the existence of transport itself. Last, the minimal paracellular transport of Na across the tight junctions is in the reverse direction from the CSF side into the blood side.

The second most important ion that is being transported across CPE is Cl (101 *mmol/L*) that enters the cell from the blood side via AE2 transporter residing on the BLM. It is believed, a small amount of Cl in the cell is being driven into the blood side via NBCn2 and KCC3, while a large amount moves to lumen via KCC4 co-transporter as well as Cl channels on the apical membrane. There is also a transport of this ion from the lumen into the cell via NKCC1.

Transport of HCO₃ from the blood side into the cell and from the cell into the lumen is facilitated by basolateral NBCn2 and apical NBCe2, respectively. The last important ion, K, on one hand is being passively transported mainly via paracellular route (tight junctions) from the blood into the lumen side, and on the other hand is being driven

from the blood side into cell via KCC3, located on the BLM, and then from the cell into the lumen via Na-K-ATPase pump, KCC4 co-transporter, and K channels.

AQP1 water channels that facilitate the transcellular water transport are highly concentrated on the apical membrane of CPE, however not many of these water channels are found on the BLM (Figure 19). On the paracellular route, Claudin-2 proteins found in the tight junctions of the CPE may also drive water passively from the blood side into the lumen.

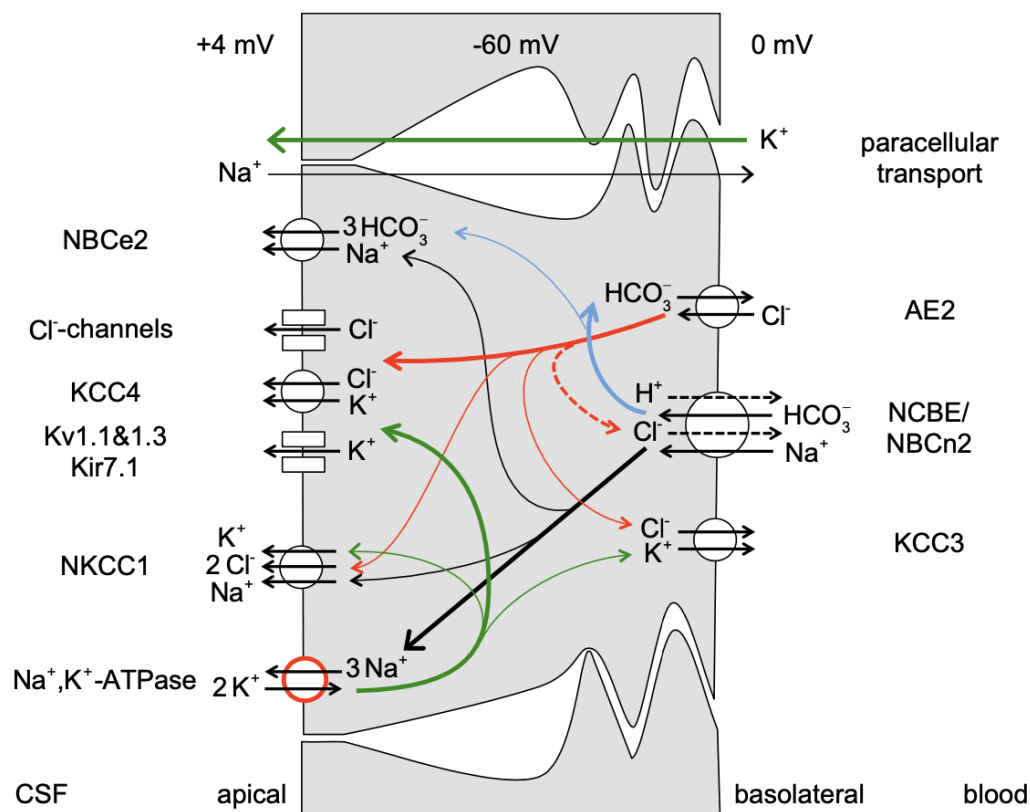


Figure 18: Proposed model by Damkier for the transcellular isotonic transport across CPE, [28].

The introduced model, sets a firm foundation that reveals ion and water transport across the CPE [28]. In the following subsection, we aim to propose a mathematical model that governs the mechanics of epithelial cells as well as fluid (water and solute) transport across them. There have been studies that model different characteristics of the epithelial cells separately, however to the best of my knowledge, there has never been a study to model the entire characteristic of this tissue., and in the next Chapter we specifically model the CPE.

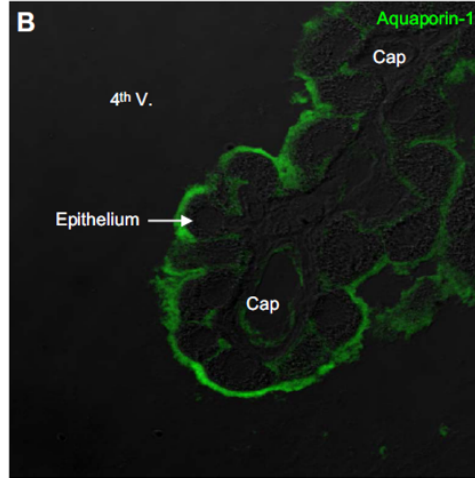


Figure 19: Highly expressed AQP1 water channels on the apical membrane [28].

3.4.1 Mathematical modelling of epithelial cells

In this section, we attempt to model typical epithelial cells accounting for its viscoelastic characteristic. The membranes have elastic membranes that possess channels and transporters that facilitate water and solute exchange. We couple mass and momentum conservation balances for the CPE, form equations that model the elastic membranes (i.e. BLM, APM) as well as water and solute exchanges between CPE and its surrounding media (i.e. Stroma and ventricles). We also model flux of water and solute across the tight junctions (i.e. paracellular transport).

Mass conservation of water and solutes

Water and solute must be conserved in the epithelial cells. This equation can be written similar to the ones derived for capillary in section 3.2. For water it is defined as,

$$l \frac{dA}{dt} = Q_{in} - Q_{out}. \quad (69)$$

and the mass conservation for solutes reads as,

$$l \frac{d}{dt} (AC_i) = Q_{in} C_{i,in} - Q_{out} C_{i,out}. \quad (70)$$

Where l , A , Q , and C are the hydraulic length, cross section area, flow rate, and solute concentrations, respectively.

Momentum conservation

To model the epithelial cells we utilise the momentum conservation balance, which states that the forces acting in a control volume must be conserved. For an incompressible control volume where the inertia and body forces are negligible, the formulation is,

$$\nabla \cdot \bar{\sigma} = 0. \quad (71)$$

where σ is a stress tensor. Since epithelial cells are a viscoelastic material, hence the relationship between stress and strain must be modelled. For the purpose of the current study, we take advantages of Kelvin-Voigt model as,

$$E\varepsilon_r(t) + \eta \frac{d\varepsilon_r(t)}{dt} - P_r = 0 \quad (72)$$

where ε is the strain and P is the normal stress (i.e. pressure) in the epithelial cells, E and η are elastic and viscosity constants.

3.4.2 Mathematical modelling of membranes & tight junctions

Several studies attempted to model the solute transport across epithelial cells in pancreas, proximal tubule, retinal pigment [148, 35, 132, 133] however no mathematical model have been introduced to model the transporters across the CPE. On the other hand, different epithelial cells possess different transporters; hence there is no general equation governing these transports. Regardless, in this section, we attempt to provide a very generic form of the transporters and in the next section write the specific ones will be written for each transporters.

Solute transport

As explained earlier, the transport of each solute i across epithelial cells interfaces IF are facilitated by means of active (primary (ATP) and secondary (SAT)) as well as passive

mechanisms (Channels (Ch)), which can be expressed in a general form as,

$$J_{i,IF} = J_{ATP} + \sum b_i J_{i,SAT} + J_{i,Ch} \quad (73)$$

The paracellular transport facilitated by tight junctions, unlike the channels, allow for solutes to be transported via both diffusion and advection mechanisms; therefore, the equation modelling this pathway is similar to the one derived for solute transport across endothelial cell membrane (Equation 18) as,

$$J_i = DB\Delta C_i + C_i(1 - \sigma_i)Q.$$

Water transport

Subsequently, water transport across CPE is similar to the one described across the endothelial cell membrane (Equation 20),

$$Q = Lp[\Delta P - RT\sigma_i(\Delta C_i)]$$

Note that the governing Equations must be evaluated separately for basal and apical membranes, as well as the tight junctions. These operations are taken to a later section, where all the equations are finalised (section 4.1).

Elasticity

Additional equations are required to be specified for the elastic membranes, for which the balances are similar to the one expressed for endothelial cell membrane. Recall the balance,

$$\nabla \cdot \bar{\bar{T}} + \bar{\pi} = 0.$$

The above relation is a balance between the tension on the membrane and the external load exerted to the membrane. First term on the left hand side is as explained previously

(i.e. section 3.2.1 ,Equation 22) can be expressed as,

$$\nabla \cdot \bar{\bar{T}} = -\left(\frac{1}{r}\right)\left(\frac{G}{1-\nu}\right)\left(\frac{r^2}{r_o^2} - 1 - \nu\right)$$

Subsequently, the second term is expressed as,

$$\vec{\pi} = (\bar{\sigma}_{ex} - \bar{\sigma}_{in}) \cdot \vec{n}. \quad (74)$$

The subscripts *ex* and *in* refer to the external and internal sides of the membrane of epithelial cell (BLM and APM). Therefore, this equation for an isolated epithelial cell can be written as,

$$\begin{aligned} \bar{\sigma}_{CPE} \cdot \vec{n} &= (\sigma_{CPE} \cdot n_r, 0, 0) \\ &= \left(\frac{P_{BLM}}{\theta}, 0, 0\right). \end{aligned} \quad (75)$$

Therefore,

$$\left(-\left(\frac{1}{r}\right)\left(\frac{G}{1-\nu}\right)\left(\frac{r^2}{r_o^2} - 1 - \nu\right) - \frac{P}{\theta}\right)_{BLM} = 0 \quad (76)$$

and for the APM side

$$\left(-\left(\frac{1}{r}\right)\left(\frac{G}{1-\nu}\right)\left(\frac{r^2}{r_o^2} - 1 - \nu\right) - \frac{P}{\theta}\right)_{APM} = 0 \quad (77)$$

Therefore Equations 76 and 77 govern the dynamics of elastic membranes bounding the CPE. Some of the terms in these equations are required to be evaluated either at their boundaries or/and at their compartment, for which these operations are taken to a dedicated section (section 4.2.2).

4 A Novel Microscopic Model for Choroid Plexus and CSF Production

4.1 Introduction

In this section, a close to real mathematical model, that mimics the mechanics of choroid plexus including CSF production, is developed. The primary motivation is to understand and explain the behaviour of this tissue in health, which has never been addressed before. Such investigations enable us to find answers for fundamental questions related to the characteristic of temporal CSF production signal from CP and the significance of CSF flux pulsatility. Furthermore, to examine the common assumptions in regards to neglecting the resistance induced by endothelial cells fenestrations in solute transport. In addition, to examine the dynamical behaviour of the compartments such Stroma and epithelial cells (CPE), which are impossible to access clinically.

In addition, the knowledge gap around the dynamics of CP operation in normal conditions has limited researchers to investigate the sensitivity of such organ to parameters contributing in CSF production and assess its behaviour in various scenarios ranging from ageing to diseased states. Therefore, developing such model provides a baseline for assessing the tissue against abnormal conditions (addressed in Chapter 4). It will also enable us to assess the subsystems which are impacted the most.

An additional use of such holistic model is to find a realistic boundary conditions for conducting 3D simulations of ventricular system (addressed in Chapter 5). This practice will significantly reduce the conjectures and disagreements about the fluid circulation in the system (discussed in Chapter 1, specifically Table 1).

4.2 Methodology

In the following, the proposed dynamic model for a single strand of choroid plexus is described. Then, the general equations derived for each medium as an isolated compartment (introduced in the previous chapter, e.g. section 3.2: blood vessels, section 3.3: Stroma, etc) would be finalised and adjusted to represent the sub-systems in the choroid plexus. The final version of the equations will be gathered in section 4.2.3. Finally, the

numerical method applied to the system is described.

4.2.1 Computational domain

Our proposed computational domain is shown in Figure 20. The model, similar to a real choroid plexus, is composed of seven different media: capillary vessel (Cap), endothelial cell membrane (EC), Stroma (St), basal membrane (BLM), choroid plexus epithelium (CPE), apical membrane (APM), and tight junctions (TJ).

The simplified system represents a layered cylinder, encompassing the blood vessel in the middle surrounded by layers mentioned above. The outset space represent the ventricular domain (Vent). The blood flow is unidirectional and along the longitudinal axis, Z , while flow of water and solute taking radial direction, r .

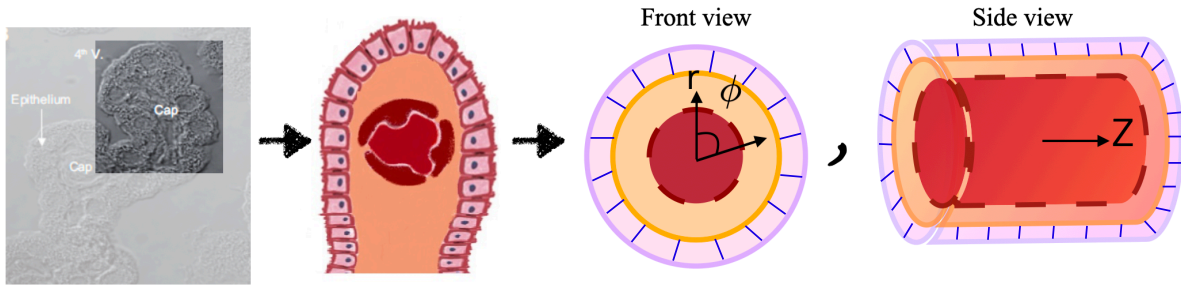


Figure 20: Proposed computational domain for one strand of choroid plexus (CP). The microscopic model consists of all 7 media that make up the CP: capillary, fenestrated endothelial cells, loose connective tissues, basal membrane, epithelium, apical membrane and tight junction.

The blood flowing through the capillaries of choroid plexus gets filtered across the fenestrated endothelial cells and flows radially into the adjacent compartment, Stroma. Since blood is composed of water and solutes, from now on, we refer to them separately and discuss their transport mechanisms. In literature, there is a general belief that the endothelial cells and Stroma impose small resistance to the flow based on the grounds that the endothelial cells of capillary have large fenestrations and Stroma is a loose connective tissue [14, 64, 28]. This assumption is challenged in our model based on the fact that fenestrations are not uniformly distributed and are not homogeneous [68, 121, 123, 120, 6]. In addition, Stroma can be considered as a proelastic medium, hence the transport of water and solutes may have different time and length scales.

Therefore, the solute transport across these compartments is facilitated by a combination of advection-diffusion phenomena. The magnitude of water filtration across the membranes is balanced by both hydrodynamic and osmotic pressures across this fenestrated barrier. The next stage in CSF production includes the movement of solutes and water across the Stroma to reach the other end (i.e. outer layer) of Stroma.

After passing through Stroma, there are two distinct routes for solutes and water to reach ventricles. First route is paracellular motion from the outer layer of Stroma through gaps between epithelial cells, called tight junctions (TJ). The second route is transcellular motion: across BLM into CPE and then across APM into the ventricles. These transportation are facilitated by special molecules located on the interfaces. For instance, claudin-2, CLDN-2, is a pore-forming protein are located at tight junctions, utilising paracellular transport of cations (e.g. sodium, potassium, etc) and water [28].

Transcellular transport of solutes across CPE takes place via transporters and channels located on the basal and apical membranes (BLM and APM). In particular, in our model, KCC3, NBCn1, NCBE, and AE2 are located on the BLM, and Na-K-ATP, KCC4, NKCC1, NBCe2, NHE, and K and Cl channels are located on APM (Figure 21). In addition, water transporting molecules, aquaporins -1 (AQP1), have been abundantly identified on BLM and APM [28], which is accounted in the model.

Finally, static and dynamic forces acting on all membranes, poroelastic Stroma and viscoelastic CPE causing displacements and deformation in the compartments are considered. In this model we considered radial displacement of media.

4.2.2 Formulation

In the last chapter, the generic form of equations for each compartment in the CP was derived. Note that the equations were driven for an isolated compartment. The unknown variables are of seven types: water flow rates Q , pressures P , radius r , cross sectional area A , surface area B , solute concentration C , and solute flux J . The subscript in each variable indicates the investigated medium and the sub-subscript specifies the location at which the variable is represented for (e.g. Q_{Capin} : flow at capillary inlet). Currently, the model accounts for 17 main solutes that exist in blood, however it has the capacity to

include further solutes. Considering the fact that blood is composed of different solutes (e.g. albumin, sodium, potassium, etc; Table 1 in [119] and Tables 2 and 4 in [120]), variables that are associated with solutes such as C and J have a further subscript i , representing their solute identity. Please refer to the Table 3 for the list of solutes and their corresponding identifier.

Capillary (Cap)

The integral form of mass conservation for water and solutes in a control volume resembling capillary (i.e. cylinder) were derived in section 3.2. This equation in choroid plexus reads as,

$$l \frac{dA_{Cap}}{dt} = Q_{Capin} - Q_{Capout} - Q_{EC}. \quad (78)$$

Subsequently, the mass conservation of solute in this compartment is,

$$l \frac{d}{dt} \left(A_{Cap} \frac{C_{i,Capin} + C_{i,Capout}}{2} \right) = Q_{Capin} C_{i,Capin} - Q_{Capout} C_{i,Capout} - J_{i,EC}. \quad (79)$$

and the Hagen Poissuille representing the momentum balance,

$$P_{in} - P_{out} = \frac{8\pi\mu l}{A_{Cap}^2} \left(\frac{Q_{Capin} + Q_{Capout}}{2} \right). \quad (80)$$

Endothelial cells (EC)

The solutes transport across endothelial cells is governed by advection-diffusion equation,

$$J_{i,EC} = D_{i,EC} B_{EC} \left(\frac{C_{i,Capin} + C_{i,Capout}}{2} - C_{i,St} \right) + (1 - \sigma_{i,EC}) \left(\frac{C_{i,Capin} + C_{i,Capout}}{2} + C_{i,St} \right) Q_{EC}. \quad (81)$$

and water flux across the medium is governed by,

$$Q_{EC} = L_{PEC} B_{EC} \left[\left(\frac{P_{in} + P_{out}}{2} - P_{Stin} \right) - RT \sigma_{i,EC} \left(\frac{C_{i,Capin} + C_{i,Capout}}{2} - C_{i,St} \right) \right]. \quad (82)$$

Note that this equation is a balance between hydrostatic pressure and osmotic pressure gradients. The aforementioned osmotic pressure gradient (i.e. $RT \sigma_{i,EC} \left(\frac{C_{i,Capin} + C_{i,Capout}}{2} - C_{i,St} \right)$) represents a situation in which the fluid is made up of one solute type, however

blood is composed of many different solute species. Therefore, the equation requires to be modified to include all solutes that exist in the fluid (refer to Table 3) and account for the sum of their molar concentration. This equation is rearranged as,

$$Q_{EC} = L_{PEC} B_{EC} \left[\left(\frac{P_{in} + P_{out}}{2} - P_{St_{in}} \right) - RT \sum_{i=1}^{17} \sigma_{i,EC} \left(\frac{C_{i,Cap_{in}} + C_{i,Cap_{out}}}{2} - C_{i,St} \right) \right]. \quad (83)$$

The equation for membrane deformability as a function of radius r , displacement d , and pressure P gradient imposed on the membrane from capillary and Stroma can be written as,

$$-\left(\frac{1}{r}\right)\left(\frac{G}{1-\nu}\right)\left(\frac{r^2}{r_o^2} - 1 - \nu\right) - \left(\frac{E \frac{\partial d}{\partial r} - (1+\nu)P_r}{\theta}\right)_{St_{in}} - P_{Cap} = 0. \quad (84)$$

where θ is the membrane thickness and can be estimated as,

$$2\pi r_o \theta_o = 2\pi r_o \theta,$$

$$\theta = \frac{r_o \theta_o}{r}.$$

the subscript o is devoted to the initial state of the variables. Assuming the radius at rest is presented by R (i.e. $r_o = R$) and the displacement of the membrane is a difference between the radius at each time and at rest (i.e. $d = r - R$)., The above equation governing the elasticity of the membrane can be stated as,

$$\theta_{o_{EC}} \left(\frac{G}{1-\nu} \right)_{EC} \left((1+\nu) \frac{R_{EC}}{r_{EC}^2} - \frac{1}{R_{EC}} \right) - E_{St} \left[\frac{r_{BLM} - r_{EC}}{R_{BLM} - R_{EC}} - 1 \right] + (1+\nu_{St}) P_{St_{in}} - P_{Cap} = 0. \quad (85)$$

Stroma (St)

The equations governing the fluid and solid behaviours in the Stroma were explained in section 3.3, which require appropriate boundary conditions. Restating Equation 65,

$$S \frac{d \langle P \rangle}{dt} + \frac{k}{\mu} \frac{2}{r_o^2 - r_i^2} \left[r_o \left(\frac{\partial P}{\partial r} \right)_{r_o} - r_i \left(\frac{\partial P}{\partial r} \right)_{r_i} \right] + \frac{2\alpha}{r_o^2 - r_i^2} \left[r_o \left(\frac{\partial d}{\partial t} \right)_{r_o} - r_i \left(\frac{\partial d}{\partial t} \right)_{r_i} \right] = 0.$$

since Stroma is bounded from the inner and outer sides by the endothelial cells and the basolateral membranes, respectively, the subscripts i and o denote variables to be evaluated at the inner and outer membranes. Substituting for definition of displacement

d as defined in the previous section (i.e. $d = r - R$) the above equation can be rewritten as,

$$S \frac{d}{dt} \left(\frac{P_{St_{in}} + P_{St_{out}}}{2} \right) - \frac{k}{\mu} \frac{2}{r_{BLM}^2 - r_{EC}^2} \left[r_{BLM} \left(\frac{\partial P}{\partial r} \right)_{r_{BLM}} - r_{EC} \left(\frac{\partial P}{\partial r} \right)_{r_{EC}} \right] + \frac{2\alpha}{r_{BLM}^2 - r_{EC}^2} \left[r_{BLM} \frac{dr_{BLM}}{dt} - r_{EC} \frac{dr_{EC}}{dt} \right] = 0 \quad (86)$$

In addition, taking the pressures to vary linearly in the radial direction (i.e. $(\frac{\partial P}{\partial r})_{r_{BLM}} = (\frac{\partial p}{\partial r})_{r_{EC}}$), the above equation can be written as,

$$S \frac{d}{dt} \left(\frac{P_{St_{in}} + P_{St_{out}}}{2} \right) - \frac{k}{\mu} \frac{2}{r_{BLM}^2 - r_{EC}^2} \frac{\partial P}{\partial r} (r_{BLM} - r_{EC}) + \frac{2\alpha}{r_{BLM}^2 - r_{EC}^2} \left[r_{BLM} \frac{dr_{BLM}}{dt} - r_{EC} \frac{dr_{EC}}{dt} \right] = 0. \quad (87)$$

and finalised as,

$$S \frac{d}{dt} \left(\frac{P_{St_{in}} + P_{St_{out}}}{2} \right) - \frac{k}{\mu} \frac{2}{r_{BLM}^2 - r_{EC}^2} [P_{St_{out}} - P_{St_{in}}] + \frac{2\alpha}{r_{BLM}^2 - r_{EC}^2} \left[r_{BLM} \frac{dr_{BLM}}{dt} - r_{EC} \frac{dr_{EC}}{dt} \right] = 0. \quad (88)$$

An additional equation governing the physics in Stroma is solute concentration, similar to the one derived in the capillary subsection. It can be written for Stroma as,

$$l \frac{d}{dt} (A_{St} C_{i,St}) = J_{i,EC} - J_{i,BLM} - J_{i,TJ} \quad (89)$$

Choroid plexus epithelium (CPE)

The mass conservation of water inside the CPE is governed by,

$$l \frac{dA_{CPE}}{dt} = Q_{BLM} - Q_{APM} \quad (90)$$

However, there is a significant body of research emphasising on importance of intercellular PH regulation in epithelial cells [92, 80, 28, 25]. Therefore, we account for the maintenance

of intercellular PH by adding a term to the above equation,

$$l \frac{dA_{CPE}}{dt} = Q_{BLM} - Q_{APM} - Q_{PH} \quad (91)$$

where $Q_{PH} = M J_{buff}$. M is a constant and J_{buff} is the amount of water produced in the epithelial cells from the reaction of hydrogen and bicarbonate. To elaborate further, one mole of hydrogen and one mole of bicarbonate can react to form water and carbon dioxide. Hence, the production of water means destroying the two mentioned ones. Subsequently, the solute mass conservation is rearranged as,

$$l \frac{d}{dt} (A_{CPE} C_{i,CPE}) = J_{i,BLM} - J_{i,APM} \quad (92)$$

The above equation stands for all solutes, except when computing the solute conservation for hydrogen and bicarbonate. These equations include an additional term for J_{buff} , as

$$l \frac{d}{dt} (A_{CPE} C_{i,CPE}) = J_{i,BLM} - J_{i,APM} + J_{buff}. \quad (93)$$

The relationship between stress and strain described and derived for the CPE in section 3.4.1 must be finalised to govern the viscoelasticity of CPE. Recall Equation 72 as,

$$E \varepsilon_r(t) + \eta \frac{d\varepsilon_r(t)}{dt} - P_r = 0$$

This equation should be evaluated at its boundaries, which are bounded from the inside by the basal membrane and the outside by the apical membrane including the tight junctions. $\varepsilon = \frac{r_{CPE} - R_{CPE}}{R_{CPE}}$, where r is the variable radius and R is the computed for the membrane at rest. In addition, $r_{CPE} = r_{APM} - r_{BLM}$. Substituting for these, we have

$$E \left(\frac{r_{APM} - R_{BLM} - R_{CPE}}{R_{CPE}} \right) + \eta \frac{d}{dt} \left(\frac{r_{APM} - r_{BLM}}{R_{CPE}} \right) - P_{APM} + P_{BLM} = 0 \quad (94)$$

Basal & Apical membrane (BLM & APM)

The next sets of equations govern the transcellular solute transportation across the membranes (i.e. basal and apical). Recall that there exist different transporters on each membrane, each of which facilitate movement of certain ions. A limitation to this model is that it does not account for the ionic charge nor most the chemical reactions of ions. For more convenience, a choroid plexus epithelium (CPE) with all its transporters is sketched in Figure 21.

As apparent, KCC3, NCBn1, NBCe, and AE2 exist on basal membrane. Subsequently, Na-K- ATPase pump, KCC4, NKCC1, and NBCe2, and NHE are located on APM, and there are two channels dedicated to K and Cl transports. All these transporters have been modelled in the following. For simplicity we have given the concentration of each solute a number according to Table 3, i.e. $C_{Cl} = C_4$, $C_{Na} = C_6$, $C_{HCO_3} = C_8$, $C_K = C_{10}$, $C_H = C_{17}$.

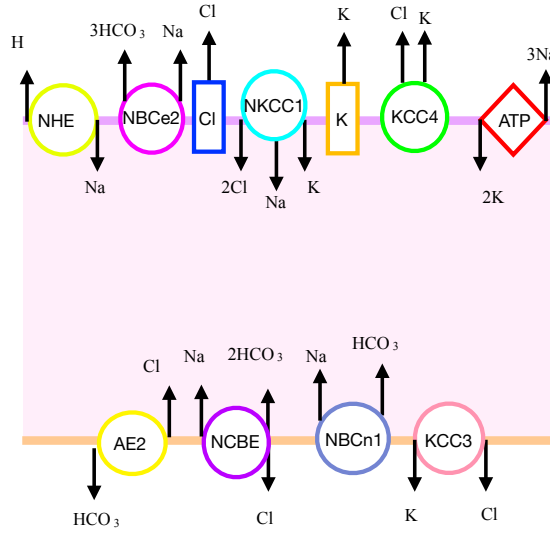


Figure 21: The sketch depicts one unit of CPE with all the protein transporters on membrane.

The transporters on basal membranes are,

$$J_{KCC3} = M_{KCC3} B_{BLM} \frac{C_{4,St} C_{10,St} - C_{4,CPE} C_{10,CPE}}{K_4 K_{10} \left(1 + \frac{C_{4,St}}{K_4} + \frac{C_{10,St}}{K_{10}}\right) \left(1 + \frac{C_{4,CPE}}{K_4} + \frac{C_{10,CPE}}{K_{10}}\right)} \quad (95)$$

$$J_{NBCn1} = M_{NBCn} B_{BLM} \frac{C_{6,St} C_{8,St} - C_{6,CPE} C_{8,CPE}}{K_6 K_8 \left[(1 + C_{6,St}/K_6 + C_{6,St} C_{8,St}/K_6 K_8) (1 + C_{6,CPE} C_{8,CPE}/K_6 K_8) + (1 + C_{6,CPE}/K_6 + C_{6,CPE} C_{8,CPE}/K_6 K_8) (1 + C_{6,St} C_{8,St}/K_6 K_8) \right]} \quad (96)$$

$$J_{NCBE} = M_{NCBe} B_{BLM} \frac{C_{6,St} (C_{8,St})^2 C_{4,CPE} - C_{6,CPE} (C_{8,CPE})^2 C_{4,St}}{K_4 K_6 K_8^2 \left[(1 + \frac{C_{4,CPE}}{K_4}) (1 + \frac{C_{6,CPE}}{K_6}) (1 + \frac{C_{8,CPE}}{K_8})^2 \cdot (C_{4,St}/K_4 + C_{6,St}/K_6 + 2C_{8,St}/K_8) + (1 + \frac{C_{4,St}}{K_4}) (1 + \frac{C_{6,St}}{K_6}) (1 + \frac{C_{8,St}}{K_8})^2 \cdot (C_{4,CPE}/K_4 + C_{6,CPE}/K_6 + 2C_{8,CPE}/K_8) \right]} \quad (97)$$

$$J_{AE2} = M_{AE2} B_{BLM} \frac{C_{4,St} C_{8,CPE} - C_{4,CPE} C_{8,St}}{K_4 K_8 \left[(1 + C_{4,CPE}/K_4 + C_{8,CPE}/K_8) (C_{4,St}/K_4 + C_{8,St}/K_8) + (1 + C_{4,St}/K_4 + C_{8,St}/K_8) (C_{4,CPE}/K_4 + C_{8,CPE}/K_8) \right]} \quad (98)$$

and the equations modelling the pump on apical membranes is,

$$J_{ATP} = M_{ATP} B_{APM} \left(\frac{C_{6,CPE}}{R_6 + C_{6,CPE}} \right)^3 \left(\frac{C_{10,Vent}}{R_{10} + C_{10,Vent}} \right)^2$$

$$R_6 = 0.2 \left(1 + \frac{C_{10,CPE}}{8.33 \times 10^3} \right), \quad (99)$$

$$R_{10} = 0.1 \left(1 + \frac{C_{6,Vent}}{18.5 \times 10^3} \right).$$

and the transporters,

$$J_{KCC4} = M_{KCC4} B_{APM} \frac{C_{4,CPE} C_{10,CPE} - C_{10,Vent} C_{4,Vent}}{K_4 K_{10} \left(1 + \frac{C_{4,CPE}}{K_4} + \frac{C_{10,CPE}}{K_{10}} \right) \left(1 + \frac{C_{4,Vent}}{K_4} + \frac{C_{10,Vent}}{K_{10}} \right)} \quad (100)$$

$$J_{NKCC1} = \frac{M_{NKCC1} B_{APM}}{K_4^2 K_6 K_{10}} \frac{C_{4,CPE}^2 C_{6,CPE} C_{10,CPE} - C_{4,Vent}^2 C_{6,Vent} C_{10,Vent}}{\left(1 + \frac{C_{6,CP}}{K_6} + \frac{C_{6,CP}}{K_6} \frac{C_{4,CP}}{K_4} + \frac{C_{6,CP}}{K_6} \frac{C_{10,CP}}{K_{10}} \frac{C_{4,CP}}{K_4} + \frac{C_{6,CP}}{K_6} \frac{C_{10,CP}}{K_{10}} \frac{C_{4,CP}^2}{K_4^2} \right) \cdot \left(1 + \frac{C_{6,Vent}}{K_6} \frac{C_{10,Vent}}{K_{10}} \frac{C_{4,Vent}^2}{K_4^2} \right) + \left(1 + \frac{C_{4,Vent}}{K_4} + \frac{C_{10,Vent}}{K_{10}} \frac{C_{4,Vent}}{K_4} + \frac{C_{10,Vent}}{K_{10}} \frac{C_{4,Vent}^2}{K_4^2} + \frac{C_{6,Vent}}{K_6} \frac{C_{10,Vent}}{K_{10}} \frac{C_{4,Vent}^2}{K_4^2} \right) \cdot \left(1 + \frac{C_{6,CP}}{K_6} \frac{C_{10,CP}}{K_{10}} \frac{C_{4,CP}^2}{K_4^2} \right)}$$

$$J_{NBCe2} = M_{NBCe2} B_{APM} \frac{C_{6,CPE} C_{8,CPE}^3 - C_{6,Vent} C_{8,Vent}^3}{K_6 K_8^3 \left[(1 + C_{6,CPE}/K_6 + C_{6,CPE} C_{8,CPE}^3 / K_6 K_8^3) (1 + C_{6,Vent} C_{8,Vent}^3 / K_6 K_8^3) + (1 + C_{6,Vent}/K_6 + C_{6,Vent} C_{8,Vent}^3 / K_6 K_8^3) (1 + C_{6,CPE} C_{8,CPE}^3 / K_6 K_8^3) \right]}$$

$$J_{NHE} = M_{NHE} B_{APM} \frac{C_{17,CPE} C_{6,Vent} - C_{17,Vent} C_{6,CPE}}{K_6 K_{17} \left[(1 + C_{6,Vent}/K_6 + C_{17,Vent}/K_{17}) (C_{6,CPE}/K_6 + C_{17,CPE}/K_{17}) + (1 + C_{6,CPE}/K_6 + C_{17,CPE}/K_{17}) (C_{6,Vent}/K_6 + C_{17,Vent}/K_{17}) \right]}$$

These equations were taken from [162, 132, 134, 148, 157, 35, 164].

Channels are very selective and uptake only one type of molecules for transport. In our modelling, we found that a simple flux equation does not provide accurate results for channel modelling. Therefore, we take advantages of Goldman–Hodgkin–Katz equation, which considers the transmembrane potential as well as the concentration gradients of ions as,

$$\begin{aligned} J_{6,Ch} &= D_{K,Ch} B_{APM} (C_{K,CPE} - o * C_{K,Vent}), \\ J_{4,Ch} &= D_{Cl,Ch} B_{APM} (C_{Cl,CPE} - n * C_{Cl,Vent}), \end{aligned} \quad (101)$$

where o and n are constants. In addition, the paracellular transport via tight junction is governed by,

$$J_{i,TJ} = D_{i,TJ} B_{APM} (C_{i,S} - C_{i,Vent}) + (1 - \sigma_{i,Tj}) \left(\frac{C_{i,Vent} + C_{i,St}}{2} \right) Q_{TJ} \quad (102)$$

Subsequently, the water transport across the basal and apical membrane as well as the tight junction,

$$Q_{BLM} = L_{pBLM} B_{BLM} \left[\left(P_{Stout} - \frac{P_{BLM} + P_{APM}}{2} \right) - RT \sum_{i=1}^{16} \sigma_{i,BLM} (C_{i,St} - C_{i,CPE}) \right]. \quad (103)$$

$$Q_{APM} = L_{pAPM} B_{APM} \left[\left(\frac{P_{BLM} + P_{APM}}{2} - P_{Vent} \right) - RT \sum_{i=1}^{16} \sigma_{i,APM} (C_{i,CPE} - C_{i,Vent}) \right]. \quad (104)$$

$$Q_{TJ} = Lp_{TJ}B_{APM} \left[\left(P_{Stout} - P_{Vent} \right) - RT \sum_{i=1}^{16} \sigma_{i,TJ} \left(C_{i,St} - C_{i,Vent} \right) \right]. \quad (105)$$

The last sets of equations govern elasticity of the membranes (i.e. basal and apical) are defined as,

$$\theta_{o_{BLM}} \left(\frac{G}{1-\nu} \right)_{BLM} \left((1+\nu) \frac{R_{BLM}}{r_{BLM}^2} - \frac{1}{R_{BLM}} \right) + E_{St} \left[\frac{r_{BLM} - r_{EC}}{R_{BLM} - R_{EC}} - 1 \right] - (1+\nu_{St}) P_{Stout} + P_{BLM} = 0.$$

$$\theta_{o_{APM}} \left(\frac{G}{1-\nu} \right)_{APM} \left((1+\nu) \frac{R_{APM}}{r_{APM}^2} - \frac{1}{R_{APM}} \right) - P_{APM} + P_{Vent} = 0.$$

4.2.3 Governing equations

In the previous section, we finalised the equations that model each media. In this section, we gather all the governing equations, arrange them in a manner that all the similar type of equations are in one category. Note that some equations are solute i dependent and must be written for each solute, separately. Some of these equations will be written in a compact form (i.e. equations for variables such as $J_{i,EC}$ must be written for all solutes, hence since there exist 17 solutes in the model, we repeat this equation 17 times: each equation is written for one solute). As a result, we have 171 equations, the unknown variables that we will solve for, shown in red, are of seven types (i.e. water flux (Q), solute flux (J), Pressure (P), Concentration (C), cross section and surface areas (A and B), as well as the radius for each compartment (r). The inlet and outlet conditions in blue and the constant parameters in black, the choice of which are described in subsection 4.2.4 .

Time integration was implemented by applying implicit Euler scheme. The discretised system was solved numerically in MATLAB using Newton-Raphson method.

Mass conservation: Water

$$l \frac{dA_{Cap}}{dt} = Q_{Capin} - Q_{Capout} - Q_{EC}.$$

$$l \frac{dA_{St}}{dt} = Q_{EC} - Q_{BLM} - Q_{TJ}.$$

$$l \frac{dA_{Vent}}{dt} = Q_{APM} + Q_{TJ} - Q_{Ventout}.$$

$$l \frac{dA_{CPE}}{dt} = Q_{BLM} - Q_{APM} - M J_{buf}.$$

Mass conservation of Solute

$$l \frac{d}{dt} \left(A_{Cap} \frac{C_{i,Capin} + C_{i,Capout}}{2} \right) = Q_{Capin} C_{i,Capin} - Q_{Capout} C_{i,Capout} - J_{i,EC}.$$

$$l \frac{d}{dt} \left(A_{St} C_{i,St} \right) = J_{i,EC} - J_{i,BLM} - J_{i,TJ}.$$

$$l \frac{d}{dt} (A_{Vent} C_{i,Vent}) = J_{i,TJ} + J_{i,APM} - Q_{Vent_{out}} C_{i,Vent}.$$

$$l \frac{d}{dt} (A_{CPE} C_{i,CPE}) = J_{i,BLM} - J_{i,APM}.$$

$$l \frac{d}{dt} (A_{CPE} C_{8,CPE}) = J_{8,BLM} + J_{buff} - J_{8,APM}.$$

$$C_{17,CPE} = 10^{-PH} \times 10^3$$

$$l \frac{d}{dt} (A_{CPE} C_{17,CPE}) = J_{buff} - J_{17,APM} + J_{17,BLM}.$$

Solute transport

$$J_{i,EC} = D_{i,EC} B_{Cap} \left(\frac{C_{i,Cap_{in}} + C_{i,Cap_{out}}}{2} - C_{i,St_{in}} \right) \\ + (1 - \sigma_{i,EC}) * \left[\left(\frac{C_{i,Cap_{in}} + C_{i,Cap_{out}}}{2} \right) + C_{i,St} \right] Q_{EC}.$$

$$J_{(1:3,5,7,9,11:16),BLM} = 0$$

$$J_{4,BLM} = J_{AE2} + J_{KCC3} - J_{NCBE}$$

$$J_{6,BLM} = J_{NCBe} + J_{NBCn1} + (1 - \sigma_{6,BLM}) (C_{6,St} + C_{6,CPE}) Q_{BLM}$$

$$J_{8,BLM} = 2J_{NCBe} - J_{AE2} + J_{NBCn1}$$

$$J_{10,BLM} = J_{KCC3} + (1 - \sigma_{10,BLM}) (C_{10,St} + (C_{10,CPE})) Q_{BLM}$$

$$J_{17,BLM} = (1 - \sigma_{17,BLM}) (C_{17,St} + C_{17,CPE}) Q_{BLM}$$

$$J_{i,TJ} = D_{i,TJ} B_{APM} (C_{i,St} - C_{i,Vent}) + (1 - \sigma_{i,TJ}) (C_{i,St} + (C_{i,Vent})) Q_{TJ}.$$

$$J_{(1:3,5,7,9,11:16),APM} = 0$$

$$J_{4,APM} = J_{KCC4} + 2J_{NKCC1} + J_{4,Ch}$$

$$J_{6,APM} = 3J_{ATP} + J_{NKCC1} + J_{NBCe2} - J_{NHE} + (1 - \sigma_{6,APM}) (C_{6,CPE} + C_{6,Vent}) Q_{APM}$$

$$J_{8,APM} = 3J_{NBCe2}$$

$$J_{10,APM} = -2J_{ATP} + J_{KCC4} + J_{NKCC1} + J_{10,Ch} + (1 - \sigma_{10,APM}) (C_{10,CPE} + C_{10,Vent}) Q_{APM}$$

$$J_{17,APM} = J_{NHE} + (1 - \sigma_{17,APM}) \left(C_{17,CPE} + C_{17,Vent} \right) Q_{APM}$$

Momentum balance

$$(P_{in} - P_{out}) A_{Cap}^2 = 8\pi\mu l \left(\frac{Q_{Capin} + Q_{Capout}}{2} \right).$$

$$S \frac{d}{dt} \left(\frac{P_{Stin} + P_{Stout}}{2} \right) (r_{BLM}^2 - r_{EC}^2) - \frac{2k}{\mu} [P_{Stout} - P_{Stin}] \\ + \frac{\alpha}{\pi} \frac{dA_{St}}{dt} = S (Q_{BLM} + Q_{TJ} - Q_{EC}) \frac{P_{Stin} + P_{Stout}}{2\pi l}.$$

$$E_{CPE} (r_{APM} - r_{BLM} - (R_{APM} - R_{BLM})) + \eta \frac{d}{dt} (r_{APM} - r_{BLM}) = 0$$

Water transport

$$Q_{EC} = Lp_{EC} B_{EC} \left[\left(\frac{P_{in} + P_{out}}{2} - P_{Stin} \right) - RT \sum_{i=1}^{17} \sigma_{i,EC} \left(\frac{C_{i,Capin} + C_{i,Capout}}{2} - C_{i,St} \right) \right].$$

$$Q_{BLM} = Lp_{BLM} B_{BLM} \left[\left(P_{Stout} - \frac{P_{BLM} + P_{APM}}{2} \right) - RT \sum_{i=1}^{17} \sigma_{i,BLM} (C_{i,St} - C_{i,CPE}) \right].$$

$$Q_{TJ} = Lp_{TJ} B_{APM} \left[(P_{Stout} - P_{Vent}) - RT \sum_{i=1}^{17} \sigma_{i,TJ} (C_{i,St} - C_{i,Vent}) \right].$$

$$Q_{APM} = Lp_{APM} B_{APM} \left[\left(\frac{P_{BLM} + P_{APM}}{2} - P_{Vent} \right) - RT \sum_{i=1}^{17} \sigma_{i,APM} (C_{i,CPE} - C_{i,Vent}) \right].$$

Elasticity

$$\theta_{oEC} \left(\frac{G}{1-\nu} \right)_{EC} \left((1+\nu) \frac{R_{EC}}{r_{EC}^2} - \frac{1}{R_{EC}} \right) - E_{St} \left[\frac{r_{BLM} - r_{EC}}{R_{BLM} - R_{EC}} - 1 \right] + (1+\nu_{St}) P_{Stin} - \frac{P_{in} + P_{out}}{2} = 0.$$

$$\theta_{oBLM} \left(\frac{G}{1-\nu} \right)_{BLM} \left((1+\nu) \frac{R_{BLM}}{r_{BLM}^2} - \frac{1}{R_{BLM}} \right) + E_{St} \left[\frac{r_{BLM} - r_{EC}}{R_{BLM} - R_{EC}} - 1 \right] - (1+\nu_{St}) P_{Stout} + P_{BLM} = 0.$$

$$\theta_{oAPM} \left(\frac{G}{1-\nu} \right)_{APM} \left((1+\nu) \frac{R_{APM}}{r_{APM}^2} - \frac{1}{R_{APM}} \right) - P_{APM} + P_{Vent} = 0.$$

Area

$$A_{Cap} = \pi r_{EC}^2.$$

$$A_{St} = \pi(r_{BLM}^2 - r_{EC}^2).$$

$$A_{CPE} = \pi(r_{APM}^2 - r_{BLM}^2).$$

$$A_{Vent} = \pi(r_{Vent}^2 - r_{APM}^2).$$

$$B_{EC} = 2\pi r_{EC} l.$$

$$B_{BLM} = 2\pi r_{BLM} l.$$

$$B_{APM} = 2\pi r_{APM} l.$$

Transporters

$$J_{KCC3} = M_{KCC3} B_{BLM} \frac{C_{4,St} C_{10,St} - C_{10,CPE} C_{4,CPE}}{K_4 K_{10} \left(1 + \frac{C_{4,St}}{K_4} + \frac{C_{10,St}}{K_{10}}\right) \left(1 + \frac{C_{4,CPE}}{K_4} + \frac{C_{10,CPE}}{K_{10}}\right)}$$

$$J_{NBCn1} = M_{NBCn} B_{BLM} \frac{C_{6,St} C_{8,St} - C_{6,CPE} C_{8,CPE}}{K_6 K_8 \left[\left(1 + \frac{C_{6,St}}{K_6} + \frac{C_{6,St} C_{8,St}}{K_6 K_8}\right) \left(1 + \frac{C_{6,CPE} C_{8,CPE}}{K_6 K_8}\right) + \left(1 + \frac{C_{6,CPE}}{K_6} + \frac{C_{6,CPE} C_{8,CPE}}{K_6 K_8}\right) \left(1 + \frac{C_{6,St} C_{8,St}}{K_6 K_8}\right) \right]}$$

$$J_{NCBE} = M_{NCBe} B_{BLM} \frac{C_{6,St} (C_{8,St})^2 C_{4,CPE} - C_{6,CPE} (C_{8,CPE})^2 C_{4,St}}{K_4 K_6 K_8^2 \left[\left(1 + \frac{C_{4,CPE}}{K_4}\right) \left(1 + \frac{C_{6,CPE}}{K_6}\right) \left(1 + \frac{C_{8,CPE}}{K_8}\right)^2 \cdot (C_{4,St}/K_4 + C_{6,St}/K_6 + 2C_{8,St}/K_8) + \left(1 + \frac{C_{4,St}}{K_4}\right) \left(1 + \frac{C_{6,St}}{K_6}\right) \left(1 + \frac{C_{8,St}}{K_8}\right)^2 \cdot (C_{4,CPE}/K_4 + C_{6,CPE}/K_6 + 2C_{8,CPE}/K_8) \right]}$$

$$J_{AE2} = M_{AE2} B_{BLM} \frac{C_{4,St} C_{8,CPE} - C_{4,CPE} C_{8,St}}{K_4 K_8 \left[\left(1 + \frac{C_{4,CPE}}{K_4} + \frac{C_{8,CPE}}{K_8}\right) \left(\frac{C_{4,St}}{K_4} + \frac{C_{8,St}}{K_8}\right) + \left(1 + \frac{C_{4,St}}{K_4} + \frac{C_{8,St}}{K_8}\right) \left(\frac{C_{4,CPE}}{K_4} + \frac{C_{8,CPE}}{K_8}\right) \right]}$$

$$J_{ATP} = P_{maxATP} B_{APM} \left(\frac{C_{6,CPE}}{R_6 + C_{6,CPE}}\right)^3 \left(\frac{C_{10,Vent}}{R_{10} + C_{10,Vent}}\right)^2$$

$$R_6 = 0.2 \left(1 + \frac{C_{10,CPE}}{8.33 \times 10^3} \right)$$

$$R_{10} = 0.1 \left(1 + \frac{C_{6,Vent}}{18.5 \times 10^3} \right)$$

$$J_{KCC4} = M_{KCC4} B_{APM} \frac{C_{4,CPE} C_{10,CPE} - C_{10,Vent} C_{4,Vent}}{K_4 K_{10} \left(1 + \frac{C_{4,CPE}}{K_4} + \frac{C_{10,CPE}}{K_{10}} \right) \left(1 + \frac{C_{4,Vent}}{K_4} + \frac{C_{10,Vent}}{K_{10}} \right)}$$

$$J_{NKCC1} = \frac{M_{NKCC1} B_{APM}}{K_4^2 K_6 K_{10}} \frac{C_{4,CPE}^2 C_{6,CPE} C_{10,CPE} - C_{4,Vent}^2 C_{6,Vent} C_{10,Vent}}{\left(1 + \frac{C_{6,CP}}{K_6} + \frac{C_{6,CP}}{K_6} \frac{C_{4,CP}}{K_4} + \frac{C_{6,CP}}{K_6} \frac{C_{10,CP}}{K_{10}} \frac{C_{4,CP}}{K_4} + \frac{C_{6,CP}}{K_6} \frac{C_{10,CP}}{K_{10}} \frac{C_{4,CP}^2}{K_4^2} \right) \cdot \left(1 + \frac{C_{6,Vent}}{K_6} \frac{C_{10,Vent}}{K_{10}} \frac{C_{4,Vent}^2}{K_4^2} \right) + \left(1 + \frac{C_{4,Vent}}{K_4} + \frac{C_{10,Vent}}{K_{10}} \frac{C_{4,Vent}}{K_4} + \frac{C_{10,Vent}}{K_{10}} \frac{C_{4,Vent}^2}{K_4^2} + \frac{C_{6,Vent}}{K_6} \frac{C_{10,Vent}}{K_{10}} \frac{C_{4,Vent}^2}{K_4^2} \right) \cdot \left(1 + \frac{C_{6,CP}}{K_6} \frac{C_{10,CP}}{K_{10}} \frac{C_{4,CP}^2}{K_4^2} \right)}$$

$$J_{NBCe2} = M_{NBCe2} B_{APM} \frac{C_{6,CPE} C_{8,CPE}^3 - C_{6,Vent} C_{8,Vent}^3}{K_6 K_8^3 \left[\left(1 + C_{6,CPE}/K_6 + C_{6,CPE} C_{8,CPE}^3 / K_6 K_8^3 \right) \left(1 + C_{6,Vent} C_{8,Vent}^3 / K_6 K_8^3 \right) + \left(1 + C_{6,Vent}/K_6 + C_{6,Vent} C_{8,Vent}^3 / K_6 K_8^3 \right) \left(1 + C_{6,CPE} C_{8,CPE}^3 / K_6 K_8^3 \right) \right]}$$

$$J_{NHE} = M_{NHE} B_{APM} \frac{C_{17,CPE} C_{6,Vent} - C_{17,Vent} C_{6,CPE}}{K_6 K_{17} \left[\left(1 + C_{6,Vent}/K_6 + C_{17,Vent}/K_{17} \right) \left(C_{6,CPE}/K_6 + C_{17,CPE}/K_{17} \right) + \left(1 + C_{6,CPE}/K_6 + C_{17,CPE}/K_{17} \right) \left(C_{6,Vent}/K_6 + C_{17,Vent}/K_{17} \right) \right]}$$

$$J_{4,Ch} = D_{4,Ch} B_{APM} (C_{4,CPE} - o C_{4,Vent})$$

$$J_{10,Ch} = D_{10,Ch} B_{APM} (C_{10,CPE} - n C_{10,Vent})$$

4.2.4 Conditions and constants

Choroid plexus is an understudied organ in with a limited quantitative data available in literature addressing its mechanics. This lack in clinical measurements impose a challenge upon the choice of parameter to be input in the model. However, the main purpose for this study is not to determine the exact values for the parameters, but to understand the system and assess its sensitivity to the parameters. Regardless of the argument, we

did our best to obtain, interpret, and justify the parameters that will be further used as baseline input in the model. These parameters are also collected in Tables and the justification is discussed below.

Inlet and outlet conditions

The inlet conditions to the model are of four types: pressure inlet to the capillary, P_{in} , flow influx to the capillary Q_{Capin} , pressure in ventricular system P_{Vent} , and blood composition $C_{i,Capin}$. The first three variables (i.e. P_{in} , Q_{Capin} and P_{Vent}) are taken from a previously developed mathematical model, which is presented and described is in Appendix A. The profiles for the first three aforementioned variables are shown below.

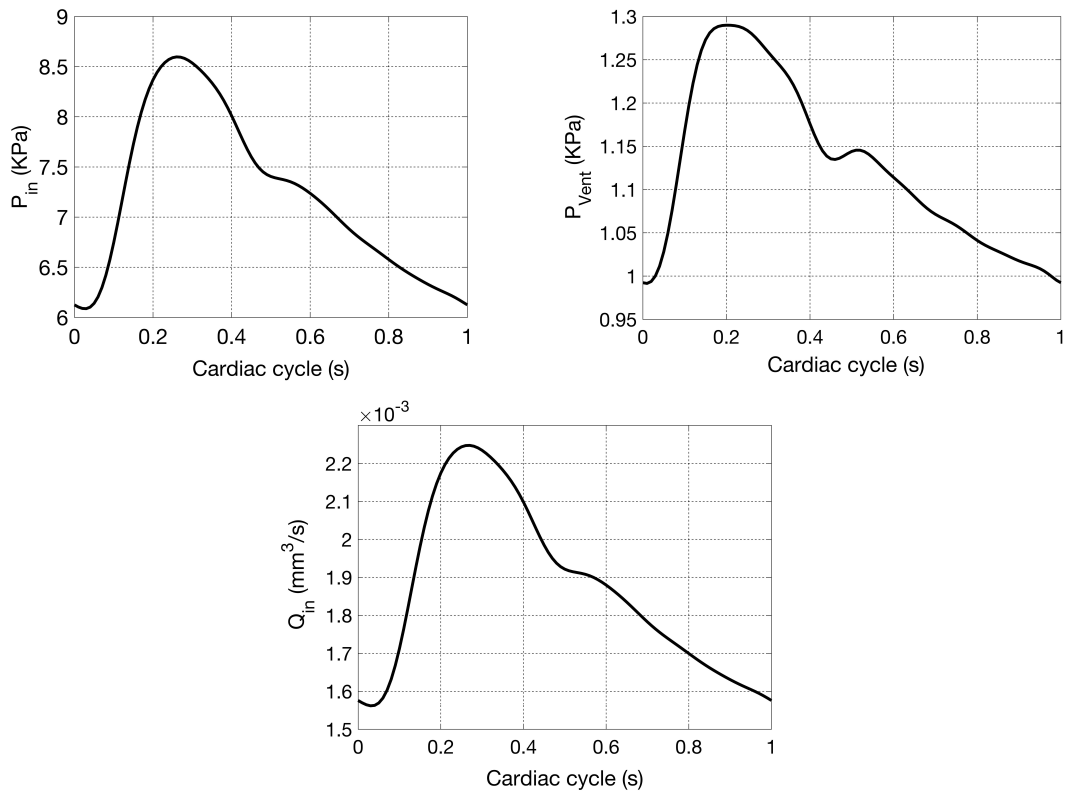


Figure 22: Inlet and outlet conditions for the model. Top left: inlet profile for pressure distribution at capillary. Top right: outlet profile for pressure distribution at ventricle. Bottom: flow inlet profile at capillary inlet.

The concentration inlet to the model is taken from blood from different sources (e.g.

i	Constituent	Symbol	C_{blood}
1	Albumin	Alb	0.64
2	Globulin	Glo	0.05
3	Fibrinogen	Fib	0.006
4	Chloride	Cl	101
5	Cholesterol	Chol	4.14
6	Sodium	Na	137
7	Calcium	Ca	2.5
8	Bicarbonate	HCO_3	23
9	Glucose	Glu	5.1
10	Potassium	K	4.9
11	Magnesium	Mg	0.8
12	Lactate	Lac	1.77
13	Amino acid	AmAc	0.49
14	Uric Acid	UrAc	0.38
15	Urea	Ur	2.33
16	Phosphate	PO	0.26
17	Hydrogen	H	3.98×10^{-5}

Table 3: Main constituent in blood accounted in this study and their concentrations. The unit is $nmol/mm^3$

Table 1 in [119] and Tables 2 and 4 in [120]), however we only tabulated the 17 main ones in Table 3).

Dimensions

Length of the cylindrical compartments were chosen to be at a constant value, 5 mm. This value was estimated based on the length of cerebral microvessels [163]. We assumed the change in the cross-sectional area results from the flaccid characteristics of the compartments rather than them stretching.

Voetmann (1949) found the capillaries of the choroid plexus Stroma to be considerably larger in diameter than capillaries found elsewhere in the body ($15 \mu m$ as compared to $3 \mu m$) [102, 117, 125].

The corresponding value in the Stroma, to the best of my knowledge, is not reported in the literature; therefore, we make a loose estimate based on the microscopic pictures provided for the choroid plexus (Figure 5 in [52]) and estimate the thickness to be equivalent to one a size of one epithelial cell. A large volume of studies suggests the cells to have

Parameter	location	value
R_o (mm)	EC	7.5×10^{-3}
	BLM	17.5×10^{-3}
	APM	27.5×10^{-3}
	Vent	177×10^{-3}
θ_o (mm)	EC	3×10^{-4}
	BLM	7.6×10^{-6}
	APM	7.6×10^{-6}

Table 4: Resting radius and thickness of membranes (R_o, θ_o), ABV. EC:endothelial cells, BLM: Basolateral membrane, APM: apical membrane, Vent: ventricles.

simple cuboidal shape at approximately $10\mu m$ in height [137, 7].

Finally, although we do not fully model the ventricular system, but we have assumed an enclosed ventricle. Hence, we need to pre-define the radius of ventricle. We chose the boundary for ventricle significantly larger than the CP to minimise its impact on other variables and mimic a real condition, i.e. 150 times larger than APM.

Reflection coefficient

The reflection coefficient (σ) is a dimensionless constant representing the amount of solute that will pass through a membrane, which adopts a value ranging between 0 and 1. In most similar conducted studies, the variable is assumed to be 0 across endothelial cells, as the pore fenestrations were assumed considerably larger than solutes radius's. i.e. ranging between 300-500 A in diameter [114]. Since these pores are large in comparison to solutes that naturally exist in the blood (e.g. one of the largest being Fibrinogen with maximum length of 216 A), there has been a general misconception in literature that these fenestrated endothelial cells provide little to no resistance to the solutes [18, 28, 52, 110]; therefore, allowing the solutes to freely cross the membrane. However, these studies did not account for the other two membranes that cover the endothelial cell membranes (i.e. basement membrane and diaphragm) [68, 121, 123]. Histological studies on endothelial membranes reveal that these ECs are bounded from the outside by a layer of continuous

membranes (i.e. basement membrane) and from the inside by a layer of fenestrated diaphragm, both of which may impose resistance to solute exchange [68, 121, 123, 120, 6]. In addition, as mentioned earlier, the fenestrations are not uniform in size and their frequency; the numbers of smallest to largest pores in cat stomach is 2600/1, in cat intestine is 6400/1, in dog colon is 550/1, with occupied areas of 92/1, 340/1, and 48/1, respectively [76]. Therefore, we challenged the argument and adopted a new evaluation approach by computing the values for each solute. This value depends on solute and pore radius (i.e. a and R) [5, 101, 128] as,

$$\sigma = \left(1 - \left(1 - \frac{a}{R}\right)^2\right)^2$$

Considering the above argument, we estimate the average effective pore radius in plexus capillary to be approximately 30% of the average endothelial reported pore size (i.e. 200A).

This formulation above was also used to find the reflection coefficients across the tight junction. CLDN-2 forms a narrow pathway of 0.65 nm to 0.75 nm that acts as a charge and size selective pore for solutes and water, i.e. cations and water can flow through them [52]. Note that at this stage, we neglect the electrical charge of ions, but implicitly we have accounted for the effect. Therefore, we compute for reflection coefficient of cations (i.e. Na, Ca, K, and Mg) across TJ, and the rest take values of 1.

Since the solutes transport across BLM and APM require special transporters to transport proteins and do not have the ability to pass the solutes across without them, the reflection coefficient can be assumed as 1.

Hydraulic conductivity

There is a great body of research pointing at the resemblance between choroid plexus and proximal tubule in kidney [28, 52]. A study investigating the mathematical modelling of proximal tube absorption suggest that the hydraulic conductivity of endothelial cells is 2 times larger than this variable on the basal membrane [56]. Therefore, we use twice the value of L_p across BLM. This value reads well in the range for the associated data found elsewhere [55].

i	Symbol	σ_{EC}	σ_{TJ}
1	Alb	1	1
2	Glo	1	1
3	Fib	1	1
4	Cl	0.003	1
5	Chol	0.0028	1
6	Na	0.001	0.3
7	Ca	0.005	0.9
8	HCO_3	0.004	1
9	Glu	0.013	1
10	K	0.002	0.5
11	Mg	0.003	0.6
12	Lac	0.005	1
13	AAmAc	0.048	1
14	UrAc	0.0.01	1
15	Ur	0.007	1
16	PO	0.009	1
17	H	0.0003	0.1

Table 5: Calculated reflection coefficient of each solutes across EC: endothelial cells and TJ:tight junctions.

On the other hand, to estimate the required data, we studied different epithelial cells to find the most resembling one to the CPE [56, 132, 157, 35, 34, 78]. Among the cited references, we choose hydraulic conductivity of retinal pigment epithelium (RPE) as a base data upon: 1) both (RPE and CPE) have similar epithelial cell types (i.e. simple cuboidal epithelium), 2) the size of both epithelial cells is similar (i.e. $10\mu m$ lengths in each side) [158, 7], 3) the Lp value was for RPE in that study was chosen at temperature 37 degree Celsius (i.e. human body temp). This value reads as $3.8 \times 10^{-9} cms/Pa$.

In addition, it is evident that AQP1, which is responsible for transcelular water transport is more abundant in APM of choroid plexus epithelium than BLM [28, 51, 102]; therefore, the hydraulic conductivity could be assumed larger across APM than BLM. A similar justification is made for the Lp across APM of RPE, therefore we use a 10-fold of the value assigned for hydraulic conductivity across the BLM as our required Lp on APM membranes. A similar approach is taken in [35, 34, 56].

Dankier et.al reports that the area of tight junction is 10^{-4} times of the apical membrane [28]. Hence, we utilise this data and adjust for the corresponding value at tight junction.

Parameter	location	value
Lp $(\frac{mm}{s.kPa})$	EC	2.56×10^{-6}
	BLM	1.28×10^{-6}
	APM	1.28×10^{-5}
	TJ	1.28×10^{-7}

Table 6: Hydraulic conductivity of each membrane, ABV. EC:endothelial cells, BLM: Basolateral membrane, APM: apical membrane, Vent: ventricles.

Diffusion coefficient

The solute permeability refers to the ease with which the solutes can cross a membrane; it describes the diffusion of particles through membranes. According to the Stokes-Einstein relation for diffusion of spherical particles in low Reynolds number is defined by

$$D = \frac{KT}{6\eta\pi r}$$

where K is the Boltzmann constant, η is the dynamic viscosity, T is the temperature, and r is the radius. It can be seen that the permeation of the solutes is inversely proportional to the radius; hence, we take advantages of the relationship between the permeability coefficient of one solute and the radius for each solute, in order to estimate all the permeability coefficients (i.e. $\frac{D_{ii}}{D_i} = \frac{r_i}{r_{ii}}$).

The following step is to obtain a value for permeability coefficient of one solute across the fenestrated membrane. Note that there are far fewer investigations in permeability across fenestrated capillaries in comparison to the continuous type as these membranes have been considered to impose no or little restriction in solute transport. Hence, we utilise both sets of parameters found from fenestrated and continuous endothelial cells to acquire the required value. We investigated the different solute permeability across fenestrated capillaries, from where we found the albumin transfer across dog intestine (i.e. fenestrated EC) to be $2.9 \times 10^{-8} \text{ cm/s}$ [3] and a similar value reads in dog heart muscle (i.e. continuous type) as well as in other mammalian heart muscles [128]; hence, we take

$D = 2.9 \times 10^{-8} \text{ cm/s}$ as a reasonable choice for albumin transfer across a fenestrated EC. Taking advantages of the relation between radius and permeability, we estimate all other values.

As it can be seen in the model, there are Cl and K channels located on the apical membranes. In order to mimic these pathways, we require to estimate the permeability coefficients across these membranes. [35] provides the permeability values of chloride and potassium across the basal membrane of RPE to be $1.24 \times 10^{-6} \text{ cm/s}$ and $3.16 \times 10^{-6} \text{ cm/s}$, as well as the potassium permeability across the apical membrane (i.e. $2.23 \times 10^{-5} \text{ cm/s}$). As it has been mentioned earlier, it is suggested that the permeability of APM to solutes is a factor of 10 in comparison to their permeability across BLM. Hence, we take this value of Cl on BLM and multiply by 10. Note that a similar pattern exists for K permeability across BLM and APM (i.e. $3.16 \times 10^{-6} \text{ cm/s}$ and $2.23 \times 10^{-5} \text{ cm/s}$).

In order to define the permeability constants for the aforementioned solutes (i.e. Na, Ca, K, and Mg) across the TJs, we adopt a similar approach as determining the permeability constants across endothelial cells (i.e. $\frac{D_{ii}}{D_i} = \frac{r_i}{r_{ii}}$). As it has been discussed earlier, the transport across CPE resembles the transport across the renal proximal tubule. Therefore, we use the permeability coefficient of sodium across the TJs (i.e. $2.41 \times 10^{-6} \text{ cm/s}$, provided in [157]) to determine the rest of the permeability coefficients.

Transporters coefficient

Finally, we describe the choice for transporter coefficients as well as dissociations constant for transporters involving ATP, NKCC1, KCC4, NBCe2, NCBe, and AE2. To best of my knowledge, there has never been a study reporting these values on the CPE membranes. Also, there are very limited studies reporting these values on other epithelial membranes[35, 158, 157]. Therefore, to acquire the relevant data, we make use of the average values from different sources. In addition, the dissociation constants are directly taken from the resources in [162, 132, 134, 148, 157, 35]. However, these constant values for NCBE and NBCe2 were not found in the sources, hence we just made a loose estimate based on other transporters coefficients. The values for membrane potential (ΔE) was chosen to be 60mV, a value well within the range outlined for the mammalian choroid plexus [28].

i	Symbol	$D_{EC} \times 10^{-7}$	$D_{TJ} \times 10^{-3}$	$D_{Ch} \times 10^{-4}$
1	Alb	2.9	0	0
2	Glo	1.22	0	0
3	Fib	0.956	0	0
4	Cl	31.2	0	0.14
5	Chol	19.7	0	0
6	Na	29	2.4	0
7	Ca	25.3	2.09	0
8	HCO_3	29	0	0
9	Glu	28.8	0	0
10	K	31.3	2.59	0.3
11	Mg	24.8	2.045	0
12	Lac	45.13	0	0
13	AAmAc	14.8	0	0
14	UrAc	32.4	0	0
15	Ur	39.9	0	0
16	PO	34.6	0	0
17	H	173	14	0

Table 7: Calculated diffusivity constants across interfaces, EC: endothelial cells, TJ: tight junction, Ch: channel.

Elastic constants

It is known that the stiffer a material is, the higher the elasticity constant for that material will be. In the case of endothelial cells, the Youngs modulus E is suggested to be 4 KPa, close to the range found in cultured Schlemms canal endothelial cells [165]. At this phase of the study, we choose the elasticity coefficients for basal and apical membranes to have the same value. Since retina epithelium and CPE both have simple cuboidal epithelium and having similar size, we take the elasticity constant of RPE for our model ($E=2$ KPa). These values for St and CPE were taken to be 10 and 20 KPa, respectively [66, 163, 165, 49].

In the model, we have two additional parameters related to this properties that must be defined: Poisson ratio ν , and Shear modulus G . ν is taken as 0.5 as a widely acceptable value for an incompressible biological membrane [66] and $G = \frac{E}{2*(1+\nu)}$.

Membrane	Transporter	M $\frac{nmol}{s.mm^2}$	ion	K mM
BLM	KCC3	1.5×10^{-2}	Cl	5
			K	5
	NBCn1	1.5×10^{-2}	Na	500
			HCO3	30
	NCBE	2.7×10^{-3}	Na	50
			HCO3	3
			Cl	30
	AE	9.6×10^{-2}	HCO3	1
Cl			10	
APM	Na-K-ATP	1.48×10^{-2}	Na	5
			K	5
	KCC4	1.5×10^{-2}	Na	500
			HCO3	30
	NKCC1	2.7×10^{-3}	Na	50
			HCO3	3
			Cl	30
	NBCe2	9.6×10^{-2}	HCO3	1
			Cl	10
	NHE	9.6×10^{-2}	HCO3	1
Cl			10	

Table 8: transporter coefficients (M) and dissociated coefficients (K).

Additional constants

There are some parameters specifically related to the Stroma that must be defined. As mentioned in previous sections, Stroma in choroid plexus is the most overlooked and understudied area in CP and there is not much information on this organ. It is mostly referred to as highly vascular loose connective tissues [28, 52, 102, 140, 51]. The most similar tissue to Stroma, that I encounter in human body, is the Pia Mater [153]. These data are provided in Table below.

In equations modelling CPE, there are two constants which are defined as $\eta = 9.7 \times 10^{-7}$ $KPa.s$ and $M = 1.8 \times 10^{-5}$ $mm^3/nmol$.

Parameter	location	units
S	0.1	KPa^{-1}
α	1	
μ	0.65×10^{-6}	$KPa.s$
k	3×10^{-9}	mm^2
ρ	1×10^{-6}	kg/mm^3

Table 9: S : storage coefficient, α : Biot-Willis coefficient, μ : dynamic viscosity of water, k : permeability coefficient, and ρ : density of water.

4.3 Validation, Verification, and Results

Our aim in this study is to develop and establish a new holistic mathematical model of the mechanics of choroid plexus (CP), including CSF production, capable to provide new insight on its behaviour and predict its response in abnormal conditions. The choice of parameters has been explained and justified in the previous section. Here and in this section, we attempt to validate the model by assessing its behaviour despite limited information that exist in the literature. Although the real phenomenon is transient, literature provides a mean value of some properties; hence we ran the model in steady state and compared the solutions with the literature. Nevertheless, to fulfil the original aim of this research we simulated the transient model and report the outcome in the following section.

One novelty of this model is its capability to provide information on all variables of interest (e.g. Q, J, C, P) not only as an average value, but also their systemic variations with a heartbeat. i.e. over one cardiac cycle. This data has particular importance since it reveals invaluable information and insight on the dynamic of the system in various conditions. i.e. healthy, aged, diseased, and post-treatment. Such detail is difficult to be acquired clinically since cranium imposes a challenge to measure and examine the pulsatility of the organs inside the brain. Note that as a limitation of this study, we do not account for the ionic charge nor the chemical reactions of the solutes existing in the system; hence, notation of the ions will appear without their ionic charge. i.e. Na+ is shown as Na.

4.3.1 Concentration of solutes

In this model, pores forming fenestrations on EC membrane as well as the membrane proteins restrict movements of solutes across the tissue. This characteristic of EC and the poroelastic nature of Stroma do not allow for the instantaneous solute flux across the system into the CSF system; a misconception that is widely discussed in literature [110]. In general, among those 17 solutes reported in Table 3 and considered in this study, Na, K, Ca, Mg, Cl and HCO₃ can reach the ventricle. Regulation of these ions plays a vital role in brain homeostasis, i.e. sodium regulates cell and intravascular volume [38].

Concentration of freshly produced CSF compositions have been reported by a variety of experimental works in literature [28, 52]. CSF have higher concentration of Na, Cl, and Mg compared to blood while the concentration of K, HCO₃ and Ca are lower. This observation is qualitatively and quantitatively validated in our model and reported in Figure 23. i.e. the concentration of Ca is 2.5 mM in blood and decreases to 2.4 Mm in CSF, and the Mg concentration increases from 0.8 mM in blood to 2.1 mM in CSF [17]. In addition, studies report that the most prominent ions being able to pass the membranes of CPE are Na, K, Cl, and HCO₃ [28, 52]; the intercellular concentrations of Na and Cl are less than blood and CSF, whereas K concentration is larger than the surrounding and HCO₃ does not seem to differ at all. The model prediction on the intercellular concentrations is consistent with the trend discussed in the literature [28, 52].

To elaborate further, sodium concentration in blood, that is an inlet condition in our model, increases to 139 Mm in Stroma, decreases to 51 Mm in CPE, and increases back to 139 mM in CSF. Consequently, the prediction for chloride concentration is found to be significantly lower in CPE than blood and CSF; a view consistent with the literature [28, 52]. However, the value found in CPE is 40 mM, whereas literature reports 65 mM. Potassium concentration is 4.9 mM in blood compartment of our model, which decreases to 4.6 mM in Stroma, and increases to 22 mM in CPE, and finally decreases back to 4.2 mM in ventricle. The experimental studies however, report the potassium concentrations to be 100 mM and 3.3 mM in CPE and CSF respectively [17, 28, 52].

	[Na]	[Cl]	[K]	[HCO ₃]	[Ca]	[Mg]
<i>Vent</i>	139	124	4.2	18	2.4	2.17
	140-150	124	3.3	22	2.4	2.17
<i>CPE</i>	51	40	22	26	N/A	N/A
	50	65	100	21		
<i>St</i>	139	83	4.6	43	2.4	2.17
<i>Cap</i>	137	101	4.9	23	2.5	0.8

Figure 23: Concentration of sodium (Na), potassium (K), bicarbonate (HCO₃), calcium (Ca), and magnesium (Mg) in blood (Cap), Stroma (St), Choroid plexus epithelium (CPE), and ventricle (vent). The concentration values shown in blue are the inlet condition, the black ones are obtained from the model, and the red ones are found from literature [28]. Unit: milimollar (mM).

4.3.2 Solute flux

Normal functioning of the CPE transporters plays a vital role in development and maintenance of the central nervous system homeostasis by sustaining the concentration gradient. In the dynamic model, we account for all the transporters located on the epithelial cells, as justified in the last chapter. To recap, there are four transporters on the basal membrane and seven on the apical membrane. In literature, to the best of my knowledge, there is no quantitative value that represents the magnitude of solute flux by each transporter. However, the direction by which they transport solutes are reported; this information is utilised as a qualitative validation. Note that the equations modelling co-transporters are pre-set and formulated in a manner that all transport each solute from the inner compartment to the outer one (Stroma to epithelial cells and from epithelial cells to the ventricle, refer to solute flux equations for KCC3, NBCn1, KCC4, NKCC1, and NBCe2). However, we allow the system to solve and set for the direction. Our findings predicted the direction of all co-transporters, except one, to be similar to the reported ones in the literature: On BLM, the NBCn1 net transport is positive (St to CPE), and for KCC3

is reversed direction (CPE to St). For transporters on APM, the model predicts NKCC has an inward direction (vent to CPE) and KCC4 transports the solutes outward (CPE to vent). However, we observe an inward transport from NBCe2 transports which contradicts the literature [28].

Another unique character of the choroid plexus epithelial cells is their arrangement next to each other. The junction that holds neighbouring epithelial cells are relatively larger than the ones found elsewhere in the brain. i.e. the largest barrier among the four that exist in brain. Among the reported solutes, K and Na can pass this junction. It has been proposed that the paracellular solute transport of potassium occurs from blood to CSF whereas Na transport takes place in the opposite direction [28]. Our model confirms such findings. Further analysis shows that the Na flux across APM into CSF system is approximately 7% larger than the magnitude of flux across TJ. Subsequently, the net flux of K across APM is inward at the same efflux across TJ.

The model also reveals information regarding the transporters and their contribution in balancing the concentration in each compartment. Na-K-ATPase, or sometimes referred to as sodium pump, has a prominent role in regulating the concentration of sodium in the CPE. We reduced the activity of ATP by 35%, and found that the intercellular concentration of Na increases from 50 to 68mM. A condition that leads to cell lysis (death). However, the intercellular concentration of potassium remained unaffected.

In addition, it has been reported that the CSF concentrations of K and HCO₃ remain constant when the corresponding concentrations in blood are experimentally manipulated [28, 136]. Hence, we varied the concentration of the two ions in the system within appropriate physiological range and examined the concentrations in the CSF. Normal potassium concentration in blood in original simulation is set at 4.9 mM; we examined the extreme values of 2 and 6 mM and repeated the simulation. Findings show that concentration at CSF remain at 4.2 mM in both cases. Similarly, the concentration of bicarbonate in original model was set as 23 mM. The extreme cases of 13 and 33 mM did not change the corresponding concentration at CSF. We take this analysis as a verification for the transporters activity that exist in the model. i.e. the transporters activity alters to maintain the composition of the solutes in the CSF. For instance, increasing HCO₃ by 10mM lead to NBCE2 transporter to increase its flux by 80%.

4.3.3 Pressure distribution in compartments

Utilising the non-linear and dynamic model, we present the pressure distributions in each compartment of choroid Plexus . i.e. capillary, poroelastic Stroma, viscoelastic epithelial cell (Figure 24). Characterisation of the variable (i.e. pressure) in each compartment provides local information (e.g. average pressure, pulsatility nature, etc). Each signal is composed of average value and pulsating waveform; for the sake of simplicity, we discuss them separately. The mean pressure in capillary, Stroma, and CPE are 3.6, 2.4, and 1.8, and 1.2 KPa. The dynamic pressure signal for the capillary, which is an input to the model, have a maximum at the first half of the cardiac cycle followed by a small peak. Stroma and CPE show a similar characteristic; however, the extremums are significantly attenuated.

Pulse pressure is an informative parameter that assess intracranial health and it is measured as the absolute pulse amplitude, which is the min to max variation in pressure signal. The pulse pressure in the system is highest in capillary at 1.2 KPa, whereas in the other compartments the corresponding value is approximately 0.25- 0.3 KPa.

In order to compare the results with an abnormal case, we rerun the simulation in for a

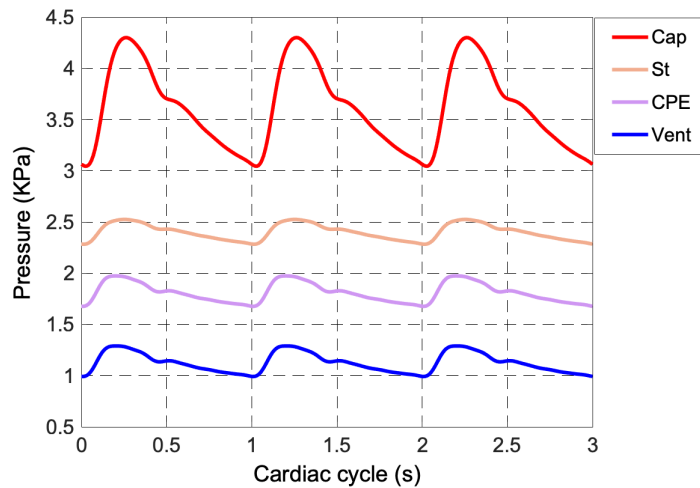


Figure 24: The pressure waveforms in different compartments in choroid plexus, capillary (Cap), Stroma (St), choroid plexus epithelium (CPE), and Ventricle (vent).

case where the endothelial cells thickens. This condition is repeatedly reported for various conditions such as ageing [135, 126]. Figure 25 depicts the pressure trajectories in the Stroma and CPE from the case where the thickness is $3 \times 10^{-4} \text{ mm}$ (normal condition)

to $3 \times 10^{-3} \text{ mm}$ (thickened) case for 350 hours. It can be seen that, this condition has a great impact on the pressure inside the Stroma whereas the CPE is less affected. i.e. the mean pressure in Stroma increases to 3.07 KPa, a 27% increase relative to the normal case., whereas the corresponding variable increases by 9% in CPE. In addition, the pulse pressure in Stroma increases by 16% in thickened EC case, while this value remains unaffected in CPE. These result highlight the importance of Stroma, and their dynamical change when the system undergoes alterations.

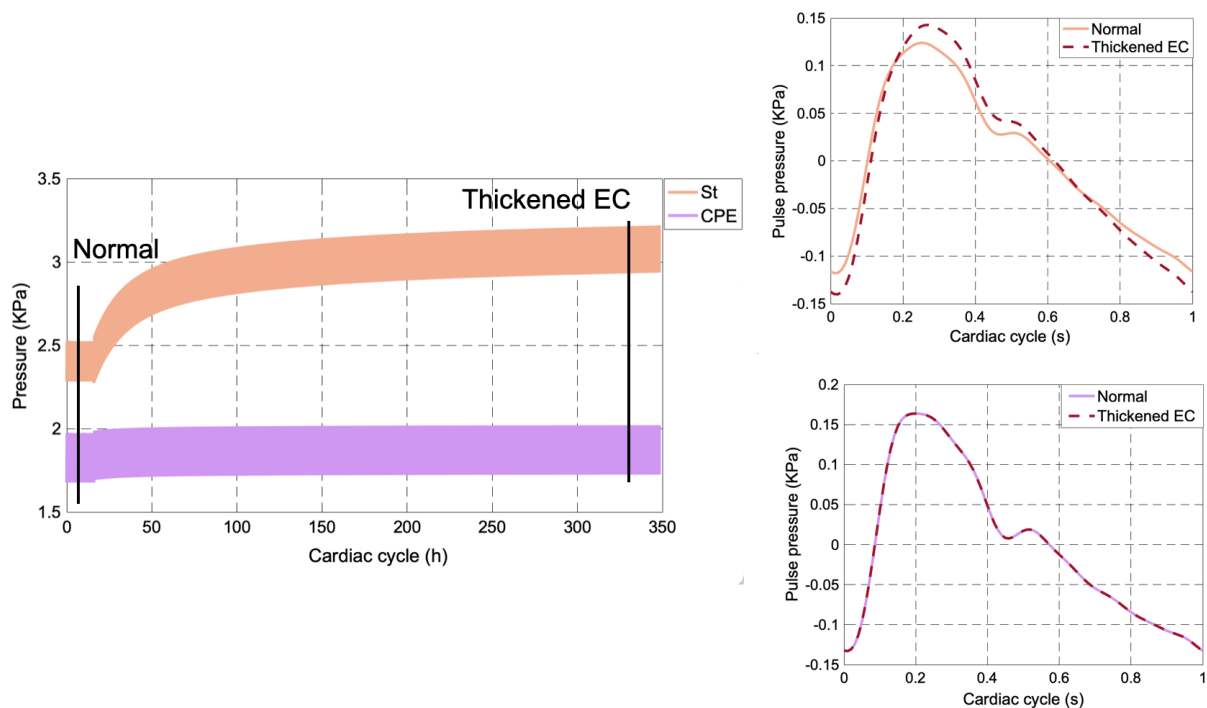


Figure 25: Predicted pressure in Stroma (St) and choroid plexus epithelium (CPE). The figure on the left shows the evolution of pressure from a normal case to an abnormal case of thickened endothelial cells. Right figures show the steady state solutions of pressures for one cardiac cycle in normal vs abnormal case.

4.3.4 Water seepage

There have been attempts to determine water production by CP using implicit and inaccurate observation [111]. One clinical approach has been to take the CSF net flow across the aqueduct over one cardiac cycle as a measure for CSF flux CP [138]. However, this reasoning is unacceptable since there is a speculation about the contribution of choroidal

and extra choroidal sources of CSF production, which cannot be isolated and tested separately.

However, modelling provides an opportunity to examine water transport produced solely by CP. As explained in the previous chapter, water transport across interfaces is modelled by Starling law, which is a balance between hydrostatic and osmotic pressure gradient across membranes. It is worth noting that the flow flux due to hydrostatic pressure takes place from the compartment having higher to lower pressure, whereas the direction of the flow flux due to osmotic pressure difference takes place from the compartment with lower to higher pressure.

Our model predicts the hydrostatic versus osmotic pressure gradient, exerted to EC and BLM membranes, are the same order of magnitude, but not across APM and TJ. i.e. the hydrostatic pressure gradient across APM and TJ are 95 and 85% higher in magnitude relative to the osmotic pressure (Table 10). Across all membranes, both the hydrostatic and osmotic pressures drive the flow outward. In other words, across each membrane, the lower compartment exerts higher hydrostatic pressure to the membrane than the adjacent upper compartment; hence water flows outside. Simultaneously, the upper compartment imposes higher osmotic pressure to the membrane than the lower and leads to water efflux. The latter explains the negative signs in Table. Figure (27a) depicts total water flux

	EC	BLM	APM	TJ
Hydrostatic pressure	0.2	0.6	0.68	1.27
Osmotic pressure	-0.5	-0.4	-0.02	-0.2

Table 10: Hydrostatic pressure and osmotic pressure across EC: Endothelial cells, BLM:basolateral membrane, APM: apical membrane, TJ: tight junction. The units are KPa.

across all membranes; the mean water flux across EC, BLM, APM and TJ are 3.8×10^{-7} , 2.3×10^{-7} , 2.3×10^{-7} , and $1.5 \times 10^{-7} \frac{mm^3}{s}$, respectively. Subtracting the mean value provides us with the pulsation. Figure (27b) depicts the water flux pulse across the membranes; the pulsatility is highest across EC and BLM, whereas APM and TJ experiences the least pulse. Pulsatility index (PI) is another dimensionless flow parameter with a broad range

of both, research and clinical applications. The parameter is defined as,

$$PI = \frac{\max(Q) - \min(Q)}{\text{mean}(Q)}$$

Our analysis predicts the PI across interfaces of EC, BLM, TJ, and APM to be 0.12, 0.26, 0.05, and 0.05, respectively. In the following chapter we discuss this parameter further.

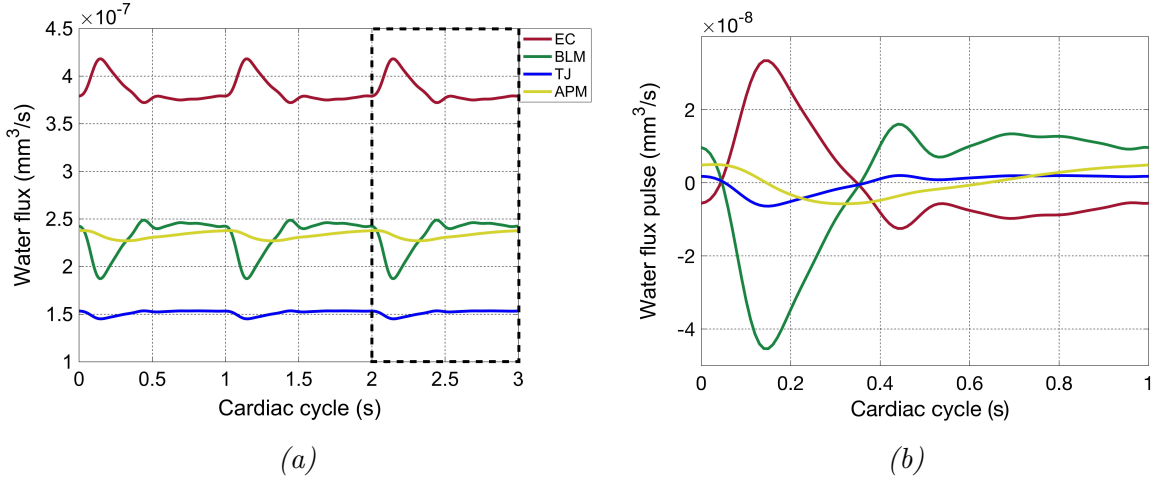


Figure 26: (a) Total water flux for 3 seconds & (b) CSF pulses for 1 second across endothelial cells (EC), Basolateral membrane (BLM), apical membrane (APM), and tight junction (TJ)

4.3.5 Origin of CSF pulsation at CP

The model enables us to examine the two proposed origins of CSF pulsation: volumetric expansion of CP versus pulsation induced by CSF production. In this model, the CSF production is the summation of water flux across TJ and APM. In addition, the expansion of CP is found from the volumetric change of the outer layer in the model, i.e. APM. The model predicts the average CSF production and the volumetric expansion of CP are $3.8 \times 10^{-7} \text{ mm}^3/\text{s}$ and $4.5 \times 10^{-7} \text{ mm}^3/\text{s}$, respectively. This analysis does not provide us with enough information to compare the sources, since both have almost similar values. However, a more detailed analysis on their pulsating components will address us further (Figure 27): the displacement of choroid plexus is about four orders of magnitude larger than the pulse that CSF flux inserts. (CSF flux pulse= $1.5 \times 10^{-8} \text{ mm}^3/\text{s}$, CP volumetric

expansion= $2.5 \times 10^{-4} \text{ mm}^3/\text{s}$). Therefore, the source for pulsation originated at CP is perhaps by change in volume of CP, rather than CSF production.

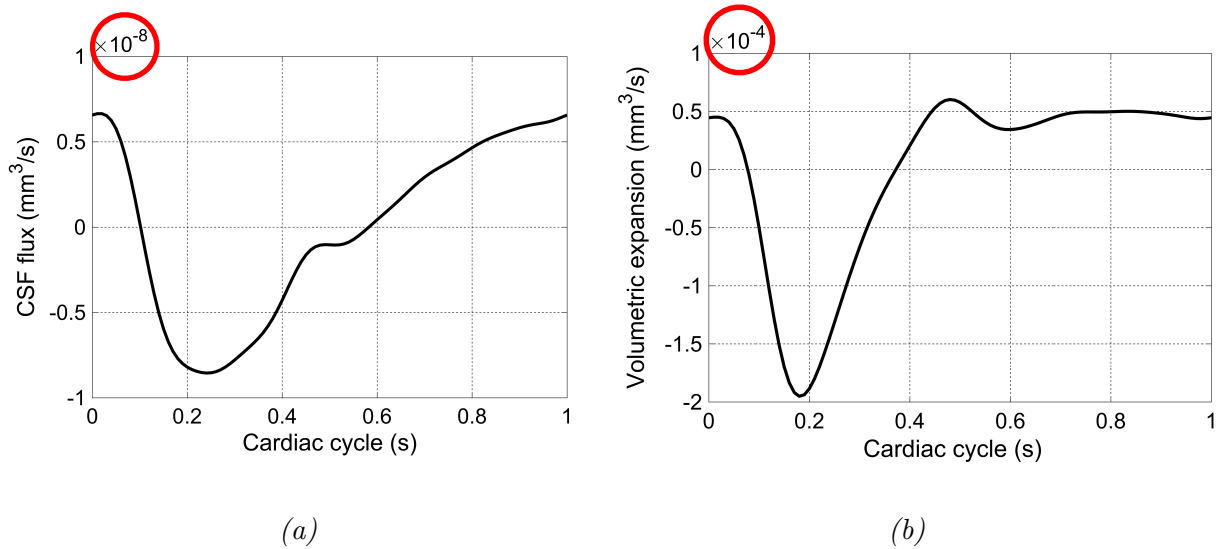


Figure 27: Compare the two proposed sources of pulsation from choroid plexus. (a) CSF production pulsation & (b) volumetric expansion pulsation. The latter is four orders of magnitude larger than the former, hence more likely to be pulsating source.

4.4 Chapter summary & future work

The first mathematical model representing the mechanics of choroid plexus is developed. The system includes all three main compartments present in a real choroid plexus, i.e. capillary, Stroma, and epithelial cells. The interfaces between each compartments have also been accounted for, i.e. endothelial cells (EC), basolateral membrane (BLM), apical membrane (APM), and tight junction (Tj). For each compartment, we formulate mass conservations of water and solute as well as the momentum conservation for water. The transport across the interfaces is facilitated by either advection-diffusion mechanism or via active and passive transporters located on the basolateral and apical membranes of CPE. In total 171 equations were derived and have been solved numerically by MATLAB. The variables that we solve for are of seven types: water flux (Q), solute flux (J), Pressure (P), Concentration (C), cross section and surface areas (A and B), as well as the radius for each compartment (r).

One reason for developing such holistic mathematical model is to provide a framework that clarifies the behaviour of the system in health, provides insights about the poorly understood mechanisms, and examine the assumptions that have been made in clinical and experimental work.

In this model, it is predicted that solute transport across endothelial cells (EC) is not as free as previously described in literature. Specifically, there are notable differences in the concentrations of solutes in the blood and Stroma. This observation has important implications for the analysis of osmotic pressure and its effects on water flux across the system, which will be further discussed in the next chapter.

While the developed model has shown promise in predicting the dynamics of CSF production in the choroid plexus, further validation is necessary to ensure its accuracy and reliability. This entails comparing the model's predictions with further experimental and clinical measurements, such as conducting more detailed techniques, including microdialysis, electrophysiology, molecular biology, histology, and in vivo studies. These techniques could be used to compare the model's predictions with further experimental measurements, helping to assess the model's accuracy and reliability.

In addition, the model's validity can be further established through sensitivity analy-

ses, which identify and quantify sources of uncertainty and potential limitations in the model. With approximately 180 pre-defined parameters in the system, a sensitivity analysis study would increase understanding of the relationships between input and output variables and test the model's robustness. Alternatively, experts in the field can conduct peer-review of the model to evaluate its assumptions, methodology, and findings, which can help identify any weaknesses or limitations and suggest improvements to enhance its validity.

The developed model can be used to create maps of solute perfusion across the choroid plexus as a function of CP/blood properties. Since the system is highly interconnected and various parameters can influence each other (e.g., pressure, flow flux, concentration, etc.), the developed model is capable of exploring the impact of multiple variables on each other.

As a fundamental model, there are numerous opportunities for improvement. Currently, the model is developed for a single unit of the choroid plexus. However, the choroid plexus consists of an unknown number of strands, which appear to be connected to one another in parallel forms. Since this information is not reported in the literature, further studies are necessary to extend the model to a macroscopic level that appropriately reflects the complexity of the system.

In addition, the model does not incorporate the influence of electrochemical processes, which have a significant impact on the transport of solutes throughout the system, leading to changes in osmotic pressure and water flow. Specifically, the direction and rate of water and solute transport depend on both the concentration gradient and the electrical potential difference across the cell membrane. It is our conjecture that the absence of such electrochemical considerations may have contributed to the incomplete validation of intercellular ion concentration. Therefore, future work should focus on integrating electrochemical factors into the model to improve its accuracy and predictive power.

5 Role of Choroid Plexus in Ageing Brain and Development of Neurological Disorders

5.1 Introduction

In recent years, it has become clear that malfunction of CP is a major contributor factor in the development and progression of various neurodegenerative diseases and autoimmune disorders [60, 113, 74]. One example is Alzheimer's disease (AD) that is associated with morphological and physiological changes in the CP [74]. The biomarker for this disease is amyloid beta ($A\beta$); a fragment of a molecule that is naturally produced by brain neurones and blood cells. Under normal conditions, the choroid plexus clears this protein from the CNS via two proposed routes. First, $A\beta$ enters choroidal capillaries and is transported to the ventricular system, follows the pathways towards the arachnoid granulations located on the subarachnoid spaces and is absorbed to the venous blood stream. i.e. similar to the route that CSF takes. The second mechanism involves uptake via choroid plexus, i.e. the $A\beta$ in the CSF reaches the choroid plexus, enters the CPE and Stroma, and absorbs to the blood stream [9]. However, it has been postulated that CP loses its ability to remove the protein in abnormal conditions resulting in the accumulation and deposition of $A\beta$ in brain tissue (more specifically along the subventricular zone) and inside subsystem of CP (e.g. choroidal capillary), which is a neuropathological hallmark of AD [74].

Another example is multiple sclerosis (MS), which is the second cause of neurological disability in developed countries [93]. The disease is characterised by inflammatory damage to the brain tissue accompanied by increase in T cell. Under normal conditions, T cells are a part of immune cells that are found to cross CP into the CSF system [94]. However, recent studies suggest that disruption in CP structure and integrity may amplify the existence of T cells in the CSF and target the periventricular brain tissue and cause inflammatory damage [139, 45].

In both aforementioned neurological conditions and others such as Parkinson's disease and Hydrocephalus, the exact aetiologies are unknown. However, there is a significant body of new research emphasising on the possible contribution of CP in the onset and

progression of these abnormal conditions [60, 113, 74, 139, 45, 93].

Recently, advances in imaging techniques have enabled clinicians to detect the CP changes in abnormal conditions. i.e. swollen CP, deposition of solutes (e.g. T cell, $A\beta$, iron) in vessels, stroma, and epithelial cells [54, 23]. These investigations have shed lights on the overall behaviour of this tissue, however the information they provide is limited. One reason is that the tissue is very small and difficult to detect with high resolution imaging tools. Another reason is its deep location inside the brain which makes it hardly accessible. In addition, these studies can detect CP in health and in diseased states; a time by which the irreversible damages took place to the brain and does not cover the transition period during which disease is initiated and is being developed.

Although the exact underlying mechanisms for the conditions remain unknown, but thickened and stiffened endothelial cells, fibrosis within the Stroma, structural changes in epithelial cells and altered CSF production have been repeatedly observed [60, 9, 54, 93]. So far, there has never been a study to examine the effect of these pathophysiological changes on the dynamic of CP. In the previous chapter we developed a model for CP incorporating all the important tissues and elements. The model does not only enable us to analyse the overall behaviour of tissue under various conditions, but also provides us with detailed information that is impossible to obtain with any other technique. For instance, we can analyse the reaction of each compartment separately rather than obtaining a holistic behaviour of the system. Such investigation is necessary to correct the existing misconceptions around the tissue and its mechanics. One example is neglecting the Stroma that to the best of my knowledge has never been investigated. Secondly it can differentiate the impact on individual compartments; this will provide insights about the main locations being affected the most, hence one step closer to finding the aetiology of certain conditions. In this chapter we conduct a detailed examination of some pathophysiological impact on the tissue and its association with neurological conditions. It is worth noting that these pathophysiological conditions are also commonly observed in normal ageing [60].

Therefore, we examine the impact of ageing brain (more specifically ageing choroid plexus) on the mechanics of Choroid plexus and its possible contribution to development of neurological conditions. One reason for our interest in healthy ageing is that according to

WHO, the pace of population ageing is faster than the ever before and the world's population over 60 year will double between 2015 & 2050, [112]. Therefore, it is expected that countries will face major challenges to ensure that their health and social systems are ready to make the most of of this shift; hence, understanding how the brain reacts as it ages is becoming ever more important.

5.2 Methodology

The model, mimicking the mechanics of Choroid plexus, developed in the previous chapter is utilised to assess the effect of physiological and morphological changes in ageing CP and its possible relation to development of abnormal neurological conditions. The model is described in the previous chapter and will not be repeated in this chapter (for more detailed explanation, please refer to Chapter 4). However, for the purpose of conducting the current study, we recap the related parts.

The model is composed of 171 equations and unknown variables which have been solved numerically in MATLAB. The variables that we solve for are of seven types: water flux (Q), solute flux (J), Pressure (P), Concentration (C), cross section and surface areas (A and B), as well as the radius for each compartment (r). The pre-defined parameters used to solve the model are: diffusivity constants (D) and reflection coefficients (σ) for all solutes across interfaces, hydraulic conductivity of each interface (L_p), resting radius for the membranes (R), the thickness of each membrane (θ), Elastic properties for each membrane and compartment (E), transporters coefficients and dissociation constants for each transporter (M and K), and additional Stroma and CPE properties. In general, with ageing some of these parameters that describe properties of the system undergo physiological or structural changes. In the following subsection, we explain which pre-defined parameters were changed to conduct the study.

5.2.1 Ageing of choroid plexus

We conducted literature review to understand the main impact that ageing has on normal choroid plexus anatomy as well as function. Reports of physiological CP ageing repeatedly describe modifications in elastic properties of media (E), water transport properties (L_p),

Parameter	Medium	Magnitude	Comment
Elasticity	EC St CPE	Increase by 3-fold	Endothelial cells, stroma and CPE stiffen. $E_{Ageing} = 3 \times E_{Normal}$
Dehydration	EC BLM APM TJ	Decrease by 1/10	Interfaces loose their ability to transport water efficiently. $LP_{Ageing} = \frac{1}{10} \times LP_{Normal}$
Epithelial Atrophy	CPE	Decrease by 10%	Epithelial cells shrink. $R_{Ageing} = 0.9 \times R_{Normal}$
Transporter activity	ATP NKCC	Decrease by 30%	Enzymes loose their ability to transport solute efficiently. $M_{Ageing} = 0.7 \times M_{Normal}$

Table 11: Pathological changes in choroid plexus in ageing. (ABV. EC: Endothelial cells, St: Stroma, CPE: Choroid plexus epithelium, TJ: Tight junction, ATP & NKCC are two enzymes located on APM). Values are found from [93, 135, 43, 126, 60]

epithelial cell size (R) , and transporters activities (M) [135, 43, 126, 60]. Consequently, we change the associated parameters in the developed model to accommodate for ageing CP. The magnitude of these alterations are estimated based on findings that have been reported in literature and tabulated in Table 11. Please note that, at this stage of the research and for better understanding the system, we perform 10 different simulations, each of which examines the effect of one alteration on the dynamic of the system. The results will be displayed and discussed in the next section.

5.3 Results and discussion

Justified in the previous subsection, we investigate the effect of medium's stiffness, dehydration, epithelial atrophy and two transporter's activities on the dynamics of three variables: CSF production, capillary morphology, and CP volume. The choice of these

variables will be explained and justified under their relevant subsections. Since, each variable has a pulsatile nature, it is composed of two components: mean value and oscillating signal with zero mean. For a better comparison to normal condition, the results are presented and analysed by use of figures, schematic diagrams and tables. In addition, the figures are colour coded. i.e. the results obtained by the change in **EC** will be shown in **dark red**. Consequently, we use **green**, **yellow**, and **blue** to represent changes done to **basolateral membrane (BLM)**, **apical membrane (APM)**, **tight junction (TJ)**, respectively. We also use **light orange** and **purple** for representing the changes applied to **Stroma (St)** and **epithelial cells (CPE)**. Finally, **magenta** and **cyan** will be used to shown results obtained from reduction in **ATP** and **NKCC** activities. We only plot and discuss the variables affected by the pathological alterations; the rest will only be reported in the tables in each subsection.

5.3.1 CSF production

Alteration of CSF production is associated with development and progression of various neurological disorders. In our model the total secretion is a summation of production through apical membrane (APM) and tight junctions (TJ) into the ventricular system. In all scenarios, we report the total production, the flow rate pulsation profile, and the mean production percentage relative to the normal case (Schematic diagram). Overproduction of CSF is linked to hydrocephalus, whereas its underproduction may lead to deposition of solutes in the ventricular system. In addition, the alteration in the Pulsatility index (PI) is used in clinical investigations as an indication for an abnormality or development of an abnormal condition.

As described in the previous chapter, the secretion of CSF is facilitated by starling law, i.e. a balance between hydrostatic and osmotic pressure across the interfaces (i.e. APM: membrane between CPE and ventricle, and TJ: junction between Stroma and ventricles). Therefore, to improve understanding on the dynamics of the system, we analyse the balance in those equations wherever necessary. Under normal condition, as explained in the previous chapter, hydrostatic pressure (HP) and osmotic pressure (OP) differences across each membranes force the fluid out the compartments into the ventricular system. However, pathophysiological conditions may impair the balance and impact not only the

water production, but also impair functions of CP as a system facilitating waste removal or micronutrients secretion.

Another point worth recapping, when referring to tables reporting the hydrostatic and osmotic pressures differences across media, is that the positive HP refers to outflow, since flow takes place from higher pressure location to a lower pressure location. However, the efflux due to OP takes place when the value is negative; this is because water flows from a low OP location to higher.

Effect of elasticity on CSF production

The predicted CSF production into the ventricular system for stiffened EC, St, and CPE are depicted in Figure 28. As it can be seen from Figure 28-right, the total production does not seem to be affected by the endothelial cell stiffening. The relative mean production in comparison to the normal case is decreased by less than 1%, whereas loss of elastic properties in Stroma and CPE have a greater impact on average CSF production. Stiffened Stroma decreases the mean production by 7%, while this production increases in altered CPE by 41%.

In the stiffened EC, the osmotic and hydrostatic pressure across APM remains unchanged compared to the normal case (Table 12), whereas the osmotic pressure across TJ drops by 17% and hydrostatic pressure increases by 20%. Since the production is a balance between the two forces, the osmotic and hydrostatic alterations across TJ compensate for each other; hence, the total production remains unaffected.

In a more rigid Stroma, the osmotic and hydrostatic pressure across the APM does not change, but the corresponding forces across TJ are affected; in stiffened Stroma the OP also causes backflow into the compartment. i.e. the OP that has a negative magnitude (outflow) in normal case becomes positive in stiffened case (Refer to Table 12). Among all analysis conducted, this physiological change in Stroma is the only one having such a unique impact on the flow production. In abnormal condition of less flexible epithelial cells, the changes are significant. Among the three alterations, the latter is the only case where the OP and HP across both APM and TJ are affected; across APM, OP drops by an order of magnitude and HP increases by an order of magnitude. Across TJ, the magnitude for both OP and HP increases by approximately two-fold.

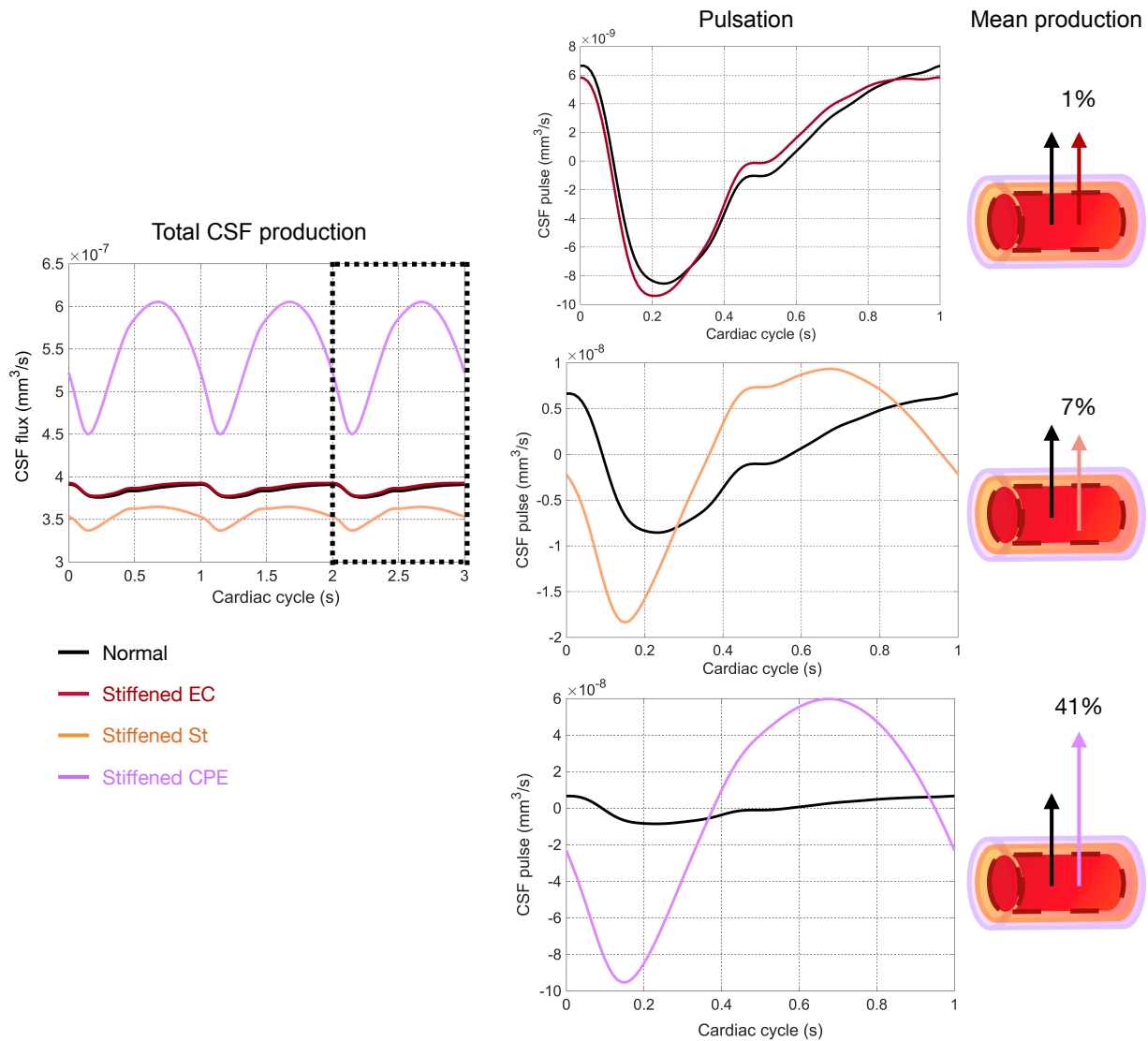


Figure 28: Investigating the effect of media stiffness on CSF production. Left: total CSF production for 3 seconds, middle: CSF pulses for 1 second, right: the schematic diagram of the relative percentage difference of mean CSF production between normal and each abnormal condition.

We postulate that one reason for observing such a significant impact of CPE stiffening on CSF production to be the elasticity modulus that the nominated compartment has. In general, among the three media, CPE has the highest elasticity modulus (i.e. the stiffest among the three) and imposing additional stiffness to the compartment can lead to a drastic alteration in flow production.

Another characteristic of this production is the pulsatile profile. As shown in Figure 28-middle, EC stiffening does not affect the production pulsation, but the changes in the two other cases are more significant. The pulsatility index (PI) for CSF production in

Variable	Q_{PI}	OP_{APM} (KPa)	HP_{APM} (KPa)	OP_{Tj} (KPa)	HP_{Tj} (KPa)
Normal case	0.04	-0.02	0.68	-0.2	1.27
Stiffened EC	0.04	-0.02	0.69	-0.03	1.47
Stiffened St	0.07	-0.02	0.65	0.009	1.42
Stiffened CPE	0.28	-0.005	2.3	-0.41	3.99

Table 12: Detailed analysis assessing the impact of stiffened endothelial cells (EC), Stroma (St), and choroid plexus epithelium (CPE) on Q_{PI} : pulsatility index for total CSF production, OP_{APM} : osmotic pressure difference between CPE and vent, HP_{APM} : hydrostatic pressure difference between CPE and vent, OP_{Tj} : Osmotic pressure difference between St and vent, HP_{Tj} : hydrostatic pressure difference between St and vent.

stiffened St and CPE are increased from 0.04 in a normal case to 0.07 and 0.28, respectively. One reason for such behaviour can be explained by the nature of the elastic and viscoelastic properties of the Stroma and CPE. respectively. In general, the pulsation in our model is cardiac induced, affected by the flow and pressure pulse at capillary inlet and the pressure at ventricular system. The pathway for the pulse in through Stroma and CPE into the ventricular system. In a normal case the elastic property of the tissues absorbs some of the pulse, however in the less elastic tissues (i.e. rigid) the pulse is less absorbed which leads to amplified pulse. This behaviour becomes more exaggerated when viscosity is involved as well, as viscosity is another factor absorbing the shocks. In other words, viscous-elastic materials when subjected to a sudden shock relax over time and slower than solely elastic materials.

Effect of dehydration on CSF production

Figure 29-left represents the total CSF production via choroid plexus under conditions where the interfaces (EC, BLM, APM and TJ) lose their ability to transfer water efficiently. This physiological change in our model is imposed by diminishing the magnitude of hydraulic conductivity (L_p) for each interface. The average CSF production decreases in all cases, however the diminish is most significant for EC dehydration; 43%. This reduction in BLM, APM and TJ are 5, 1.3 and 1%, respectively (Figure 29-right).

In the first case, the OP across the APM remains unchanged, the magnitude of the

Variable	Q_{PI}	OP_{APM} (KPa)	HP_{APM} (KPa)	OP_{Tj} (KPa)	HP_{Tj} (KPa)
Normal case	0.04	-0.02	0.68	-0.2	1.27
Dehydrated EC	0.06	-0.02	0.23	-3.02	-2.4
Dehydrated BLM	0.02	-0.01	0.68	-1.28	1.29
Dehydrated APM	0.02	-0.2	0.68	-0.4	1.27
Dehydrated TJ	0.03	-0.03	0.68	-0.4	1.27

Table 13: Investigation of the effect of dehydrated interfaces such as endothelial cells (EC), basolateral membrane (BLM), apical membrane (APM), and tight junction (TJ) on Q_{PI} : pulsatility index for total CSF production, OP_{APM} : osmotic pressure difference between CPE and vent, HP_{APM} : hydrostatic pressure difference between CPE and vent, OP_{TJ} : Osmotic pressure difference between St and vent, HP_{TJ} : hydrostatic pressure difference between St and vent.

corresponding force inserted to the TJ increases from 0.2 in normal case to 3.02 (KPa). In other words, the OP between the Stroma and Ventricle imposes a large volume of water outflow. The HP across the APM drops by 3-fold, but this pressure changes sign across TJ (Table 13); indicating the HP in Stroma increases beyond the pressure in ventricle, causing the abnormal backflow into the Stroma. Furthermore, the dehydration of all other interfaces only impacts the osmotic pressures and not the hydrostatic pressures. This observation can be explained by one of the mechanisms that solute transfers across membranes: advection. By this mechanism, water crossing EC and TJ can carry solutes; hence changing the osmotic pressure. Therefore, when a membrane dehydrates and loses its ability to transport water efficiently, the less solute is transported which results in increase of osmotic pressure difference across membranes. These observations emphasis

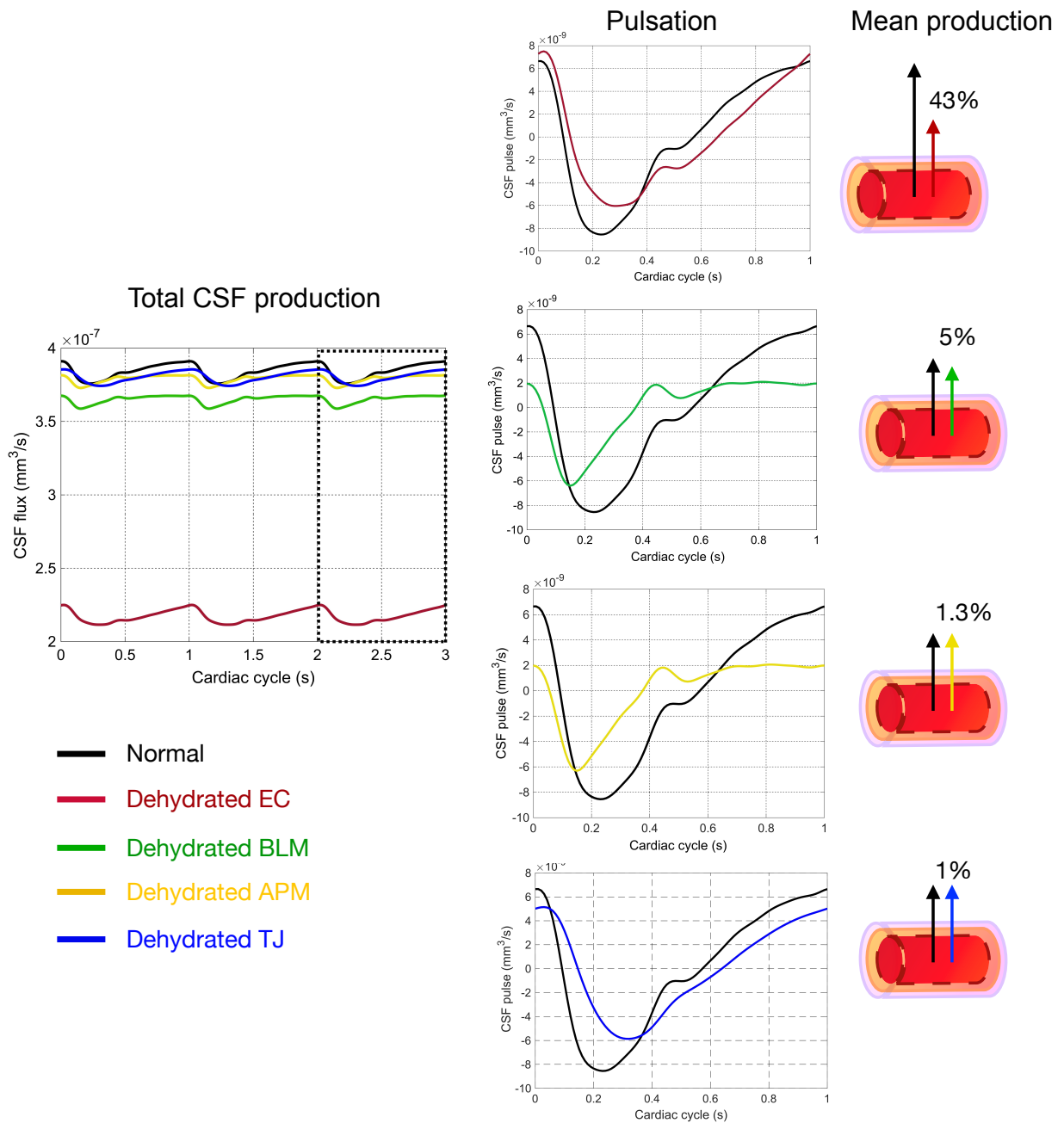


Figure 29: Impact of interfaces dehydration on CSF production. Left: total CSF production for 3 seconds, middle: CSF pulses for 1 second, right: the schematic diagram of the relative percentage difference of mean CSF production between normal and each abnormal condition.

on the importance of osmotic pressures on water production in the system.

Effect of CPE reduction on CSF production

Epithelial atrophy is repeatedly reported in various conditions such as ageing, Alzheimer’s and Parkinson’s disease [126, 69]. In our model, we impose a 10% reduction to the epithelial cell (i.e. reducing the radius of CPE) and investigate the CSF production (Figure 30). The average CSF production decreases by 16% in comparison to the normal case. The OP across the APM and TJ remain relatively unchanged. i.e.the epithelial atrophy does not change the OP. However, a striking feature of the cell reduction is significant on the HP; not only the magnitudes across APM and TJ decreases significantly but they also change sign., i.e. imposing backflow into CPE and Stroma from the ventricular system at a small magnitude. Among all studies conducted to investigate effect of on CSF production, this is the only case where the CSF will flow back from ventricular system into the CPE and Stroma. In addition, the signal keeps its original characteristics; there

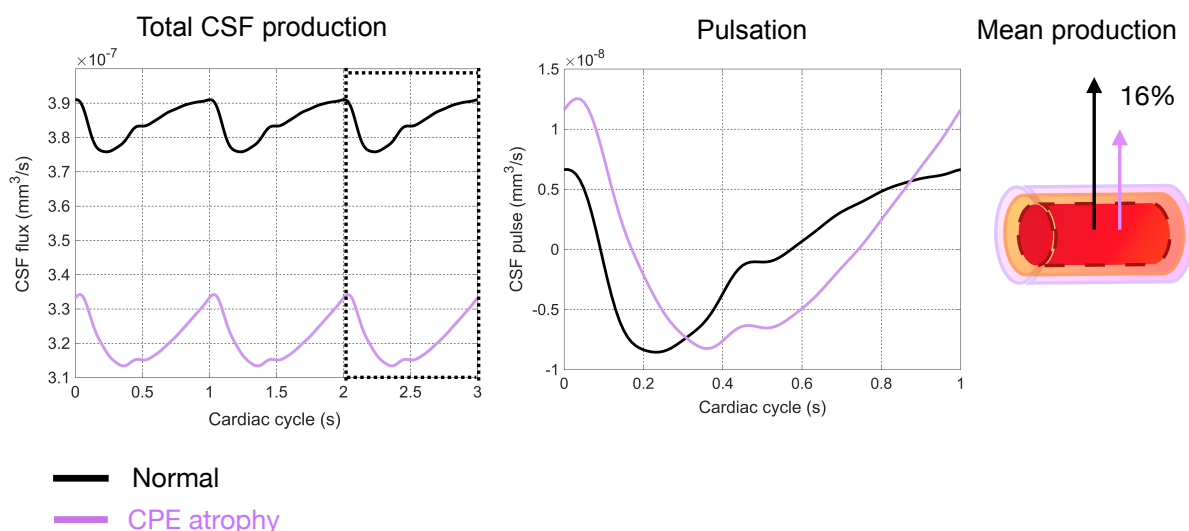


Figure 30: Impact of CPE atrophy on CSF production. Left: total CSF production for 3 seconds, middle: CSF pulses for 1 second, right: the schematic diagram of the relative percentage difference of mean CSF production between normal and each abnormal condition.

is a minimum followed by a plateau, but the minimum experiences a shift and the plateau takes place almost at the new minimum side.

Variable	Q_{PI}	OP_{APM} (KPa)	HP_{APM} (KPa)	OP_{Tj} (KPa)	HP_{Tj} (KPa)
Normal case	0.04	-0.02	0.68	-0.2	1.27
CPE Atrophy	0.06	-0.03	-0.4	-0.13	-0.55

Table 14: Impact of reduced epithelium size on components of CSF production. Q_{PI} : pulsatility index for total CSF production, OP_{APM} : osmotic pressure difference between CPE and vent, HP_{APM} : hydrostatic pressure difference between CPE and vent, OP_{Tj} : Osmotic pressure difference between St and vent, HP_{Tj} : hydrostatic pressure difference between St and vent.

Effect of Transporters on CSF production

In this section, we reduced the activity of two transporters located on APM; Na-K-ATP and NKCC to examine their effect on CSF production across CP. The reduction of ATP activity resulted in a 6% decrease in CSF flux, whereas a similar change on NKCC transporter led to a 45% increase in CSF production. ATP activity reduction had a small impact on the OP across APM and TJ, however the impact is significant in NKCC reduction; the OP across APM and TJ increase by 50% and 190%, respectively. In the first case, The HP across the interfaces do not seem to be significantly affected by the activity of transporters. Such analysis provides insight about the importance of OP on CSF production in the system, more specifically the osmotic pressure gradient between Stroma and ventricle (i.e. across TJ).

Since reduction in activity of transporters directly impacts the solute transports, we

Variable	Q_{PI}	OP_{APM} (KPa)	HP_{APM} (KPa)	OP_{Tj} (KPa)	HP_{Tj} (KPa)
Normal case	0.04	-0.02	0.68	-0.2	1.27
Reduced ATP activity	0.04	-0.02	0.53	-0.17	1.04
Reduced NKCC activity	0.03	-0.03	0.72	-0.58	1.2

Table 15: Detailed analysis of the significance of ATP and NKCC transporter activities on component of CSF production. Q_{PI} : pulsatility index for total CSF production, OP_{APM} : osmotic pressure difference between CPE and vent, HP_{APM} : hydrostatic pressure difference between CPE and vent, OP_{Tj} : Osmotic pressure difference between St and vent, HP_{Tj} : hydrostatic pressure difference between St and vent.

conducted further analysis on investigating the solute concentrations of the four most important ions (as explained in the last chapter, Cl , K , Na , and HCO_3) inside the compartments of Stroma, CPE, and ventricles. Reduction of the ATP, that takes 3 Na outside the CPE and 2 K into the cell) has the most significant impact on intercellular Na, Cl, and HCO_3 , respectively. The intercellular concentration of Na increases by 17 mM, whereas Cl and HCO_3 decrease by 4 and 3 mM. Consequently, reduction in activity of NKCC transporters (2Cl, Na, and K into the cell) causes the Cl in Stroma to decrease by 5mM, and the intercellular concentration of Cl and Na to decrease by 1 and 3 mM, respectively.

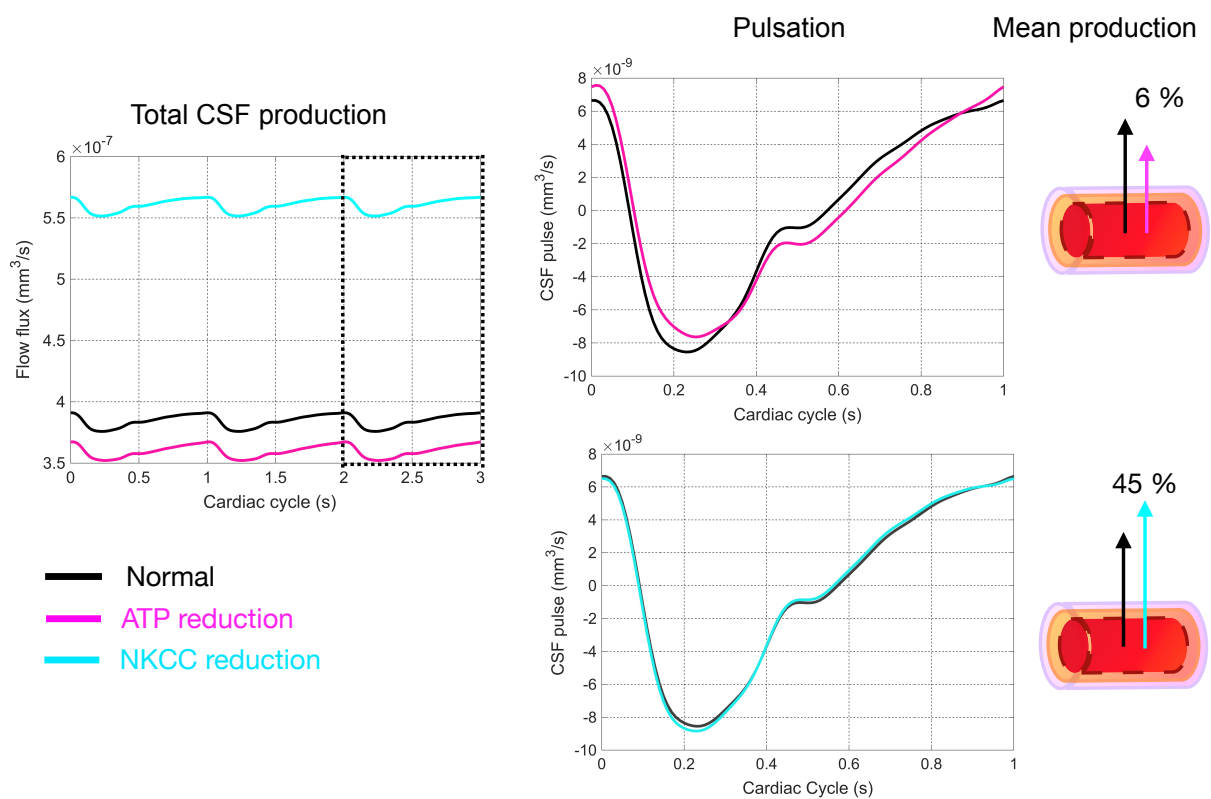


Figure 31: Effect of ATP and NKCC transporters on CSF production. Left: total CSF production for 3 seconds, middle: CSF pulses for 1 second, right: the schematic diagram of the relative percentage difference of mean CSF production between normal and each abnormal condition.

5.3.2 Capillary morphology

To date, the exact mechanism by which the CP removes waste and unwanted products (e.g. $A\beta$, T cells) in a healthy brain and the reason for their aggregation in aged or diseased states remain elusive [44]. However, one proposed mechanism for drainage is the force imposed by the wave on the endothelial cell walls; the EC compression and expansion induces a force and provides pathways directions for drainage [27]. Therefore, in this section we analyse the alterations in the capillary size and the corresponding endothelial wave against the normal condition. Since the volumetric change of capillary, in the dynamic model, is a balance between the blood influx and efflux (i.e. $\frac{dv}{dt} = Q_{in} - Q_{out} - Q_{EC}$), we take a step further into analysing the dynamics of flow in capillary under various conditions. Note that in the model, the Q_{in} is an inlet condition and it does not change under any of the conditions applied. Therefore, the alterations will be on fluid leaving the capillary (Q_{out} downstream and Q_{EC} across). Our analysis shows that Q_{out} remains unchanged; hence the alterations are induced by the fluid flow across the EC, which will be discussed further in the following subsections.

Effect of elasticity on capillary morphology

The average radius for capillary in normal case is computed to be 6.4 micrometer, a value that is well in agreement with the literature [102]. Table 16 reports the average capillary radius under normal and abnormal conditions of stiffening EC, St, and CPE. The results suggest only CPE stiffening affects the size of capillary vessel; the value increases to 8.7 micrometer. We postulate, this observation to be related to the impact that the stiffness has on CSF production as shown in the previous section: The water transport increased by 40%. The system can provide such high production because the flow across EC has increased. i.e. further analysis shows that the flow rate across the EC increases by 47%, relative to the normal case.

Figure 32 plots the comparison between the endothelial cells wave in the normal and stiffened CPE. Although the shape of the signal does not significantly change, but the pulse amplitude increases by an order of magnitude (reported in Table 16).

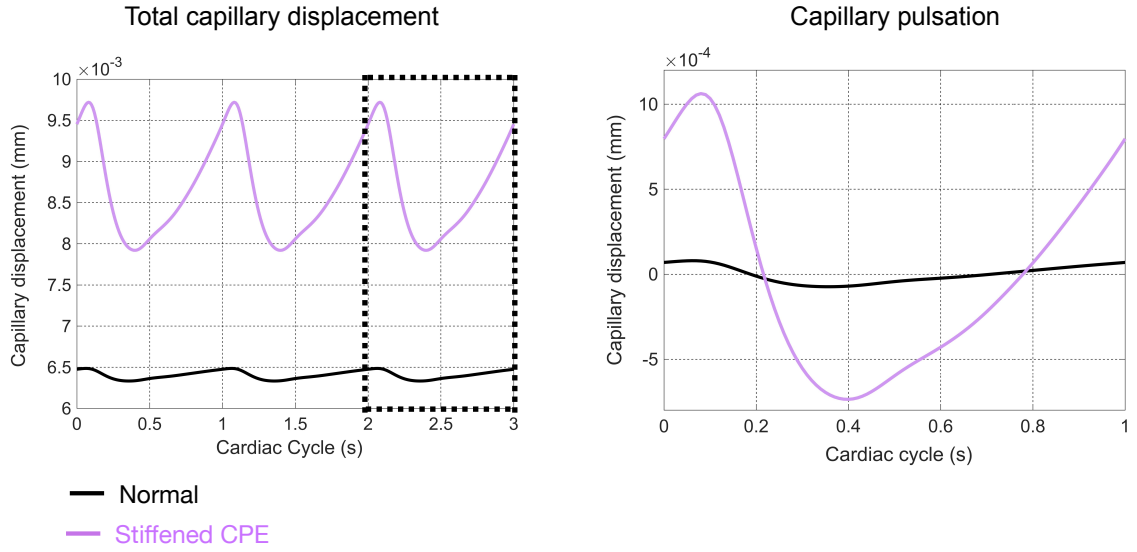


Figure 32: Impact of CPE stiffness on capillary morphology (left) and its pulsation (right).

Variable	R_m μm	R_p μm	$Q_{m_{out}}$ mm^3/s	$Q_{m_{EC}}$ mm^3/s
Normal case	6.4	0.15	1.8×10^{-3}	3.8×10^{-7}
Stiffened EC	6.5	0.18	1.8×10^{-3}	3.8×10^{-7}
Stiffened St	6.4	0.14	1.8×10^{-3}	3.5×10^{-7}
Stiffened CPE	8.7	1.18	1.8×10^{-3}	5.6×10^{-7}

Table 16: Analysis for impact of stiffness of endothelial cells (EC), Stroma (St), and choroid plexus epithelium (CPE) on capillary morphology. The analysis are conducted by studying the alterations in average capillary radius R_m , pulsation of capillary, R_p , average flow rate out of capillary compartment $Q_{m_{out}}$, and average flow rate across EC, $Q_{m_{EC}}$.

Effect of dehydration on capillary morphology

In this investigation, we reduced the hydraulic conductivity of all membranes including the tight junction and studied its impact on the capillary behaviour. Our findings show the dehydration of the interfaces have a minimal impact on the capillary size, (Table 17). The highest change is correlated with EC dehydration, a reduction of capillary size by only 4%. As expected, this physiological change will also have an impact on flow

across EC, a decrease by 44%. Although the capillary size is not affected significantly, the pulse amplitude of endothelial cells wave reduces by 65%. A normal capillary size with a diminished forces imposed by its confined wall may lead to solute deposition.

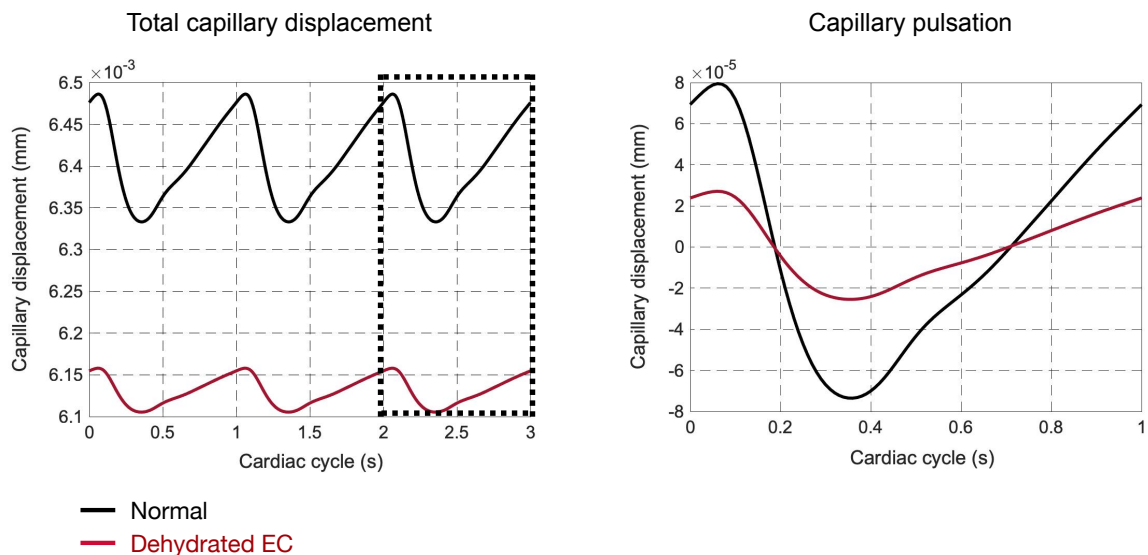


Figure 33: Impact of endothelial cell dehydration on capillary morphology (left) and its pulsation (right).

Variable	R_m μm	R_P μm	$Q_{m_{out}}$ mm^3/s	$Q_{m_{EC}}$ mm^3/s
Normal case	6.4	0.15	1.8×10^{-3}	3.8×10^{-7}
Dehydrated EC	6.1	0.05	1.8×10^{-3}	2.1×10^{-7}
Dehydrated BLM	6.4	0.15	1.8×10^{-3}	3.6×10^{-7}
Dehydrated APM	6.4	0.15	1.8×10^{-3}	3.8×10^{-7}
Dehydrated TJ	6.4	0.15	1.8×10^{-3}	3.8×10^{-7}

Table 17: Detailed analysis for dehydrated interfaces such as endothelial cells (EC), basolateral membrane (BLM), apical membrane (APM), and tight junction (TJ) on capillary morphology. The analysis are conducted by studying the alterations in average capillary radius R_m , pulsation of capillary, R_P , average flow rate out of capillary compartment $Q_{m_{out}}$, and average flow rate across EC, $Q_{m_{EC}}$.

Effect of CPE atrophy on capillary morphology

A 10% reduction in the epithelial cell size causes a similar reduction in capillary size with a decreased pulse amplitude of 70%. In addition, the flow across the endothelial cell will reduce by 17%. A unique impact that epithelial atrophy causes to the wave of endothelial cell (Figure 34-left); In normal condition, the epithelial cell expands to its maximum at approximately 0.06 into cardiac cycle which is followed by a rapid fall and experiences its compression at 0.36 seconds. This characteristic reverses in the abnormal case; the compression takes place at 0.06 seconds and the expansion at 0.36 seconds. We further investigated the possible source for such characteristic change by comparing the CSF efflux from the capillary (Capillary outlet and EC) and plot the results in Fig (35). Note that the CSF influx is not accounted because it is an inlet condition and do not change. The results show that fluid flow signal down the capillary dampens and there

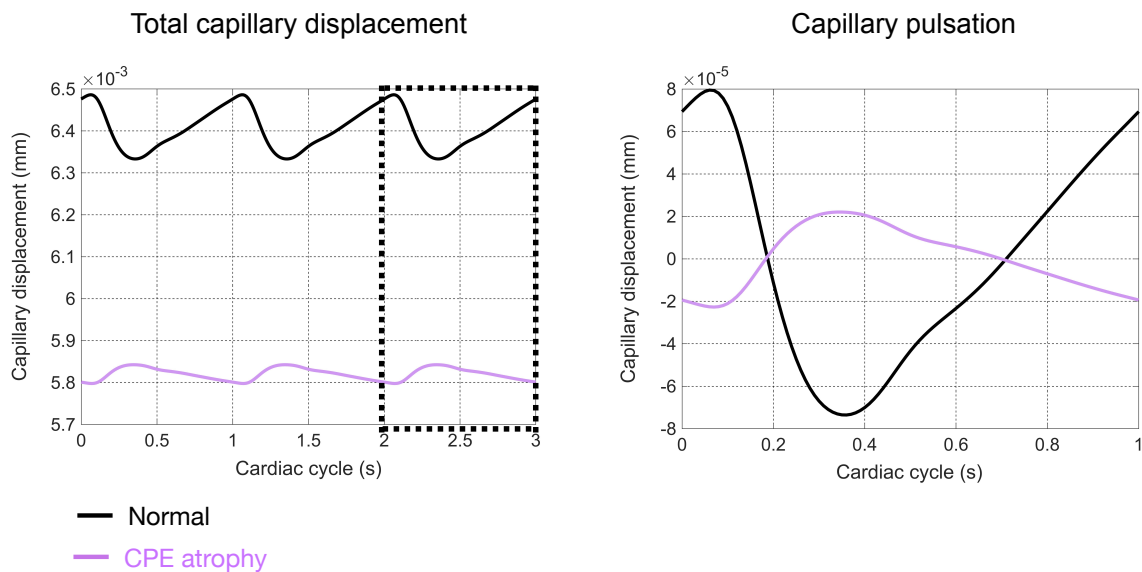


Figure 34: Impact of CPE atrophy on capillary morphology (left) and its pulsation (right).

is phase lag ϕ , of 5% (i.e. the difference between the peaks of fluxes in normal and abnormal cases) observed between the normal and abnormal case (blue lines are normal case). A similar characteristic is seen in EC: the flow across the EC experiences a phase lag ϕ , of 10%. These characteristic changes in the signal seems to be sufficient to affect the wave of endothelial cells. In addition, it can be seen that the dynamics of the flow at

Variable	R_m μm	R_P μm	$Q_{m_{out}}$ mm^3/s	$Q_{m_{EC}}$ mm^3/s
Normal case	6.4	0.15	1.8×10^{-3}	3.8×10^{-7}
CPE Atrophy	5.8	0.04	1.8×10^{-3}	3.1×10^{-7}

Table 18: Impact of in epithelial cells reduction on capillary morphology. The analysis are conducted by studying the alterations in average capillary radius R_m , pulsation of capillary, R_P , average flow rate down the capillary compartment $Q_{m_{out}}$, and average flow rate across EC, $Q_{m_{EC}}$.

large scales (relative to system) have not changed (Q_{in}, Q_{out}) but the dynamics at small scale (Q_{EC}) changed and reversed the EC wave. In other words, the balance between the water influx and efflux of capillary allows the EC to have a certain characteristic (shown in Figure 35). This characteristic changes when the balance is impaired.

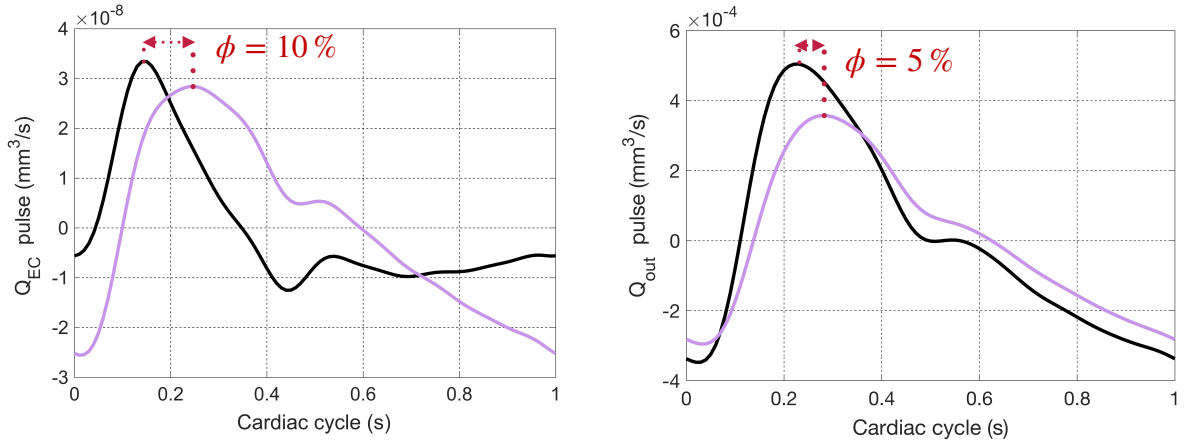


Figure 35: Comparison between the CSF efflux across endothelial cells (left) and CSF efflux down the capillary (right) for normal (black lines) and in CPE atrophy case (purple line).

5.3.3 Choroid plexus volume

Volumetric alterations of choroid plexus have been observed in neurological disorders such as Alzheimer's and Parkinson's disease [93, 23, 144]. Recent clinical studies emphasize on the need to conduct in-depth studies on the role of CP volumetric alterations in neurological conditions [54]. In this section, we examine the effect of pathophysiological alterations on the volumetric change in choroid plexus. In addition, we assess the pulsation that is induced by the volumetric change due to two main reasons. One is that CP motion is a source for pulsatile CSF circulation inside the ventricular system. Therefore, alterations in the CP motion can directly impact the CSF circulation and lead to various abnormal conditions. To elaborate further, x argues that increased CSF pulsation may lead to expansion of ventricular walls and cause hydrocephalus. Second is that abnormal volumetric change can excessively stretch the interfaces (e.g.APM and TJ) and lead to their deterioration and result in an imbalance of solute in the CSF system or facilitate entrance of unwanted substances to the CSF system.

Effect of elasticity on CP volume

Impact of each medium stiffening on CP expansion is reported in Table 19. CPE stiffening results in a significant average volumetric expansion by two orders of magnitude. This observation raised the question on what compartment among the three expands the most (Table 19). The analysis show that CPE stiffening increases the size of capillary and stroma by 35% and 71%, respectively, but decreases size of CPE by 10%. The waveform of total volumetric change for normal and the influenced case are provided for 3 seconds in Figure 36-left. In order to analyse the signal further, the average value is removed and the signal is shown for 1 second (Figure 36-right). The result shows a significant increase in the pulse amplitude by one order of magnitude, however plotting the signals in two separate figures show the characteristics of the signal do not change. The choroid plexus experiences a compression at approximately 20% of the cardiac cycle and slowly expands for the rest of the cycle.

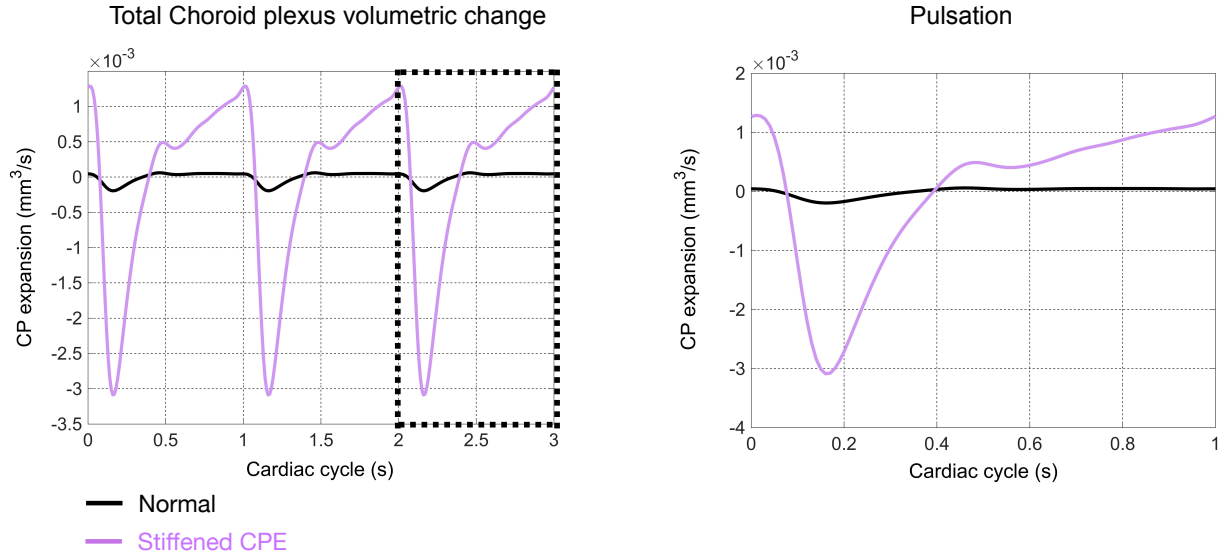


Figure 36: Impact of CPE stiffness on total choroid plexus volumetric change (left) and its pulsation (right).

Variable	dV/dt_m mm^3/s	dV/dt_P mm^3/s	R_{cap} μm	R_{St} μm	R_{CPE} μm
Normal case	4.5×10^{-7}	2.5×10^{-4}	6.4	11.1	7.8
Stiffened EC	5.3×10^{-7}	3.1×10^{-4}	6.5	11.4	7.7
Stiffened St	4.5×10^{-7}	2.4×10^{-4}	6.4	1.05	8
Stiffened CPE	1.29×10^{-5}	4.3×10^{-3}	8.7	19	7

Table 19: Analysis for impact of stiffness of endothelial cells (EC), Stroma (St), and choroid plexus epithelium (CPE) on Choroid plexus volume. The investigations are on the alterations in average CP radius volumetric expansion $\frac{dV}{dt}_m$, its pulsation, $\frac{dV}{dt}_P$, mean radius capillary R_{cap} , mean radius Stroma R_{St} , and mean radius CPE R_{CPE} .

Effect of dehydration on CP volume

Among the four investigated interfaces, decreased hydraulic conductivity (LP) of endothelial cells is the only one leading to volumetric change on the CP. The average volume reduces by 70% relative to the normal condition, along with a significant reduction of the pulse amplitude i.e.67%. Further investigation reveals that the Stroma undergoes a considerable reduction by 40%. Although CPE increases by 20%, but it does not compensate for the overall reduction of the tissue.

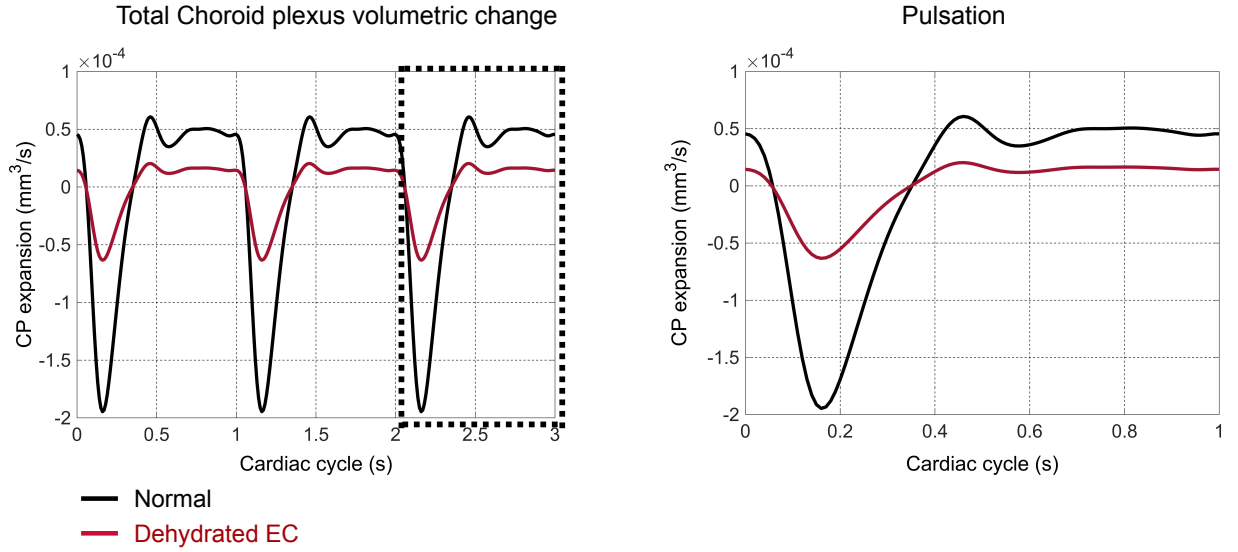


Figure 37: Impact of endothelial cell dehydration on choroid plexus volumetric change (left) and its pulsation (right).

Variable	$\frac{dV}{dt}_m$ mm^3/s	$\frac{dV}{dt}_p$ mm^3/s	R_{cap} μm	R_{St} μm	R_{CPE} μm
Normal case	4.5×10^{-7}	2.5×10^{-4}	6.4	11.1	7.8
Dehydrated EC	1.36×10^{-7}	8.36×10^{-5}	6.1	6.5	9.4
Dehydrated BLM	4.55×10^{-7}	2.56×10^{-4}	6.4	11.1	7.8
Dehydrated APM	4.55×10^{-7}	2.55×10^{-4}	6.4	11.1	7.8
Dehydrated TJ	4.5×10^{-7}	2.55×10^{-4}	6.4	11.1	7.8

Table 20: Analysis for impact of dehydration of endothelial cells (EC), basolateral membrane (BLM), apical membrane (APM), and tight junctions (TJ) on Choroid plexus volume. The investigations are on the alterations in average CP radius volumetric expansion $\frac{dV}{dt}_m$, its pulsation, $\frac{dV}{dt}_p$, mean radius capillary R_{cap} , mean radius Stroma R_{St} , and mean radius CPE R_{CPE} .

Effect of CPE atrophy on CP volume

It is not surprising that epithelial atrophy reduces the mean volumetric change of CP in comparison to the normal case, however the waveform representing the volumetric change mirrors the signal in normal condition; the peak in abnormal condition occurs where the original signal experiences a minimum. Another feature is the amplitude reduction by 70%. It is worth noting that the cell reduction by 10% was set as an initial condition

Variable	$\frac{dV}{dt}_m$ mm^3/s	$\frac{dV}{dt}_P$ mm^3/s	R_{cap} μm	R_{St} μm	R_{CPE} μm
Normal case	4.5×10^{-7}	2.5×10^{-4}	6.4	11.1	7.8
CPE Atrophy	1.1×10^{-7}	7.5×10^{-5}	5.8	10.5	8.1

Table 21: Analysis for impact of epithelial cell atrophy on Choroid plexus volume. The investigations are on the alterations in average CP radius volumetric expansion $\frac{dV}{dt}_m$, its pulsation, $\frac{dV}{dt}_P$, mean radius capillary R_{cap} , mean radius Stroma R_{St} , and mean radius CPE R_{CPE} .

to the model. However, the dynamic model computes for the size of CPE in transition. The results show that after the transition is passed and the system reaches a stability the CPE is increased by 4%, in comparison to the normal condition (table 21).

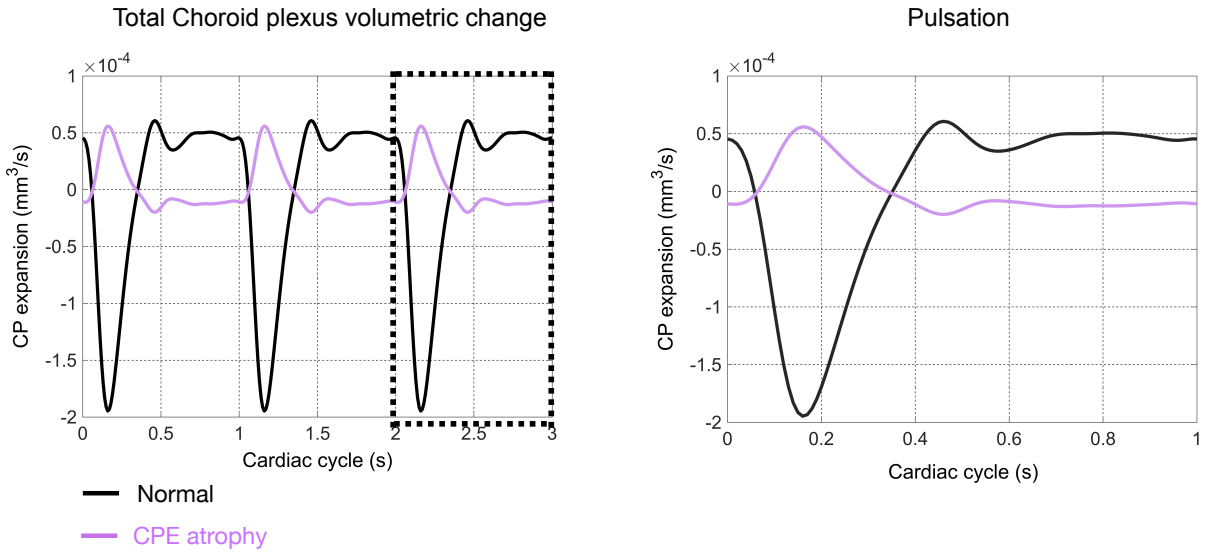


Figure 38: Impact of epithelium atrophy on choroid plexus volumetric change (left) and its pulsation (right).

5.4 Chapter summary & future work

In this chapter, the impact of normal ageing (i.e. mediums' stiffness, dehydration and epithelial atrophy, and transporters activities) on the dynamics of three variables: CSF production, capillary morphology, and choroid plexus volume, were explored. The choice of these investigated variables are due to their role in development of various neurological conditions. For instance, overproduction of CSF can lead to hydrocephalus, and it's under production may impair waste removal function from the ventricular system, which leads to deposition of particles (e.g. $A\beta$) on the ventricular walls. Such pathology can further alter the normal circulation of CSF in the ventricular domain and impact the neurogenesis.

The reason for examining morphology of capillary is that under normal conditions, capillaries are postulated to remove unwanted particles by imposing a force on them. The source of the force is from the expansion and compression of the vessel which leads to attachment and detachment of the particles and directing them towards the outlet. In abnormal conditions (e.g. enlarged capillaries), the force may not be sufficient for waste removal. Finally, we studied the choroid plexus volumetric change under different conditions. As discussed earlier, CP is one of the barriers that protects the brain. Pathological changes (e.g. over expansion) of CP can lead to deterioration of the system, allowing the entrance of harmful substances such as viruses to the ventricular system, or alternatively lead to an imbalance in entry of some particles (e.g. T cells).

Therefore, we conducted this research by performing ten simulations, one for each affected parameter by ageing (i.e. Stiffness of EC, St, CPE, dehydration of EC, BLM, APM, TJ, CPE atrophy, reduced activity of ATP and NKCC transporters). Results obtained from each simulation were discussed and analysed in detail. i.e. we first reported their direct impact on each variable (concluded in Table 22) and then investigated the possible roots and causes to explain the observations. For CSF production, the significance of hydrostatic and osmotic pressure differences was discussed. To analyse the root for alteration in capillary morphology, we studied the water influx and efflux across capillary. Finally, we analysed the impact of ageing on the overall volumetric change of choroid plexus and as an attempt to find the source, we analysed the size of each compartment: capillary,

Parameter	Medium	CSF Production			Capillary morphology			Choroid plexus volume		
		Mean	Pulse Index	Signal characteristic	Mean	Pulse	Signal characteristic	Mean	Pulse	Signal characteristic
Elasticity	EC	—	—	—	—	—	—	—	—	—
	St	↓	↑	—	—	—	—	—	—	—
	CPE	↑	↑	YES	↑	↑	YES	↑	↑	YES
Dehydration	EC	↓	↑	—	↓	↓	—	↓	↓	—
	BLM	↓	↓	—	—	—	—	—	—	—
	APM	—	↓	—	—	—	—	—	—	—
	TJ	—	↓	—	—	—	—	—	—	—
Epithelial Atrophy	CPE	↓	↑	YES	↓	↓	YES	↓	↓	YES
Transporter activity	ATP	↓	—	—	—	—	—	—	—	—
	NKCC	↑	—	—	—	—	—	—	—	—
Pathophysiology & abnormal conditions	Enlarge ventricles, Reduce waste clearance, Impair neurogenesis. Hydrocephalus, Alzheimer, Parkinson.			Deposition of solutes in the choroidal capillary. Alzheimer.			Solute imbalance in the CSF. Alzheimer, Multiple Scleroses, Parkinson.			

Table 22: Main constituent in blood accounted in this study and their concentrations. The unit is nmol/mm^3

Stroma, and epithelial cell.

In order to conclude the main findings, Table 22 is generated. The parameters that were changed in our simulations to represent ageing are tabulated in the left rows, and the variables that were investigated are represented in the column headers. Each variable is investigated by its mean value, pulse value, and whether the character of the signal representing the variable has been affected. For the sake of easy reading, we show the main findings by symbols: Upward arrows represent an increase in the magnitude of the studied variable in comparison to the normal case, and the downward arrows represent its reduction. The larger the arrow, the more significant the alteration. To represent a significant change in characteristic changes of the signals, we use YES.

It can be concluded that the increased elasticity of CPE and reduction in NKCC activity can lead to overproduction of CSF (i.e. enlarged ventricles/ hydrocephalus), whereas

dehydration of EC and epithelial atrophy significantly reduce the CSF production. In addition, the CPE stiffness, and its atrophy significantly alter the capillary morphology, but in opposite ways i.e. the former enlarges the capillary and its pulsation while the latter reduces the vessel size and its pulsation. Finally, CPE stiffness expands the CP, while EC dehydration and CPE atrophy have the opposite impacts.

Having such a holistic model is beneficial when examining large numbers of parameters; we conducted 10 computationally cheap simulations and the results suggest that the ageing of four of these parameters may lead to pathological conditions. In the future, more studies must be conducted to characterise these changes and assess these alterations in order to further address the occurrence of pathological disorders. One example is by conducting 3D simulations and studying the flow and solute dynamics across capillaries in normal conditions and assessing them in enlarged vessels with magnified pulses (associated with CPE stiffness) to investigate whether particle deposition takes place.

Another example is to conduct 3D simulations on the ventricular surface and characterise the forces on ventricles in normal and abnormal CSF production. This investigation, however, has started and is the main topic of the following chapter.

6 CSF Circulation in the Ventricular System

6.1 Introduction

In the last two chapters, we investigated the CSF production by CP. In the current chapter, we initiate studying the CSF circulation in the ventricular system. To recap, CSF flows inside a set of four interconnected ventricular system. This fluid ensures the brains health by providing hydromechanical, biochemical, and neurogenic support. In addition, CSF is used in medical field to to measure intracranial pressure, and detect unwanted protein, glucose, and viruses in the brain.

The location and structure of the CSF system adds to its importance; it connects different regions of the brain from left to right hemispheres, including all four brain lobes, each of which have different functions to control the brain (Figure 39). The boundaries of the ventricles are composed of ependymal cells; ciliated cuboidal cells residing next to each other with a gap junction of 2-4 nm, large enough to allow for exchange of solutes between the brain parenchyma and the CSF system [26].

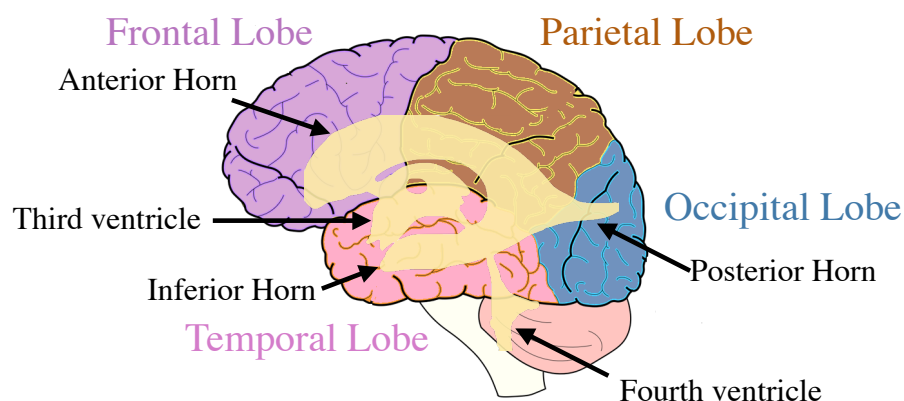


Figure 39: Sagittal view of the brain: the four lobes and ventricular system. The anterior horn, body, posterior, and inferior horns of the lateral ventricle are located in the frontal, parietal, occipital, and temporal lobes. Associated functions of lobes: Frontal: thinking, memory, & movement. Parietal: language and touch. Occipital: sight. Temporal: hearing, learning and feelings.

Therefore, the disturbances in the natural fluid flow pattern or its composition can effect the brain functions and be lead to onset and progression of variety of neurological disorders and neurodegenerative diseases such as Hydrocephalus, Alzheimer, Multiple

Sclerosis, and Chiari Malformation [48, 149, 61].

Most aforementioned neurological conditions have been known for centuries but their aetiology remain unknown. Consequently, finding cure or effective treatments have been challenging. From medical perspectives, this can be due to the common symptoms among the neurological disorders which leads to misdiagnosis. According to the Alzheimer's association, normal pressure hydrocephalus (NPH) is often misdiagnosed for Alzheimer's or Parkinson's disease. In fact, approximately 80% of people with the Parkinson's disease are improperly diagnosed [15]. Similarly, Chiari Malformations is misdiagnosed as Multiple Sclerosis or spinal cord tumour [156].

One main reason for such misdiagnosis is our limited and expensive access to human brain. We lack understanding of CSF circulation dynamics in normal condition (more discussion in chapter 2). The CSF circulation within the ventricular system has a pulsatile nature. The main cause of such pulsatility is still debatable. There are three proposals as the main source for the pulsation; pulsatile CP production flow rate, pulsatile deformation of CP tissue and ventricular system, and pulsation of cilia located on the ependymal cells, covering ventricular boundary. Confirming the main source and the contribution of each to the flow production and pulsation in healthy and normal scenario improves our approach to disturbed conditions, possibly leading to finding their aetiology and better treatments.

Medical techniques enable us to quantify some features of the flow field within the ventricular system. The two gold standard techniques are phase-contrast magnetic resonance imaging (PC-MRI) and continuous ICP monitoring. The former is a non-invasive technique measuring the flow velocity, whereas the latter measures CSF pressure by placing a sensor within the ventricles. Both methods enhance our understanding of the overall flow dynamic but currently are incapable of providing detailed local information.

On the other hand, advances in computational power allows us to fill the gap at lower costs with higher resolutions. An advantage of computational study is that it can be tailored for patients. i.e. subject specific. This is however a challenging task since computations rely heavily on accuracy of models and precision of boundary and initial conditions. Computational fluid dynamics (CFD) studies can lead to a realistic prediction if they are provided with real geometry and close to real boundary conditions. There

have been attempts to conduct CFD studies (discussed in chapter 2, specifically Table 1). Due to geometric complexity of the ventricular system and their controversial boundary conditions, many attempts to investigate the flow dynamic relied on idealised geometry or oversimplification of the boundary conditions.

Filling such a significant gap in medical practice and our understanding of CSF circulation requires a step-by-step investigation, starting with a series of thorough studies with basic principles. This is to understand the normal flow pattern, making it possible to extend it to abnormal states. In the first step, we conduct a study of CSF circulation in a real geometry, imposing a close to real inlet boundary condition. In the future, the boundary conditions must be improved to include all the possible sources of CSF pulsation as described in Chapter 2. Note that our current study is also limited to lateral ventricles and a portion of third ventricle.

6.2 Methodology

6.2.1 MR imaging & geometry reconstruction

A Magnetic Resonance Imaging (MRI) was performed at Great Ormond Street Hospital (GOSH) by Dr Kristian Aquilina to capture a 3D geometry of lateral ventricles and a portion of the third ventricle for a 5-year-old boy with normal brain conditions. Professor Carlos Martinez, from biomedical engineering department at City, University of London, utilised the MRI pictures and provided us with a map of ventricular boundary (Figure 40). The data represents the surface by connected triangular mesh and are composed of two datasets: one contains the coordinates of points (16,660 points) and the other one provides a matrix of their coordinates (33,320 rows and three columns). Each row contains three numbers; the first element is the identifier followed by the identifier of points composing each triangle. The next step was to export the geometry into a mesh generating tool, Pointwise.

6.2.2 Mesh generation

The geometry provided to us was one entity, with no allocation for choroid plexus location and the outlet boundary. Therefore, we conducted literature review and defined the

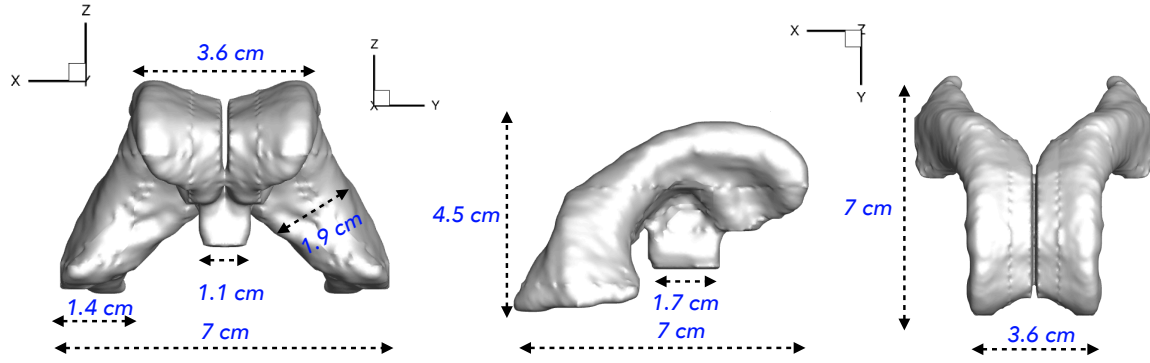


Figure 40: Views of real cerebral ventricles obtained from MRI 5-year old boy. From left to right: Coronal, Sagittal, and Horizontal planes.

approximate area and location for CP in LVs. The findings are represented in Table 23. The next step was to allocate CP and the outlet from the overall map of LV boundary. A code was written in MATLAB that enabled us to separate them. Afterwards, we converted the data into a format (i.e. STL) readable in Pointwise.

The next step was to import the ventricular boundaries, now separated in their nature, into Pointwise. Since the geometry is complicated and it requires fine grid cells, we had to use the code and break down the geometry into smaller parts, separately import them into Pointwise and apply meshing process. The geometry is represented by unstructured mesh that has 240,947 points and 1,298,208 cells (Figure 41).

Domain	Surface Area <i>cm</i> ²	Surface Cells No.	Volume cells No.
Each choroid plexus/inlet	7.5	1,714	
Outlet	0.15	150	
Ventricular surface	202.98	95,672	
Ventricular volume			1,298,208

Table 23: Summarised specifications for model set-up.

6.2.3 CFD methodology

The commercial CFD numerical solver OpenFOAM was used to predict the CSF flow dynamics inside the ventricular system. The software uses finite volume method and

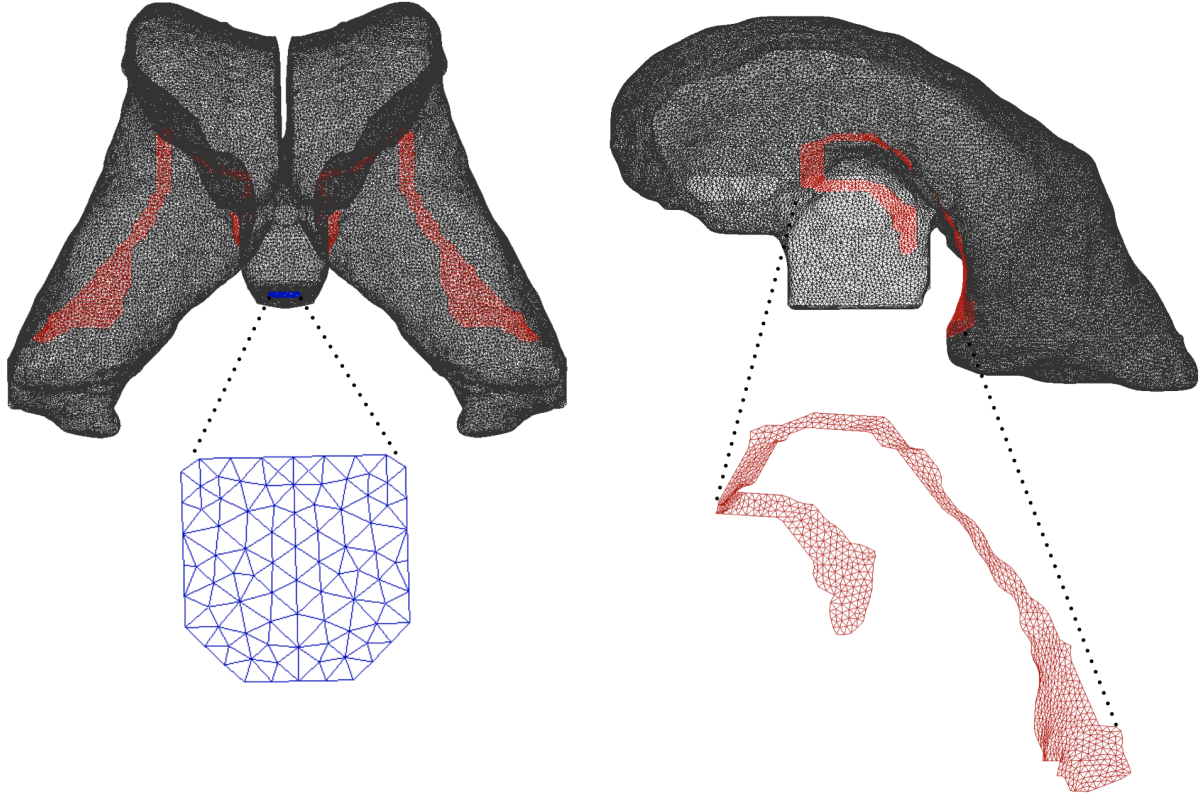


Figure 41: Coronal (left) and Sagittal (right) views of the reconstructed geometry of lateral ventricles. black mesh represent the surface area of the LVs, the regions marked in red are the choroid plexuses (i.e. inlet flow sites), and the blue mesh is represents the outlet.

solves Navier-Stokes equations that contain a continuity and momentum equations. CSF is found to be incompressible Newtonian fluid with viscosity and density similar to water. The governing equations for CSF motion inside the ventricular domain are,

$$\vec{\nabla} \cdot \vec{u} = 0, \quad (1)$$

$$\rho \left(\frac{\partial \vec{u}}{\partial t} + (\vec{u} \cdot \vec{\nabla}) \vec{u} \right) = \nabla \cdot \vec{\sigma} + \rho \vec{f}. \quad (2)$$

ρ is CSF density, u is the velocity, p is the pressure and μ is the viscosity. The fluid production and drainage take place at the specified area for the choroid plexus (i.e., the area coloured in red in Figure 41) and the outlet is at the bottom of the third ventricle (i.e., coloured in blue in Figure 41). Although the choroid plexus mimics the real location and close to real shape, the outlet is the interface to the aqueduct connecting the third to the fourth ventricle.

Location	Weight <i>g</i>	Length <i>cm</i>	Thickness <i>cm</i>	Surface area <i>cm</i> ²	Flow rate <i>cm</i> ³ / <i>s</i>
All	2			5.714	0.0067
LV		8.61	0.5	4.305	0.005
3V		0.56	0.28	0.157	0.0018
4V		4.47	0.28	0.1252	0.0015

Table 24: Information about choroid plexus. The geometric specification of choroid plexus (i.e. length, thickness, surface area) are used to estimate the interventricular CSF production choroid plexus in each region of Lateral ventricles (LV), third ventricle (3V), and fourth ventricle (4V). [103, 16, 151]

The total fluid production (inlet flow rate) was set to a constant rate at 0.0058 ml/s. The choice of this measure is made by indirect calculation from medical observations (Table 24). Note that our findings in Chapter 4 described pulsation induced at inlet occurs via volumetric expansion of CP, not the CP production. In the current study, we have not accounted for this characteristic. The velocity at outlet is specified at zero gradient, and pressure at inlet and outlet are defined as zero gradient and zero, respectively. Boundaries of the ventricles are subjected to no-slip velocity and zero gradient pressure conditions.

6.3 Results and discussion

6.3.1 CSF flow characteristics

Reynolds number Re is a non-dimensionalised parameter widely used in fluid mechanics that provides insight about the flow characteristics. It measures the ratio between inertial forces and the viscous forces within a fluid and it is defined as $Re = Ul/\nu$, where U , l , and ν are characteristic velocity and length scales, and kinematic viscosity of the fluid, respectively. In general, defining this characteristic parameter in computational studies can be a straightforward practice, since the geometries are simple, i.e. a blood vessel can be modelled as a cylinder. However, in complex shaped organs such as ventricular system, defining the characteristic parameters is challenging and perhaps non-trivial. In this study, we compute the highest Reynolds number based on the local bulk velocity

magnitude and a diameter of the horn of the lateral ventricle (i.e. 2 cm), and the CSF kinematic viscosity was taken similar as water; the Reynolds number is found to be 0.5. This value suggests the flow to be Stokes (creeping) flow; a flow type in which the fluid particles follow the geometry's physical boundary, the inertial forces are negligible, and the viscous forces dominate.

The significance of the flow characteristic arises in revealing the transport pathways for micronutrients, waste, microswimmers, and drugs in the ventricular system, whether it enters from the CP or the ependymal cells lining the ventricles. Figure 42, illustrates the streamlines in the ventricular system, depicting the directionality of fluid particles from the source of production towards the outlet, while creeping along the boundary. It can be taken that the timescale for fluid particles to exit the ventricles depend on the location they are produced at. To elaborate further, points *A* and *B* are marked in the Figure 42 depicting the start point of fluid particles: particle entering from point *A* travels a shorter distance at higher velocity in comparison to particles initiating their movement from point *B*.

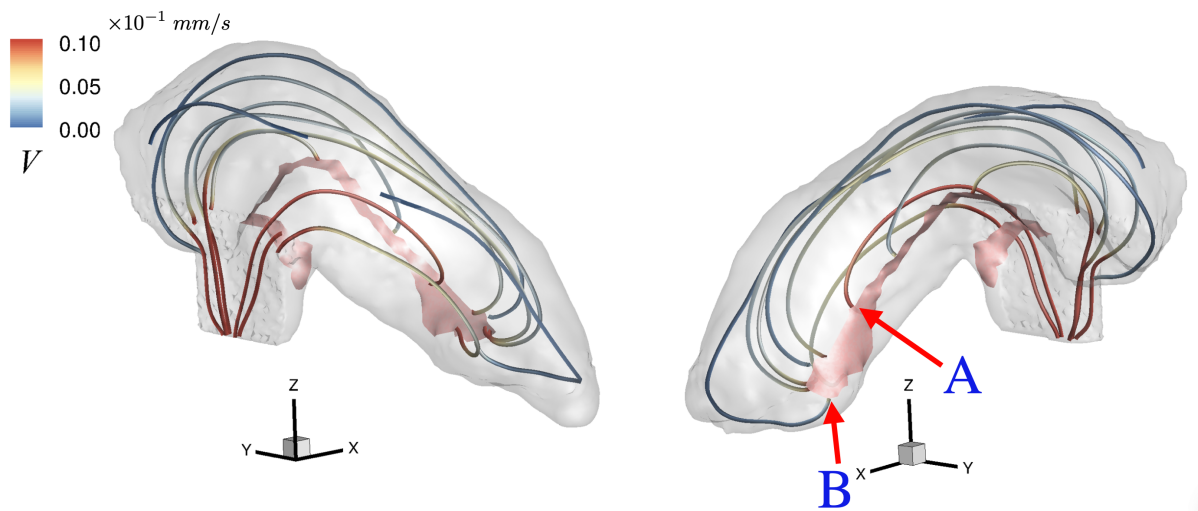


Figure 42: Streamlines illustrating the path that each particle travels from the production source (choroid plexus) to the outlet.

Another significance of the Stokes flow in ventricular system is its dependency on boundary conditions. In the current study, the CSF is produced at constant rate, similar to our

findings in Chapter 4. In the following chapter we confirmed that physiological changes can lead to alteration of average CSF production and its pulsatility. These alterations may affect the pathline of particles moving inside the ventricle. A study conducted by Sawamoto et.al confirms that the neuroblasts born in the subventricular zone migrate in parallel to the CSF flow to reach the olfactory bulb, where they are developed into new neurones [124]. Disturbance to the CSF flow will affect the neurogenesis process, which have been a hallmark in neurological disorders and neurodegenerative diseases. i.e. epilepsy, ischemic and traumatic brain injury [129].

6.3.2 Velocity field

Visualising the flow of CSF at different instants and locations is challenging given the complex shape of the ventricular system. Figure 43 shows the velocity magnitude distribution on sagittal, axial, and coronal planes. CSF momentum at the production site is the highest which decreases as the flow moves downstream, due to expansion of the geometrical space. However, it accelerates as it enters the third ventricle, which can be explained by conservation of mass.

An interesting feature of this flow distribution is the low fluid momentum at the frontal and posterior horns, which are shown in blue. The ependymal cells (i.e. the ventricular wall) of the two aforementioned areas are located in the frontal and occipital lobes of human brain (refer to Figure 39); these two brain lobes are responsible for executive functions such as cognitive skills, emotional expression, problem solving and visual perceptions. Therefore, we postulate disturbance of the fluid flow in these area may alter the brain functions.

The observation of the low fluid momentum also raises the question about the mechanisms by which particles (e.g. vitamins, growth factors, drugs, etc) are transported in the frontal and posterior horns. i.e. since the flow is almost stagnant, what mechanism causes the particle movements? We suggest the transport in these areas are facilitated by cilia movement.

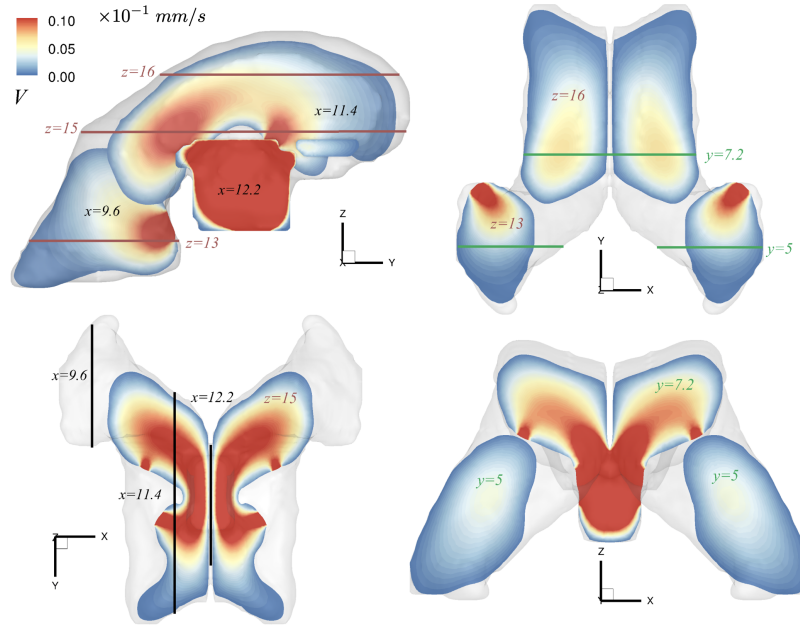


Figure 43: Velocity contours, top left: Sagittal plane, top right: Horizontal plane from bottom, bottom right: Horizontal plane from top, bottom left: coronal plane from the back. The figure is colour coded: red represents highest velocity and blue the lowest velocity.

6.3.3 Stress distribution

Ependymal cells lining the ventricular system are affected by mechanical forces induced by CSF flow. Two types of forces are normal stress (i.e., pressure) and shear stress. The former in medical science is the measure for intracranial pressure, ICP. It is examined for diagnosis of variety of neurological conditions such as intracranial bleeding, stroke, and aneurysm. It also contributes in stimulating cell proliferation and regeneration [59]. Figure 44 shows contours of pressure distribution on the boundaries of the ventricular system. It illustrates that the posterior horns experience the highest normal stress. The result explains the reason for the region being the first location to undergo ependymal cells failure, if subjected to increased pressure [154].

Our model shows the 3rd ventricle experiences the least pressure while exposed to the highest shear stress (figure 45). This mechanical stimulus has a vital role in the physiological behaviour; cells react to shear stress and modify their shape, cytoskeletal organisation, and adhesion properties of particles [104]. The latter is correlated with removal of debris from the ventricular system. Reduction in shear stress may lead to deposition

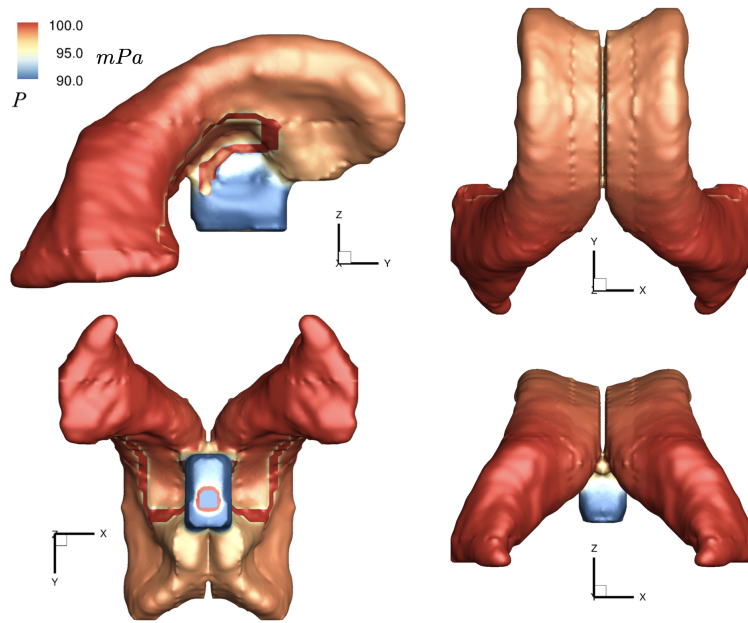


Figure 44: Pressure contours, top left: Sagittal plane, top right: Horizontal plane from bottom, bottom right: Horizontal plane from top, bottom left: coronal plane from the back. The figure is colour coded: red represents highest pressure and blue the lowest pressure.

of particles on the ventricular walls (more specifically in regions coloured in blue, parts of posterior and anterior horns). Recent studies have shown the accumulation of amyloid beta ($A\beta$) and tau protein, the two pathological hallmarks for diagnosis of AD, in SVZ at early stages of AD [71]. On the other hand, increased shear stress (regions coloured in red, FOM and 3V in our simulations) can cause abnormal ventricular cell shedding in the system. The degeneration and loss of ependymal cells are found to be a cause for ventricular expansion [161]. Additionally, we postulate the aforementioned areas may be the first locations to scar and bleed, which leads to blockage between the pathways.

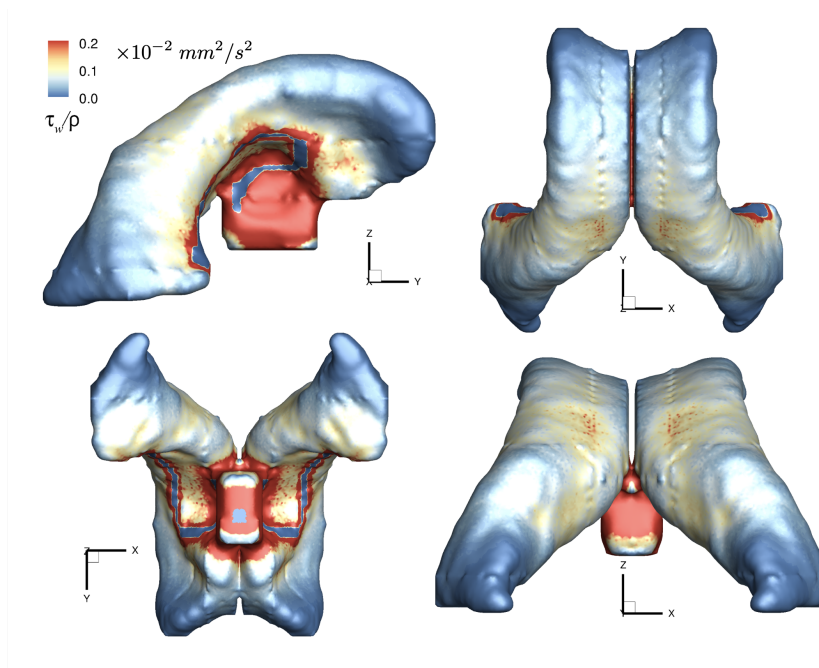


Figure 45: Shear stress contours, top left: Sagittal plane, top right: Horizontal plane from bottom, bottom right: Horizontal plane from top, bottom left: coronal plane from the back. The figure is colour coded: red represents highest Shear stress and blue the lowest Shear stress.

6.4 Chapter summary & future work

The 3D model presented in this chapter incorporates a real geometry of cerebral lateral and a portion of third ventricles as well as the location for the inlets, choroid plexus. The model provides a qualitative analysis on the normal flow pattern in the system and a baseline model for future investigations.

Our findings show, given the current boundary conditions, the flow resembles Stokes flow, creeping along the physical boundary to exit from the outlet. The highest velocity is at the production sites and the third ventricle, whereas the least fluid momentum is at the posterior horns. This part of the lateral ventricles experience the highest normal pressure: a finding that may explain the observation that in increased pressure condition, the first region that undergoes ependymal cells failure are posterior horns. The third ventricle is an area with the highest shear stress, therefore it is not surprising that increased in shear stress in the area may cause haemorrhage in the system.

One limitation of the current model is that it does not include all cerebral ventricles,

which must be considered. Additional studies must be conducted to better characterise the system in health and understand the mechanisms by which water and solutes (i.e. CSF) flow inside the ventricular system. Hence, one future study should incorporate the pulsation induced by the CP expansion (i.e. the result from chapter 4), and examine the importance of the new production signal against the current constant signals and evaluate its significance in CSF circulation. Please note that, in the current study, the boundary conditions were constant and time independent. However, integrating a pulsatile (i.e. time dependent) boundary condition will lead to time dependent flow, which can be characterised by computational studies. i.e. all variables, such as pressure and velocity, can be provided at every time instant of interest.

Other factors such as ventricular wall movement and ciliary beatings also must be studied, which are likely to be the most significant drivers. Studies, dispersedly and sparsely, have been conducted on these aspects, neglecting one against the other or focusing on a local behaviour of the flow. We propose that these mechanisms work in parallel to each other and all are important. i.e. although one may play a more significant role on the macro-scale flow than the others, another mechanism may be more effective in microscopic scales.

7 Contribution, Conclusion & Future Direction

The primary objective of this project was to advance our understanding of the cerebrospinal fluid (CSF) system, which has been largely neglected despite its potential relevance to the etiology of various neurological conditions that have long remained unresolved. A deeper understanding of this system would bring us one step closer to unraveling the underlying mechanisms of such conditions. Additionally, this knowledge could help improve current therapeutic approaches, such as the development of more advanced surgical tools, reduction of secondary side effects, and more accurate assessments of pharmacological treatments.

To achieve our main goal, we conducted a comprehensive literature review aimed at documenting and highlighting the contradictory views in the literature on all aspects of CSF dynamics, from its production to circulation and absorption. We identified the formation of incomplete conclusions as a primary reason for the limited understanding of brain function in both health and disease states. Thus, we consider our review a significant contribution to this field, providing clear direction towards fulfilling our ultimate aim.

Consequently, executing the knowledge gaps motivated us to make a bridge between biological and physical sciences, converting the latter into mathematical statements (Chapter 3). Hence, for the first time, we designed and developed a mathematical model representing the organ (i.e. choroid plexus) responsible for the direct production of CSF. The model is composed of all the main important elements in the organ, accounting for the characteristics of each sub-tissues including transports of water and solutes via their appropriate mechanisms. The model was solved using a collection of numerical techniques and the results were presented in Chapter 4. The current contribution of the model was to challenge the existing conjectures and find answers to the fundamental questions that were pending. e.g. evaluating the source of CSF pulsation at the choroid plexus, the importance of accounting for properties of tissues.

The model also provided a framework for examining the tissue under various conditions. In the current study (chapter 5), we examined the effect of normal ageing on the tissue and described their impact on the dynamic of the system and explained the possible relation to the development of neurological disorders. In addition, this system can indi-

vidually and collectively examine the impact of ageing sub-organs (e.g. membranes, cells) on the dynamic of the system. i.e. the impact of stiffened cells on CSF production. This capability of the system has the benefit of identifying and examining the most important characteristics of the sub-organs (i.e. dehydration of membranes versus cell atrophy on capillary morphology). This will also lead to the elimination of a few conjectures (i.e. dehydration of endothelial cells is more likely to alter CSF production than its stiffening due to ageing). Therefore, this is not only providing us with valuable data towards finding aetiologies of conditions but also directs scientists to the element they should target. In chapter 6, we diverged from our focus on CSF production and delved into investigating CSF circulation. Our objective was to characterise the flow field of CSF in a realistic geometry of the lateral and part of the third ventricles while maintaining a constant rate of CSF production. Our analysis shed light on several clinical observations, such as the fact that the posterior horns of lateral ventricles are the first region to experience failure of ependymal cells when CSF pressure increases. Our model serves as a visualisation tool, demonstrating that even under normal conditions, the posterior horns experience the highest normal stress (pressure), and increased pressure in the entire system may exceed the threshold limits of these regions they should target.

It is worth noting that chapters 4-6, which include the numerical investigations, were written with the purpose that a reader could refer to each as independent and complete chapters. The reason for such an outline is that the focus of chapters 4 and 5 was on CSF production and chapter 6 discusses CSF circulation. Hence, the future work for each was included in the final sections of each chapter and will not be discussed here. However, in this section, we discuss the future work for the overall system (i.e. production and circulation), counting the system as one. This is done to bring to the reader's attention a few possible clinical applications of this system, which will be discussed below. However, we acknowledge the roadmap to achieving these goals requires extensive knowledge of several disciplines such as radiology, pharmacy, and pharmacology, as well as fluid and solid mechanics.

Accounting for the future works discussed in chapters 4 and 6 as well as improving both models (i.e. mathematical model and 3D simulation) accordingly, the dynamic of the system can be studied and characterised in health. In other words, extracting a realistic

inlet condition from the mathematical model (chapter 4) as well as a realistic boundary condition adopted from the 3D model (chapter 6), can provide benchmark data for assessing the system for different purposes.

One potential clinical application of the system is in predicting the fluid flow and possible flow complications in the system after surgical treatments. e.g. implementing a shunt. One main advantage of this approach is that it can be patient-specific via the implementation of a real ventricular geometry as well as the intended use of treatment. e.g. adding a shunt to the system. Other advantages of developing such tools is the relatively low cost in comparison to experimental studies as well as their low risk.

Another practical use of such a system will be for assessing the drug transport targeting certain areas of the brain. CSF domain provides a unique conduit with the potential to play a novel role in transporting drugs into the brain since 1) the cerebrospinal fluid is essentially a product of blood, 2) the domain is lined up by epithelial cells with no tight junction, which allows for the exchange of solutes and drugs to the underlying tissue and even inaccessible areas, 3) it covers a wide area of the human body (i.e. from frontal to the posterior lobes of the brain and cranial to caudal (spinal cord)). Therefore, drugs transported from blood to ventricles can be convected by CSF flow to various regions such as periventricular targets such as the hippocampus and hypothalamus. To fulfil this purpose, the developed mathematical can be modified to include a potential agent in the blood and its transport across the CP can be examined. The results from this exercise can be implemented as inlet conditions in the 3D simulations to evaluate the drug transport in the system (e.g. Lateral ventricles).

Appendices

Appendix A: Is the steady flow assumption valid?

A multi-compartment model (here called M1) of the intracranial dynamics was previously developed in our research group (final-year-project) which is similar to the model of Linninger et al. [86]. In this model all categorically similar types of blood vessels (e.g. arteries) were lumped into a single cylindrical compartment and the physical parameters were set in a way to mimic the physics of the flow, i.e. resistance, flow rate, and elasticity. For each compartment, a simplified mass (similar to Equation 2) and momentum conservation (similar to Equation 14) laws as well as a distensibility equation (i.e. $\Delta p = E(\frac{A}{A_0} - 1)$, E : elasticity, A_0 : area at rest) were adopted. M1 couples the three governing equations in order to solve for the pressure, the flow rate, and the cross-sectional area. There were additional auxiliary equations to close the system of equations, such as equations representing the flow that leaves a compartment and enters another one.

In the following year, M2 was developed by our group (MSc dissertation) in order to question the steady state assumption in the momentum equation. To this end, an additional unsteady term was added to the momentum balance as,

$$\Delta p = \frac{8\pi\mu l}{A^2} Q_{in} + \frac{\rho l}{A} \left(\frac{\partial Q}{\partial t} \right). \quad (3)$$

A third models (M3) was also developed (MSc dissertation) to question the parabolic profile assumption of the momentum equation. Such drawback can be rectified by the Fry solution for pulsatile flows in pipes [46]. The solution is given in frequency domain and by the Fourier modes. Therefore, all equations were transferred and the resultant governing equations in each mode k out of the maximum number of considered modes N became

$$A_k \left[\frac{1}{\Delta t} \left(1 - e^{-\frac{2\pi j(k-1)}{N}} \right) \right] = Q_{in_k} - Q_{out_k}. \quad (4)$$

for the mass conservation,

$$\frac{1}{l} \Delta p_k = \left[\frac{\rho}{A_0} \frac{C_u}{\Delta t} \left(1 - e^{-\frac{2\pi j(k-1)}{N}} \right) + C_v \frac{8\pi\mu}{A_0^2} \right] Q_{in_k}. \quad (5)$$

for the momentum equation, and

$$P_{lumen_k} - P_{surrounding_k} = \left(\frac{E}{A_0} A_k - E \delta_{1k} \right). \quad (6)$$

for the distensibility closure. In Equations 4 to 6 , subscript k represents the amplitude of that variable in the mode k . C_u and C_v are the constants provided by the Fry solution, and δ_{1k} is the Kronecker delta function.

Solving the holistic system of equations, involving 20 compartments, with M1, M2, and

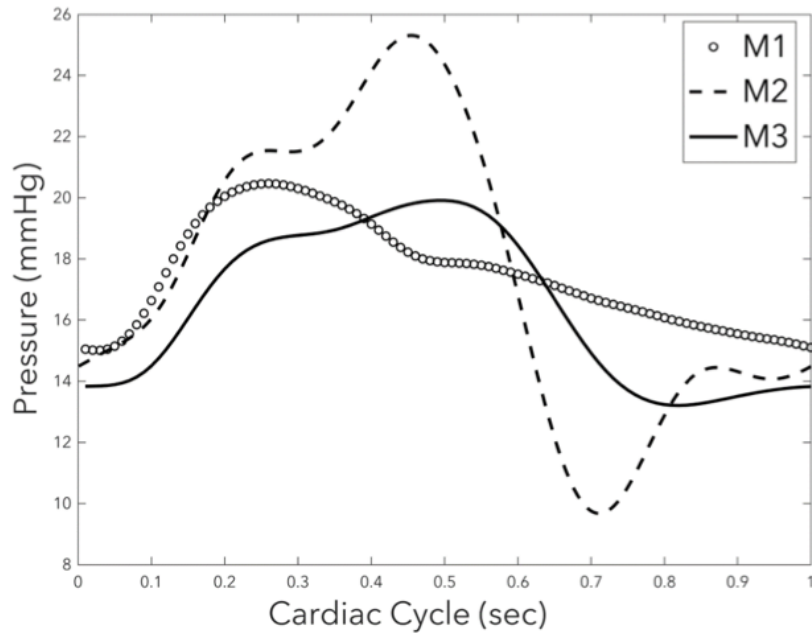


Figure 46: Time dependant pressure signal in the capillary obtained from M1 (circle symbols), M2 (dashed line) and M3 (solid line).

M3 models, provided a valuable insight on the importance of two major assumptions in the original model M1. Figure 46 compares the pressure waveform in the cerebral capillary, which is of interest in the current project, obtained from M1 (circle symbols), M2 (dashed line), and M3 (solid line). Pressure signal in M1 shows that the pressure rises for a quarter of the cardiac cycle where it reaches a maximum and then decreases. However, the characteristic of this signal changes by including the unsteady term (i.e. M2): the pressure signal increases for a quarter of the cardiac cycle (similar to M1), it reaches a plateau for a short time, after which it continues to rise and reaches a second peak. Then the pressure is followed by a rapid fall and presents a minimum before rising

again. Note that all amplitudes are magnified and the main one is shifted. A more realistic representation of the resistance in M3 illustrates a similar characteristic for pressure signal as in M2, with one main difference: the amplitudes are all dampened. The flowrates at

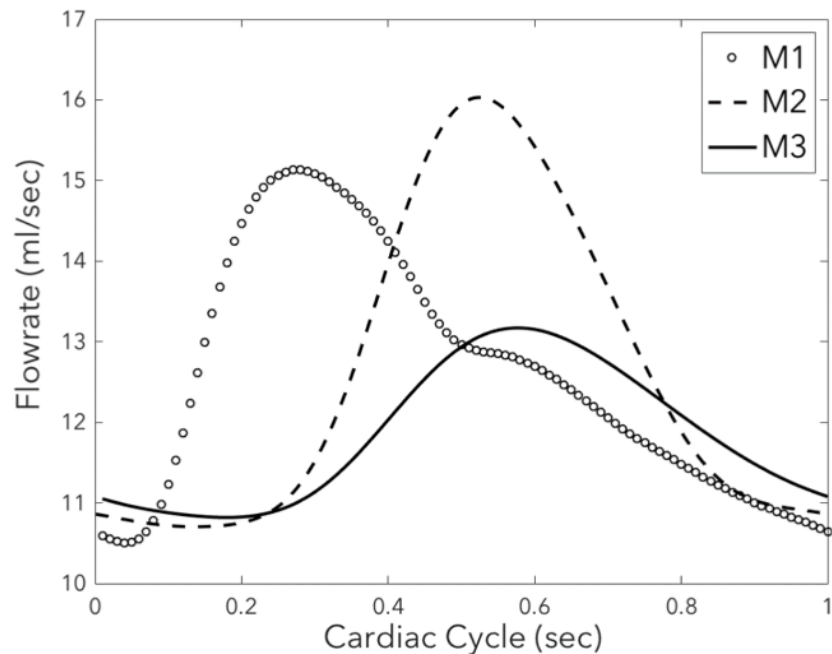


Figure 47: Comparing the solutions of flow rate in capillary obtained from M1 (circle symbols), M2 (dashed line) and M3 (solid line).

capillary level, on the other hand, present a similar characteristic when obtained from the three models (Figure 47): the flowrates in all increase, reach a maximum, then decrease. However, these events occur with different intensity at different locations. In other words, comparing M1 and M2 shows that addition of the unsteady term in M2 increased the pulsatility and shifted the location of the extrema, whereas the waveform in M3 (solid lines) represent a significant decrease in the pulsatility.

In conclusion, among these three models, M3 provides the most realistic solution of the flow in the vasculature system due to the fact that its governing equations carry less assumptions. Subsequently, the next best models are M2 and M1, respectively.

Appendix B:Table of Variables

1	<i>A</i> Cap	46	<i>C</i> vent_HCO3	91	<i>J</i> BLM_Glo	137	<i>J</i> APM_UrAc
2	<i>A</i> St	47	<i>C</i> vent_Glu	92	<i>J</i> BLM_Fib	138	<i>J</i> APM_Ur
3	<i>A</i> vent	48	<i>C</i> vent_K	93	<i>J</i> BLM_Cl	139	<i>J</i> APM_Po
4	<i>A</i> CPE	49	<i>C</i> vent_Mg	94	<i>J</i> BLM_chol	140	<i>J</i> APM_H
		50	<i>C</i> vent_Lac	95	<i>J</i> BLM_Na		
5	<i>C</i> Cap_out_AlB	51	<i>C</i> vent_AmAc	96	<i>J</i> BLM_calc	141	<i>Q</i> Cap_in
6	<i>C</i> Cap_out_Glo	52	<i>C</i> vent_UrAc	97	<i>J</i> BLM_HCO3	142	<i>Q</i> Cap_out
7	<i>C</i> Cap_out_Fib	53	<i>C</i> vent_Ur	98	<i>J</i> BLM_Glu	143	<i>Q</i> EC
8	<i>C</i> Cap_out_Cl	54	<i>C</i> vent_Po	99	<i>J</i> BLM_K	144	<i>Q</i> BLM
9	<i>C</i> Cap_out_ChOl	55	<i>C</i> vent_H	100	<i>J</i> BLM_Mg	145	<i>Q</i> TJ
10	<i>C</i> Cap_out_Na			101	<i>J</i> BLM_Lac	146	<i>Q</i> APM
11	<i>C</i> Cap_out_Calc	56	<i>C</i> CPE_AlB	102	<i>J</i> BLM_AmAc	147	<i>Q</i> vent_out
12	<i>C</i> Cap_out_HCO3	57	<i>C</i> CPE_Glo	103	<i>J</i> BLM_UrAc		
13	<i>C</i> Cap_out_Glu	58	<i>C</i> CPE_Fib	104	<i>J</i> BLM_Ur	148	<i>P</i> St_out
14	<i>C</i> Cap_out_K	59	<i>C</i> CPE_Cl	105	<i>J</i> BLM_PO	149	<i>P</i> St_in
15	<i>C</i> Cap_out_Mg	60	<i>C</i> CPE_ChOl	106	<i>J</i> BLM_H	150	<i>P</i> St_BLM
16	<i>C</i> Cap_out_Lac	61	<i>C</i> CPE_Na			151	<i>P</i> APM
17	<i>C</i> Cap_out_AmAc	62	<i>C</i> CPE_Calc	107	<i>J</i> TJ_AlB		
18	<i>C</i> Cap_out_UrAc	63	<i>C</i> CPE_HCO3	108	<i>J</i> TJ_Glo	152	<i>R</i> EC
19	<i>C</i> Cap_out_Ur	64	<i>C</i> CPE_Glu	109	<i>J</i> TJ_Fib	153	<i>R</i> BLM
20	<i>C</i> Cap_out_Po	65	<i>C</i> CPE_K	110	<i>J</i> TJ_Cl	154	<i>R</i> APM
21	<i>C</i> Cap_out_H	66	<i>C</i> CPE_Mg	111	<i>J</i> TJ_chol		
		67	<i>C</i> CPE_Lac	112	<i>J</i> TJ_Na	155	<i>B</i> EC
22	<i>C</i> St_AlB	68	<i>C</i> CPE_AmAc	113	<i>J</i> TJ_Calc	156	<i>B</i> BLM
23	<i>C</i> St_Glo	69	<i>C</i> CPE_UrAc	114	<i>J</i> TJ_HCO3	157	<i>B</i> APM
24	<i>C</i> St_Fib	70	<i>C</i> CPE_Ur	115	<i>J</i> TJ_Glu		
25	<i>C</i> St_Cl	71	<i>C</i> CPE_Po	116	<i>J</i> TJ_K	158	<i>J</i> buff
26	<i>C</i> St_ChOl	72	<i>C</i> CPE_H	117	<i>J</i> TJ_Mg	159	<i>J</i> KCC
27	<i>C</i> St_Na			118	<i>J</i> TJ_Lac	160	<i>J</i> NBCN1
28	<i>C</i> St_Calc	73	<i>J</i> EC_AlB	119	<i>J</i> TJ_AmAc	161	<i>J</i> NcBE
29	<i>C</i> St_HCO3	74	<i>J</i> EC_Glo	120	<i>J</i> TJ_UrAc	162	<i>J</i> AE1
30	<i>C</i> St_Glu	75	<i>J</i> EC_Fib	121	<i>J</i> TJ_Ur		
31	<i>C</i> St_K	76	<i>J</i> EC_Cl	122	<i>J</i> TJ_PO	163	<i>J</i> ATP
32	<i>C</i> St_Mg	77	<i>J</i> EC_ChOl	123	<i>J</i> TJ_H	164	<i>R</i> Na
33	<i>C</i> St_Lac	78	<i>J</i> EC_Na			165	<i>R</i> K
34	<i>C</i> St_AmAc	79	<i>J</i> EC_Calc	124	<i>J</i> APM_AlB	166	<i>J</i> KCC4
35	<i>C</i> St_UrAc	80	<i>J</i> EC_HCO3	125	<i>J</i> APM_Glo	167	<i>J</i> NKCC1
36	<i>C</i> St_Ur	81	<i>J</i> EC_Glu	126	<i>J</i> APM_Fib	168	<i>J</i> NBCN1
37	<i>C</i> St_Po	82	<i>J</i> EC_K	127	<i>J</i> APM_Cl	169	<i>J</i> NHE
38	<i>C</i> St_H	83	<i>J</i> EC_Mg	128	<i>J</i> APM_chol	170	<i>J</i> ch_cl
		84	<i>J</i> EC_Lac	129	<i>J</i> APM_Na	171	<i>J</i> ch_k
39	<i>C</i> vent_AlB	85	<i>J</i> EC_AmAc	130	<i>J</i> APM_Calc		
40	<i>C</i> vent_Glo	86	<i>J</i> EC_UrAc	131	<i>J</i> APM_HCO3		
41	<i>C</i> vent_Fib	87	<i>J</i> EC_Ur	132	<i>J</i> APM_Glu		
42	<i>C</i> vent_Cl	88	<i>J</i> EC_Po	133	<i>J</i> APM_K		
43	<i>C</i> vent_ChOl	89	<i>J</i> EC_H	134	<i>J</i> APM_Mg		
44	<i>C</i> vent_Na	90	<i>J</i> BLM_AlB	135	<i>J</i> APM_Lac		

References

- [1] Types of capillaries: Continuous, fenestrated & sinusoidal. *Study.com*, 2020.
- [2] Alzahra J Al Omran, Hannah C Saternos, Yusuf S Althobaiti, Alexander Wisner, Youssef Sari, Surya M Nauli, and Wissam A AbouAlaiwi. Alcohol consumption impairs the ependymal cilia motility in the brain ventricles. *Scientific reports*, 7(1):1–8, 2017.
- [3] STEVEN M Albelda, PHYLLIS M Sampson, FREDERICK R Haselton, JM McNiff, SN Mueller, SK Williams, AP Fishman, and EM Levine. Permeability characteristics of cultured endothelial cell monolayers. *Journal of Applied Physiology*, 64(1):308–322, 1988.
- [4] Arturo Alvarez-Buylla and Jose Manuel Garcia-Verdugo. Neurogenesis in adult subventricular zone. *Journal of Neuroscience*, 22(3):629–634, 2002.
- [5] John L Anderson. Configurational effect on the reflection coefficient for rigid solutes in capillary pores. *Journal of Theoretical Biology*, 90(3):405–426, 1981.
- [6] AW Asscher and J Henry Jones. Capillary permeability to plasma proteins. *Postgraduate Medical Journal*, 41(477):425, 1965.
- [7] TM Babik. Morphometric characteristics of epitheliocytes in the choroid plexus of the cerebral ventricles in humans during aging. *Neuroscience and Behavioral Physiology*, 37(2):107–109, 2007.
- [8] Erik NTP Bakker, Brian J Bacskai, Michal Arbel-Ornath, Roxana Aldea, Beatrice Bedussi, Alan WJ Morris, Roy O Weller, and Roxana O Carare. Lymphatic clearance of the brain: perivascular, paravascular and significance for neurodegenerative diseases. *Cellular and molecular neurobiology*, 36(2):181–194, 2016.
- [9] Sriram Balusu, Marjana Brkic, Claude Libert, and Roosmarijn E Vandenbroucke. The choroid plexus-cerebrospinal fluid interface in alzheimer’s disease: more than just a barrier. *Neural regeneration research*, 11(4):534, 2016.

- [10] SI Barry and M Holmes. Asymptotic behaviour of thin poroelastic layers. *IMA journal of applied mathematics*, 66(2):175–194, 2001.
- [11] Dominique Barthes-Biesel. Motion and deformation of elastic capsules and vesicles in flow. *Annual Review of fluid mechanics*, 48:25–52, 2016.
- [12] Marvin Bergsneider. Evolving concepts of cerebrospinal fluid physiology. *Neurosurgery Clinics*, 12(4):631–638, 2001.
- [13] Steven William Bothwell, Damir Janigro, and Adjanie Patabendige. Cerebrospinal fluid dynamics and intracranial pressure elevation in neurological diseases. *Fluids and Barriers of the CNS*, 16(1):9, 2019.
- [14] Thomas Brinker, Edward Stopa, John Morrison, and Petra Klinge. A new look at cerebrospinal fluid circulation. *Fluids and Barriers of the CNS*, 11(1):10, 2014.
- [15] Chris Brown, Amy Weist, Aisha Heath, and Amanda Garzon. New year! *Southerly*, 69(3):122–123, 2009.
- [16] PD Brown, SL Davies, T Speake, and ID Millar. Molecular mechanisms of cerebrospinal fluid production. *Neuroscience*, 129(4):955–968, 2004.
- [17] Joel Buishas, Ian G Gould, and Andreas A Linninger. A computational model of cerebrospinal fluid production and reabsorption driven by starling forces. *Croatian medical journal*, 55(5):481–497, 2014.
- [18] Marin Bulat and Marijan Klarica. Recent insights into a new hydrodynamics of the cerebrospinal fluid. *Brain research reviews*, 65(2):99–112, 2011.
- [19] Paulo S Caceres, Ignacio Benedicto, Guillermo L Lehmann, and Enrique J Rodriguez-Boulan. Directional fluid transport across organ–blood barriers: Physiology and cell biology. *Cold Spring Harbor perspectives in biology*, 9(3):a027847, 2017.
- [20] Michael Chan and Sepideh Amin-Hanjani. Cerebrospinal fluid and its abnormalities. *e LS*, 2001.

- [21] Thomas C Chen. Delivery considerations for targeting the choroid plexus–cerebrospinal fluid route. In *The Choroid Plexus and Cerebrospinal Fluid*, pages 155–165. Elsevier, 2016.
- [22] S Cheng, E Jacobson, and LE Bilston. Models of the pulsatile hydrodynamics of cerebrospinal fluid flow in the normal and abnormal intracranial system. *Computer methods in biomechanics and biomedical engineering*, 10(2):151–157, 2007.
- [23] Jong Duck Choi, Yeonsil Moon, Hee-Jin Kim, Younghee Yim, Subin Lee, and Won-Jin Moon. Choroid plexus volume and permeability at brain mri within the alzheimer disease clinical spectrum. *Radiology*, page 212400, 2022.
- [24] Dean Chou, John C Vardakis, and Yiannis Ventikos. Multiscale modelling for cerebrospinal fluid dynamics: Multicompartmental poroelasticity and the role of aqp4. *Journal of Biosciences and Medicines*, 2(2):1–9, 2014.
- [25] Henriette L Christensen, Dagne Barbuskaite, Aleksandra Rojek, Hans Malte, Inga B Christensen, Annette C Füchtbauer, Ernst-Martin Füchtbauer, Tobias Wang, Jeppe Praetorius, and Helle H Damkier. The choroid plexus sodium-bicarbonate cotransporter nbce2 regulates mouse cerebrospinal fluid ph. *The Journal of physiology*, 596(19):4709–4728, 2018.
- [26] Marilyn J Cipolla. The cerebral circulation. *Integrated systems physiology: From molecule to function*, 1(1):1–59, 2009.
- [27] M Coloma, JD Schaffer, RO Carare, PR Chiarot, and P Huang. Pulsations with reflected boundary waves: a hydrodynamic reverse transport mechanism for perivascular drainage in the brain. *Journal of mathematical biology*, 73(2):469–490, 2016.
- [28] Helle H Damkier, Peter D Brown, and Jeppe Praetorius. Cerebrospinal fluid secretion by the choroid plexus. *Physiological reviews*, 93(4):1847–1892, 2013.
- [29] Walter E Dandy and Kenneth D Blackfan. An experimental and clinical study of internal hydrocephalus. *Journal of the American Medical Association*, 61(25):2216–2217, 1913.

- [30] Jacques de Rougemont, Adelbert Ames III, Frances B Nesbett, and Helmut F Hofmann. Fluid formed by choroid plexus: A technique for its collection and a comparison of its electrolyte composition with serum and cisternal fluids. *Journal of neurophysiology*, 23(5):485–495, 1960.
- [31] Xiaowei Dong. Current strategies for brain drug delivery. *Theranostics*, 8(6):1481, 2018.
- [32] Frank J Dowd, Bart Johnson, and Angelo Mariotti. *Pharmacology and Therapeutics for Dentistry-E-Book*. Elsevier Health Sciences, 2016.
- [33] GH Du Boulay. Pulsatile movements in the csf pathways. *The British journal of radiology*, 39(460):255–262, 1966.
- [34] Mariia Dvoriashyna, Alexander JE Foss, Eamonn A Gaffney, Oliver E Jensen, and Rodolfo Repetto. Osmotic and electroosmotic fluid transport across the retinal pigment epithelium: A mathematical model. *Journal of theoretical biology*, 456:233–248, 2018.
- [35] Mariia Dvoriashyna, Alexander JE Foss, Eamonn A Gaffney, and Rodolfo Repetto. Fluid and solute transport across the retinal pigment epithelium: a theoretical model. *Journal of the Royal Society Interface*, 17(163):20190735, 2020.
- [36] Karen L Edelblum and Jerrold R Turner. Epithelial cells: Structure, transport, and barrier function. In *Mucosal Immunology*, pages 187–210. Elsevier, 2015.
- [37] Antigoni Ekonomou, SH Cedar, Clive G Ballard, and Stephen L Minger. Stem-cells: Prospects for treating dementia. *British Journal of Neuroscience Nursing*, 4(5):220–222, 2008.
- [38] Larry D Faller. Mechanistic studies of sodium pump. *Archives of Biochemistry and Biophysics*, 476(1):12–21, 2008.
- [39] David A Feinberg and Alexander S Mark. Human brain motion and cerebrospinal fluid circulation demonstrated with mr velocity imaging. *Radiology*, 163(3):793–799, 1987.

- [40] Latha Ganti. External ventricular drain placement. In *Atlas of Emergency Medicine Procedures*, pages 241–245. Springer, 2016.
- [41] Joseph E Gaugler, Haya Ascher-Svanum, David L Roth, Tolulope Fafowora, Andrew Siderowf, and Thomas G Beach. Characteristics of patients misdiagnosed with alzheimer’s disease and their medication use: an analysis of the nacc-uds database. *BMC geriatrics*, 13(1):1–10, 2013.
- [42] Seifollah Gholampour. Fsi simulation of csf hydrodynamic changes in a large population of non-communicating hydrocephalus patients during treatment process with regard to their clinical symptoms. *PloS one*, 13(4), 2018.
- [43] I Gonzalez-Marrero, LG Hernandez-Abad, L Castaneyra-Ruiz, EM Carmona-Calero, and A Castaneyra-Perdomo. Changes in the choroid plexuses and brain barriers associated with high blood pressure and ageing. *Neurología (English Edition)*, 2020.
- [44] Ibrahim González-Marrero, Lydia Giménez-Llort, Conrad E Johanson, Emilia María Carmona-Calero, Leandro Castañeyra-Ruiz, José Miguel Brito-Armas, Agustín Castañeyra-Perdomo, and Rafael Castro-Fuentes. Choroid plexus dysfunction impairs beta-amyloid clearance in a triple transgenic mouse model of alzheimer’s disease. *Frontiers in cellular neuroscience*, 9:17, 2015.
- [45] Joan Goverman. Autoimmune t cell responses in the central nervous system. *Nature Reviews Immunology*, 9(6):393–407, 2009.
- [46] Joseph C Greenfield Jr and Donald L Fry. Relationship between instantaneous aortic flow and the pressure gradient. *Circulation research*, 17(4):340–348, 1965.
- [47] Liwei Guo, John C Vardakis, Toni Lassila, Micaela Mitolo, Nishant Ravikumar, Dean Chou, Matthias Lange, Ali Sarrami-Foroushani, Brett J Tully, Zeike A Taylor, et al. Subject-specific multi-poroelastic model for exploring the risk factors associated with the early stages of alzheimer’s disease. *Interface focus*, 8(1):20170019, 2018.

- [48] Sumeet Gupta, Michaela Soellinger, Peter Boesiger, Dimos Poulidakos, and Vartan Kurtcuoglu. Three-dimensional computational modeling of subject-specific cerebrospinal fluid flow in the subarachnoid space. *Journal of biomechanical engineering*, 131(2), 2009.
- [49] Andrew R Harris, Loic Peter, Julien Bellis, Buzz Baum, Alexandre J Kabla, and Guillaume T Charras. Characterizing the mechanics of cultured cell monolayers. *Proceedings of the National Academy of Sciences*, 109(41):16449–16454, 2012.
- [50] GEORGE B HASSIN, ERIC OLDBERG, and MILTON TINSLEY. Changes in the brain in plexectomized dogs: with comments on the cerebrospinal fluid. *Archives of Neurology & Psychiatry*, 38(6):1224–1239, 1937.
- [51] Stephen B Hladky and Margery A Barrand. Mechanisms of fluid movement into, through and out of the brain: evaluation of the evidence. *Fluids and Barriers of the CNS*, 11(1):26, 2014.
- [52] Stephen B Hladky and Margery A Barrand. Fluid and ion transfer across the blood–brain and blood–cerebrospinal fluid barriers; a comparative account of mechanisms and roles. *Fluids and Barriers of the CNS*, 13(1):19, 2016.
- [53] L Howden, D Giddings, H Power, A Aroussi, M Vloeberghs, M Garnett, and D Walker. Three-dimensional cerebrospinal fluid flow within the human ventricular system. *Computer methods in biomechanics and biomedical engineering*, 11(2):123–133, 2008.
- [54] Violaine Hubert, Fabien Chauveau, Chloé Dumot, Elodie Ong, Lise-Prune Berner, Emmanuelle Canet-Soulas, Jean-François Ghersi-Egea, and Marlène Wiart. Clinical imaging of choroid plexus in health and in brain disorders: a mini-review. *Frontiers in molecular neuroscience*, 12:34, 2019.
- [55] Ronald E Huss and Donald J Marsh. A model of nacl and water flow through paracellular pathways of renal proximal tubules. *The Journal of membrane biology*, 23(1):305–347, 1975.

- [56] Ronald E Huss and John L Stephenson. A mathematical model of proximal tubule absorption. *The Journal of Membrane Biology*, 47(4):377–399, 1979.
- [57] James C Iatridis, Junru Wu, Jason A Yandow, and Helene M Langevin. Subcutaneous tissue mechanical behavior is linear and viscoelastic under uniaxial tension. *Connective tissue research*, 44(5):208–217, 2003.
- [58] Sebastian Illes. More than a drainage fluid: the role of csf in signaling in the brain and other effects on brain tissue. *Handbook of Clinical Neurology*, 146:33–46, 2018.
- [59] Antonio J Jiménez, María-Dolores Domínguez-Pinos, María M Guerra, Pedro Fernández-Llebrez, and José-Manuel Pérez-Fígares. Structure and function of the ependymal barrier and diseases associated with ependyma disruption. *Tissue barriers*, 2(1):e28426, 2014.
- [60] Conrad Johanson, Paul McMillan, Rosemarie Tavares, Anthony Spangenberg, John Duncan, Gerald Silverberg, and Edward Stopa. Homeostatic capabilities of the choroid plexus epithelium in alzheimer’s disease. *Cerebrospinal Fluid Research*, 1(1):1–16, 2004.
- [61] Conrad E Johanson, John A Duncan, Petra M Klinge, Thomas Brinker, Edward G Stopa, and Gerald D Silverberg. Multiplicity of cerebrospinal fluid functions: new challenges in health and disease. *Cerebrospinal fluid research*, 5(1):1–32, 2008.
- [62] Conrad E Johanson, John A Duncan, Edward G Stopa, and Andrew Baird. Enhanced prospects for drug delivery and brain targeting by the choroid plexus–csf route. *Pharmaceutical research*, 22(7):1011–1037, 2005.
- [63] Conrad E Johanson and Nancy L Johanson. Choroid plexus blood-csf barrier: major player in brain disease modeling and neuromedicine. *Journal of Neurology & Neuromedicine*, 3(4), 2018.
- [64] Conrad E Johanson, Edward G Stopa, and Paul N McMillan. The blood–cerebrospinal fluid barrier: structure and functional significance. *The blood-brain and other neural barriers*, pages 101–131, 2011.

- [65] Ian Johnston and Charles Teo. Disorders of csf hydrodynamics. *Child's nervous system*, 16(10-11):776–799, 2000.
- [66] IL Jones, M Warner, and JD Stevens. Mathematical modelling of the elastic properties of retina: a determination of young's modulus. *Eye*, 6(6):556–559, 1992.
- [67] William H Karasov. Integrative physiology of transcellular and paracellular intestinal absorption. *Journal of Experimental Biology*, 220(14):2495–2501, 2017.
- [68] Morris J Karnovsky. The ultrastructural basis of transcapillary exchanges. *The Journal of general physiology*, 52(1):64–95, 1968.
- [69] Charanjit Kaur, Gurugirijha Rathnasamy, and Eng-Ang Ling. The choroid plexus in healthy and diseased brain. *Journal of Neuropathology & Experimental Neurology*, 75(3):198–213, 2016.
- [70] Ahmad H Khasawneh, Richard J Garling, and Carolyn A Harris. Cerebrospinal fluid circulation: what do we know and how do we know it? *Brain circulation*, 4(1):14, 2018.
- [71] Hyeon Soo Kim, Seong Min Shin, Sujin Kim, Yunkwon Nam, Anji Yoo, and Minho Moon. Relationship between adult subventricular neurogenesis and alzheimer's disease: Pathologic roles and therapeutic implications. *Frontiers in Aging Neuroscience*, 14, 2022.
- [72] Marijan Klarica, Milan Radoš, Gorislav Erceg, Antonio Petošić, Ivana Jurjević, and Darko Orešković. The influence of body position on cerebrospinal fluid pressure gradient and movement in cats with normal and impaired craniospinal communication. *PLoS One*, 9(4), 2014.
- [73] Lena Koh, Andrei Zakharov, and Miles Johnston. Integration of the subarachnoid space and lymphatics: is it time to embrace a new concept of cerebrospinal fluid absorption? *Cerebrospinal fluid research*, 2(1):6, 2005.

- [74] Agnieszka Krzyzanowska and Eva Carro. Pathological alteration in the choroid plexus of alzheimer’s disease: implication for new therapy approaches. *Frontiers in pharmacology*, 3:75, 2012.
- [75] Vartan Kurtcuoglu, Michaela Soellinger, Paul Summers, Kevin Boomsma, Dimos Poulidakos, Peter Boesiger, and Yiannis Ventikos. Computational investigation of subject-specific cerebrospinal fluid flow in the third ventricle and aqueduct of sylvius. *Journal of biomechanics*, 40(6):1235–1245, 2007.
- [76] Peter R Kviety. The gastrointestinal circulation. 2010.
- [77] C Lapras, P Mertens, JN Guilburd, J Pialat, and JD Patet. Choroid plexectomy for the treatment of chronic infected hydrocephalus. *Child’s Nervous System*, 4(3):139–142, 1988.
- [78] Erik Hviid Larsen, Jakob Balslev Sørensen, and Jens Nørkaer Sørensen. Analysis of the sodium recirculation theory of solute-coupled water transport in small intestine. *The Journal of physiology*, 542(1):33–50, 2002.
- [79] Anita T Layton and Sarah D Olson. *Biological Fluid Dynamics: Modeling, Computations, and Applications*. American Mathematical Society, 1900.
- [80] Dongun Lee and Jeong Hee Hong. The fundamental role of bicarbonate transporters and associated carbonic anhydrase enzymes in maintaining ion and ph homeostasis in non-secretory organs. *International Journal of Molecular Sciences*, 21(1):339, 2020.
- [81] Ellen Lee, JZ Wang, and Reuben Mezrich. Variation of lateral ventricular volume during the cardiac cycle observed by mr imaging. *American journal of neuroradiology*, 10(6):1145–1149, 1989.
- [82] Shane A Liddelow. Development of the choroid plexus and blood-csf barrier. *Frontiers in neuroscience*, 9:32, 2015.

- [83] Andreas A Linninger, Brian Sweetman, and Richard Penn. Normal and hydrocephalic brain dynamics: the role of reduced cerebrospinal fluid reabsorption in ventricular enlargement. *Annals of biomedical engineering*, 37(7):1434–1447, 2009.
- [84] Andreas A Linninger, Kevin Tangen, Chih-Yang Hsu, and David Frim. Cerebrospinal fluid mechanics and its coupling to cerebrovascular dynamics. *Annual Review of Fluid Mechanics*, 48:219–257, 2016.
- [85] Andreas A Linninger, Cristian Tsakiris, David C Zhu, Michalis Xenos, Peter Roycewicz, Zachary Danziger, and Richard Penn. Pulsatile cerebrospinal fluid dynamics in the human brain. *IEEE Transactions on Biomedical Engineering*, 52(4):557–565, 2005.
- [86] Andreas A Linninger, Michalis Xenos, Brian Sweetman, Sukruti Ponkshe, Xiaodong Guo, and Richard Penn. A mathematical model of blood, cerebrospinal fluid and brain dynamics. *Journal of mathematical biology*, 59(6):729–759, 2009.
- [87] Antoine Louveau, Sandro Da Mesquita, and Jonathan Kipnis. Lymphatics in neurological disorders: a neuro-lympho-vascular component of multiple sclerosis and alzheimer’s disease? *Neuron*, 91(5):957–973, 2016.
- [88] Qiaoli Ma, Benjamin V Ineichen, Michael Detmar, and Steven T Proulx. Outflow of cerebrospinal fluid is predominantly through lymphatic vessels and is reduced in aged mice. *Nature communications*, 8(1):1–13, 2017.
- [89] Andrea Malandrino and Emad Moeendarbary. Poroelasticity of living tissues. *Reference Module in Biomedical Sciences*. Elsevier, pages 1–51, 2017.
- [90] Philip Kofoed Månsson, Sofia Johansson, Morten Ziebell, and Marianne Juhler. Forty years of shunt surgery at rigshospitalet, denmark: a retrospective study comparing past and present rates and causes of revision and infection. *BMJ open*, 7(1), 2017.
- [91] Giorgio Mantovani, Marta Menegatti, Alba Scerrati, Michele Alessandro Cavallo, and Pasquale De Bonis. Controversies and misconceptions related to cerebrospinal

- fluid circulation: a review of the literature from the historical pioneers' theories to current models. *BioMed research international*, 2018, 2018.
- [92] TH Maren. Effect of varying co₂ equilibria on rates of hco₃-formation in cerebrospinal fluid. *Journal of Applied Physiology*, 47(3):471–477, 1979.
- [93] Fernanda Marques, João Carlos Sousa, Maria Alexandra Brito, Jens Pahnke, Cecilia Santos, Margarida Correia-Neves, and Joana Almeida Palha. The choroid plexus in health and in disease: dialogues into and out of the brain. *Neurobiology of disease*, 107:32–40, 2017.
- [94] Vahan Martirosian, Alex Julian, and Josh Neman. The role of the choroid plexus in the pathogenesis of multiple sclerosis. In *The Choroid Plexus and Cerebrospinal Fluid*, pages 103–127. Elsevier, 2016.
- [95] Nafiseh Masoumi, F Framanzad, Behnam Zamanian, AS Seddighi, MH Moosavi, S Najarian, and Dariush Bastani. 2d computational fluid dynamic modeling of human ventricle system based on fluid-solid interaction and pulsatile flow. *Basic and clinical neuroscience*, 4(1):64, 2013.
- [96] Mitsunori Matsumae. Regarding bering's hypothesis on choroid plexus pulsatility response. *JOURNAL OF NEUROSURGERY*, 122(2):480–481, 2015.
- [97] Mitsunori Matsumae, Osamu Sato, Akihiro Hirayama, Naokazu Hayashi, Ken Takizawa, Hideki Atsumi, and Takatoshi Sorimachi. Research into the physiology of cerebrospinal fluid reaches a new horizon: intimate exchange between cerebrospinal fluid and interstitial fluid may contribute to maintenance of homeostasis in the central nervous system. *Neurologia medico-chirurgica*, 56(7):416–441, 2016.
- [98] J Gordon McComb. Recent research into the nature of cerebrospinal fluid formation and absorption. *Journal of neurosurgery*, 59(3):369–383, 1983.
- [99] Anja Meissner. Hypertension and the brain: a risk factor for more than heart disease. *Cerebrovascular Diseases*, 42(3-4):255–262, 2016.

- [100] Andi Merxhani. An introduction to linear poroelasticity. *arXiv preprint arXiv:1607.04274*, 2016.
- [101] CC Michel and FE Curry. Microvascular permeability. *Physiological reviews*, 1999.
- [102] Thomas H Milhorat. Structure and function of the choroid plexus and other sites of cerebrospinal fluid formation. In *International review of cytology*, volume 47, pages 225–288. Elsevier, 1976.
- [103] Masakazu Miyajima and Hajime Arai. Evaluation of the production and absorption of cerebrospinal fluid. *Neurologia medico-chirurgica*, pages ra–2015, 2015.
- [104] Sara Molladavoodi, Matthew Robichaud, David Wulff, and Maud Gorbet. Corneal epithelial cells exposed to shear stress show altered cytoskeleton and migratory behaviour. *PLoS one*, 12(6):e0178981, 2017.
- [105] OA Mortensen and WE Sullivan. The cerebrospinal fluid and the cervical lymph nodes. *The Anatomical Record*, 56(4):359–363, 1933.
- [106] Tatsuya Nagashima, Norihiko Tamaki, Satoshi Matsumoto, Barry Horwitz, and Yasuyuki Seguchi. Biomechanics of hydrocephalus: a new theoretical model. *Neurosurgery*, 21(6):898–904, 1987.
- [107] Deborah J Nelson and Ernest M Wright. The distribution, activity, and function of the cilia in the frog brain. *The Journal of physiology*, 243(1):63, 1974.
- [108] Jordan N Norwood, Qingguang Zhang, David Card, Amanda Craine, Timothy M Ryan, and Patrick J Drew. Anatomical basis and physiological role of cerebrospinal fluid transport through the murine cribriform plate. *eLife*, 8:e44278, 2019.
- [109] Emilie W Olstad, Christa Ringers, Jan N Hansen, Adinda Wens, Cecilia Brandt, Dagmar Wachten, Emre Yaksi, and Nathalie Jurisch-Yaksi. Ciliary beating compartmentalizes cerebrospinal fluid flow in the brain and regulates ventricular development. *Current Biology*, 29(2):229–241, 2019.

- [110] Darko Orešković and Marijan Klarica. The formation of cerebrospinal fluid: nearly a hundred years of interpretations and misinterpretations. *Brain research reviews*, 64(2):241–262, 2010.
- [111] Darko Orešković and Marijan Klarica. Measurement of cerebrospinal fluid formation and absorption by ventriculo-cisternal perfusion: what is really measured? *Croatian Medical Journal*, 55(4):317–327, 2014.
- [112] World Health Organization. Ageing and health. world health organization, 2018.
- [113] World Health Organization et al. Neurological disorders affect millions of people worldwide, new who report shows. 2007.
- [114] George D Pappas and Virginia M Tennyson. An electron microscopic study of the passage of colloidal particles from the blood vessels of the ciliary processes and choroid plexus of the rabbit. *The Journal of cell biology*, 15(2):227–239, 1962.
- [115] William M Pardridge. Drug and gene delivery to the brain: the vascular route. *Neuron*, 36(4):555–558, 2002.
- [116] Constantine Pozrikidis. *Computational hydrodynamics of capsules and biological cells*. CRC press, 2010.
- [117] Jeppe Praetorius. Water and solute secretion by the choroid plexus. *Pflügers Archiv-European Journal of Physiology*, 454(1):1–18, 2007.
- [118] Martin Prince, Martin Knapp, Maelenn Guerchet, Paul McCrone, Matthew Prina, A Comas-Herrera, Raphael Wittenberg, Bayo Adelaja, Bo Hu, Derek King, et al. Dementia uk: -overview. 2014.
- [119] Stanley I Rapoport and Karen D Pettigrew. A heterogenous, pore-vesicle membrane model for protein transfer from blood to cerebrospinal fluid at the choroid plexus. *Microvascular Research*, 18(1):105–119, 1979.
- [120] EM Renkin. Multiple pathways of capillary permeability. *Circulation research*, 41(6):735–743, 1977.

- [121] Johannes AG Rhodin. The diaphragm of capillary endothelial fenestrations. *Journal of ultrastructure research*, 6(2):171–185, 1962.
- [122] Laurent Sakka, Guillaume Coll, and Jean Chazal. Anatomy and physiology of cerebrospinal fluid. *European annals of otorhinolaryngology, head and neck diseases*, 128(6):309–316, 2011.
- [123] Hemant Sarin. Physiologic upper limits of pore size of different blood capillary types and another perspective on the dual pore theory of microvascular permeability. *Journal of angiogenesis research*, 2(1):14, 2010.
- [124] Kazunobu Sawamoto, Hynek Wichterle, Oscar Gonzalez-Perez, Jeremy A Cholfin, Masayuki Yamada, Nathalie Spassky, Noel S Murcia, Jose Manuel Garcia-Verdugo, Oscar Marin, John LR Rubenstein, et al. New neurons follow the flow of cerebrospinal fluid in the adult brain. *Science*, 311(5761):629–632, 2006.
- [125] Gaetano Scala, Marco Corona, Luigi michele Pavone, Alessandra Pelagalli, Paolo De Girolamo, and Norma Staiano. Structural and functional features of choroid epithelium from buffalo brain. *The Anatomical Record: Advances in Integrative Anatomy and Evolutionary Biology: Advances in Integrative Anatomy and Evolutionary Biology*, 290(11):1399–1412, 2007.
- [126] Jean-Marie Serot, Marie-Christine Béné, and Gilbert C Faure. Choroid plexus, aging of the brain, and alzheimer’s disease. *Frontiers in Bioscience-Landmark*, 8(6):515–521, 2003.
- [127] Tarek Shalaby, Federica Achini, and Michael A Grotzer. Targeting cerebrospinal fluid for discovery of brain cancer biomarkers. *Journal of cancer metastasis and treatment*, 2016(2):176–187, 2016.
- [128] Maya Simionescu and Nicolae Simionescu. *Endothelial cell biology in health and disease*. Springer Science & Business Media, 2013.
- [129] Matthew J Simon and Jeffrey J Iliff. Regulation of cerebrospinal fluid (csf) flow in neurodegenerative, neurovascular and neuroinflammatory disease. *Biochimica et Biophysica Acta (BBA)-Molecular Basis of Disease*, 1862(3):442–451, 2016.

- [130] Amar B Singh, Ashok Sharma, and Punita Dhawan. Claudin family of proteins and cancer: an overview. *Journal of oncology*, 2010, 2010.
- [131] Bercan Siyahhan, Verena Knobloch, Diane de Zélicourt, Mahdi Asgari, Marianne Schmid Daners, Dimos Poulidakos, and Vartan Kurtcuoglu. Flow induced by ependymal cilia dominates near-wall cerebrospinal fluid dynamics in the lateral ventricles. *Journal of the Royal Society Interface*, 11(94):20131189, 2014.
- [132] Y Sohma, MA Gray, Y Imai, and BE Argent. A mathematical model of the pancreatic ductal epithelium. *The Journal of membrane biology*, 154(1):53–67, 1996.
- [133] Yoshiro Sohma, MA Gray, Y Imai, and BE Argent. Hco 3- transport in a mathematical model of the pancreatic ductal epithelium. *The Journal of membrane biology*, 176(1):77–100, 2000.
- [134] Yoshiro Sohma, MA Gray, Y Imai, and BE Argent. Hco3- transport in a mathematical model of the pancreatic ductal epithelium. *The Journal of membrane biology*, 176(1):77–100, 2000.
- [135] Peter Solár, Alemeh Zamani, Lucie Kubíčková, Petr Dubový, and Marek Joukal. Choroid plexus and the blood–cerebrospinal fluid barrier in disease. *Fluids and Barriers of the CNS*, 17(1):1–29, 2020.
- [136] Reynold Spector and Conrad E Johanson. The mammalian choroid plexus. *Scientific American*, 261(5):68–75, 1989.
- [137] Reynold Spector, Richard F Keep, S Robert Snodgrass, Quentin R Smith, and Conrad E Johanson. A balanced view of choroid plexus structure and function: focus on adult humans. *Experimental neurology*, 267:78–86, 2015.
- [138] Jolanda M Spijkerman, Lennart J Geurts, Jeroen CW Siero, Jeroen Hendrikse, Peter R Luijten, and Jaco JM Zwanenburg. Phase contrast mri measurements of net cerebrospinal fluid flow through the cerebral aqueduct are confounded by respiration. *Journal of Magnetic Resonance Imaging*, 49(2):433–444, 2019.

- [139] Nathalie Strazielle, Rita Creidy, Christophe Malcus, José Boucraut, and Jean-François Gherzi-Egea. T-lymphocytes traffic into the brain across the blood-csf barrier: evidence using a reconstituted choroid plexus epithelium. *PLoS One*, 11(3):e0150945, 2016.
- [140] Nathalie Strazielle and Jean-Francois Gherzi-Egea. Choroid plexus in the central nervous system: biology and physiopathology. *Journal of neuropathology & experimental neurology*, 59(7):561–574, 2000.
- [141] Nathalie Strazielle and Jean-François Gherzi-Egea. Potential pathways for cns drug delivery across the blood-cerebrospinal fluid barrier. *Current pharmaceutical design*, 22(35):5463–5476, 2016.
- [142] Bao-Liang Sun, Li-hua Wang, Tuo Yang, Jing-yi Sun, Lei-lei Mao, Ming-feng Yang, Hui Yuan, Robert A Colvin, and Xiao-yi Yang. Lymphatic drainage system of the brain: A novel target for intervention of neurological diseases. *Progress in neurobiology*, 163:118–143, 2018.
- [143] Brian Sweetman, Michalis Xenos, Laura Zitella, and Andreas A Linninger. Three-dimensional computational prediction of cerebrospinal fluid flow in the human brain. *Computers in biology and medicine*, 41(2):67–75, 2011.
- [144] Ehsan Tadayon, Alvaro Pascual-Leone, Daniel Press, Emiliano Santarnecchi, Alzheimer’s Disease Neuroimaging Initiative, et al. Choroid plexus volume is associated with levels of csf proteins: relevance for alzheimer’s and parkinson’s disease. *Neurobiology of aging*, 89:108–117, 2020.
- [145] Ken Takizawa, Mitsunori Matsumae, Naokazu Hayashi, Akihiro Hirayama, Fumiya Sano, Satoshi Yatsushiro, and Kagayaki Kuroda. The choroid plexus of the lateral ventricle as the origin of csf pulsation is questionable. *Neurologia medico-chirurgica*, pages oa–2017, 2017.
- [146] Oisenyl José Tamega, Luís Fernando Tirapelli, and Sidnei Petroni. Scanning electron microscopy study of the choroid plexus in the monkey (*cebus apella apella*). *Arquivos de Neuro-Psiquiatria*, 58(3B):820–825, 2000.

- [147] Lauren N Telano and Stephen Baker. Physiology, cerebral spinal fluid (csf). In *StatPearls [Internet]*. StatPearls Publishing, 2018.
- [148] S Randall Thomas and George Dagher. A kinetic model of rat proximal tubule transport—load-dependent bicarbonate reabsorption along the tubule. *Bulletin of mathematical biology*, 56(3):431–458, 1994.
- [149] Eleuterio Francisco Toro, Morena Celant, Qinghui Zhang, Christian Contarino, Nivedita Agarwal, Andreas Linninger, and Lucas Omar Müller. Cerebrospinal fluid dynamics coupled to the global circulation in holistic setting: mathematical models, numerical methods and applications. *International Journal for Numerical Methods in Biomedical Engineering*, 38(1):e3532, 2022.
- [150] Christopher R Trimble, HR Harnsberger, M Castillo, M Brant-Zawadzki, and AG Osborn. “giant” arachnoid granulations just like csf?: Not!! *American journal of neuroradiology*, 31(9):1724–1728, 2010.
- [151] B Tserennadmid, B Odmaa, A Avirmed, and D Amgalanbaatar. The study of macro and micro structure of choroid plexus of adult brain ventricles. *Mongolian Medical Science Journal*, 168(2):9–11, 2014.
- [152] Miriam E Van Strien, Simone A Van Den Berge, and Elly M Hol. Migrating neuroblasts in the adult human brain: a stream reduced to a trickle. *Cell research*, 21(11):1523–1525, 2011.
- [153] Jenny Venton. *A Poroelastic Model of Spinal Cord Cavities*. PhD thesis, University of Brighton, 2018.
- [154] Valery L Visser, Henry Rusinek, and Johannes Weickenmeier. Peak ependymal cell stretch overlaps with the onset locations of periventricular white matter lesions. *Scientific Reports*, 11(1):1–12, 2021.
- [155] Marion L Walker. Cerebrospinal fluid physiology: Problems and possibilities. *Neurosurgery*, 58(CN_suppl_1):65–71, 2011.

- [156] Abdul Majid Wani, Najah R Zayyani, Wail Al Miamini, Amer M Khoujah, Zeyad Alharbi, and Mohd S Diari. Arnold–chiari malformation type 1 complicated by sudden onset anterior spinal artery thrombosis, tetraparesis and respiratory arrest. *Case Reports*, 2011:bcr0720103170, 2011.
- [157] ALAN M Weinstein. Chloride transport in a mathematical model of the rat proximal tubule. *American Journal of Physiology-Renal Physiology*, 263(5):F784–F798, 1992.
- [158] Alan M Weinstein and Thomas A Krahn. A mathematical model of rat ascending henle limb. ii. epithelial function. *American Journal of Physiology-Renal Physiology*, 298(3):F525–F542, 2010.
- [159] Peter Wostyn, Debby Van Dam, Kurt Audenaert, and Peter Paul De Deyn. Increased cerebrospinal fluid production as a possible mechanism underlying caffeine’s protective effect against alzheimer’s disease. *International Journal of Alzheimer’s Disease*, 2011, 2011.
- [160] Huixin Xu, Ryann M Fame, Cameron Sadegh, Jason Sutin, Christopher Naranjo, Della Syau, Jin Cui, Frederick B Shipley, Amanda Vernon, Fan Gao, et al. Choroid plexus nkcc1 mediates cerebrospinal fluid clearance during mouse early postnatal development. *Nature communications*, 12(1):447, 2021.
- [161] Shigeki Yamada, Masatsune Ishikawa, and Kazuhiko Nozaki. Exploring mechanisms of ventricular enlargement in idiopathic normal pressure hydrocephalus: a role of cerebrospinal fluid dynamics and motile cilia. *Fluids and Barriers of the CNS*, 18(1):1–11, 2021.
- [162] Makoto Yamaguchi, Martin C Steward, Kieran Smallbone, Yoshiro Sohma, Akiko Yamamoto, Shigeru BH Ko, Takaharu Kondo, and Hiroshi Ishiguro. Bicarbonate-rich fluid secretion predicted by a computational model of guinea-pig pancreatic duct epithelium. *The Journal of Physiology*, 595(6):1947–1972, 2017.
- [163] Mokhtar Zagzoule and Jean-Pierre Marc-Vergnes. A global mathematical model of the cerebral circulation in man. *Journal of biomechanics*, 19(12):1015–1022, 1986.

- [164] Shadi Zaheri and Fatemeh Hassanipour. A comprehensive approach to the mathematical modeling of mass transport in biological systems: Fundamental concepts and models. *International Journal of Heat and Mass Transfer*, 158:119777, 2020.
- [165] Dehong Zeng, Taras Juzkiw, A Thomas Read, Darren W-H Chan, Matthew R Glucksberg, C Ross Ethier, and Mark Johnson. Young's modulus of elasticity of schlemm's canal endothelial cells. *Biomechanics and modeling in mechanobiology*, 9(1):19–33, 2010.